

---

---

# Guided Projectile

- P5 -

---



Project Report  
Group 515

Aalborg University  
Department of Electronic Systems  
Fredrik Bajers Vej 7B  
DK-9220 Aalborg

Copyright © Aalborg University 2018

This report was written in LaTeX and has been shared online in-between the group members using ShareLatex licensed to all students at Aalborg University.



**Department of Electronic Systems**

Fredrik Bajers Vej 7

DK-9220 Aalborg Ø

<http://es.aau.dk>

## AALBORG UNIVERSITY

### STUDENT REPORT

**Title:**

Guided Projectile

**Theme:**

Digital and analog systems interacting with the surroundings

**Project Period:**

Fall Semester 2018

**Project Group:**

Group 515

**Participants:**

Frederik Skyt Dæncker Rasmussen  
Magnus Bøgh Borregaard Christensen  
Max Væhrens  
Claus Lolholm Nielsen  
Jakob Krarup Thomsen  
Peter Kjær Fisker

**Supervisor:**

Jan H. Mikkelsen

**Report Page Numbers:** 80

**Appendix Page Numbers:** 38

**Date of Completion:**

December 19, 2018

**Abstract:**

The purpose of this report is to document the design and implementation of a guidance system in a projectile, with the intention of reducing its circular error probable. A modular projectile platform is designed based on basic aerodynamic considerations and constructed in ABS plastic using a 3D-printer. The projectile is equipped with circuits using a quad photodiode combined with high gain stages and narrow band filtering for the purpose of detecting the relative direction of a target that emits pulse modulated IR light. When the projectile is directed straight at the target, the target can successfully be detected at a range of 45 meters. A general mathematical model of the projectile is created based on a second-order Nomoto model, on the assumption that the dynamics of the wings on the projectile is similar to those of the rudder on a boat. However, due to the designed projectile only obtaining marginal open loop stability it was not possible to determine values for the coefficients of the model. Because of this it was not possible to design and implement a controller in the system, although some thoughts and considerations about the design and performance specifications of the control system is presented.

# Contents

<b>I Project Scope</b>	<b>1</b>
<b>1 Introduction</b>	<b>2</b>
1.1 Examples of Guided Projectiles . . . . .	3
1.2 Introduction to the System to be Replicated . . . . .	4
1.3 Problem Statement . . . . .	5
<b>2 Product Specifications</b>	<b>6</b>
2.1 Functional Requirements . . . . .	6
2.2 Limitations . . . . .	6
2.3 Design Choices . . . . .	7
<b>3 System Design Overview</b>	<b>8</b>
3.1 Projectile . . . . .	9
3.2 Launcher and Target . . . . .	10
3.3 Hardware Choices . . . . .	10
3.4 Conclusion of Part One . . . . .	13
<b>II System Design</b>	<b>14</b>
<b>4 Design of Ground Systems</b>	<b>15</b>
4.1 Target . . . . .	16
4.2 Projectile Launcher . . . . .	17
4.3 Gravity Assisted Launch System . . . . .	18
4.4 Base Station . . . . .	19

## Contents

<b>5 Projectile Design</b>	<b>22</b>
5.1 Design Requirements . . . . .	23
5.2 Tools for Model Design . . . . .	23
5.3 Design Methodology . . . . .	24
5.4 Design Overview . . . . .	26
5.5 Assembly Interface . . . . .	27
5.6 Nose Design . . . . .	27
5.7 Body Design . . . . .	29
5.8 Room Separator Design . . . . .	29
5.9 Tail Design . . . . .	30
5.10 Fin Design . . . . .	33
<b>6 Design of Direction Detection System</b>	<b>35</b>
6.1 Direction Detection Theory . . . . .	36
6.2 Design of Pinhole . . . . .	37
6.3 IR Pulse Modulation . . . . .	37
6.4 Circuit Requirements . . . . .	38
6.5 Photodiode and Transimpedance Amplifier . . . . .	43
6.6 Design of Analog Filters . . . . .	46
6.7 RMS-to-DC conversion . . . . .	53
6.8 Analog to Digital Conversion of Photodiode Signal . . . . .	53
<b>7 Auxiliary Circuits</b>	<b>55</b>
7.1 Power Supplies and Voltage Regulators . . . . .	55
7.2 LED's on the Projectile . . . . .	55
7.3 Optocoupler . . . . .	55
<b>8 Embedded Design</b>	<b>57</b>
8.1 Choice of Programming Paradigm . . . . .	58
8.2 Peripheral Communication . . . . .	58

## Contents

8.3 Tasks and Interrupt Service Routines . . . . .	60
8.4 PWM Motor Control . . . . .	62
8.5 Post Processing . . . . .	62
<b>9 Design of Controller</b>	<b>64</b>
9.1 Introduction . . . . .	64
9.2 The Projectile . . . . .	65
9.3 The Disturbances . . . . .	66
9.4 Thoughts About Controller Design . . . . .	67
<b>10 Implementation</b>	<b>70</b>
10.1 Implementation of Analog Circuits . . . . .	70
10.2 Implementation of Digital Systems . . . . .	71
10.3 Implementation of Projectile . . . . .	72
10.4 Implementations of Pinhole . . . . .	73
<b>III Discussion and Conclusion</b>	<b>75</b>
<b>11 Discussion</b>	<b>76</b>
<b>12 Conclusion</b>	<b>77</b>
<b>Bibliography</b>	<b>78</b>
<b>Appendix:</b>	<b>81</b>
<b>A Determining the Size of the Pinhole</b>	<b>81</b>
A.1 Relationship between area and angle of incidence. . . . .	84
<b>B Photodiode Amplifier Bandwidth, Stability and Noise Analysis</b>	<b>89</b>
B.1 Bandwidth of the TIA . . . . .	89
B.2 Stability of the TIA . . . . .	90
B.3 RMS Noise Analysis of the TIA . . . . .	92

## Contents

<b>C Input Impedance of MFB Bandpass Filter</b>	<b>97</b>
C.1 Defining Input Impedance . . . . .	97
C.2 Circuit Analysis of MFB filter . . . . .	98
<b>D Test journal: Trans-Impedance Amplifier</b>	<b>100</b>
D.1 Test purpose . . . . .	100
D.2 Test frame . . . . .	100
D.3 Test results and data processing . . . . .	102
<b>E Test journal: High Pass Filter</b>	<b>103</b>
E.1 Test purpose . . . . .	103
E.2 Test frame . . . . .	103
E.3 Test results and data processing . . . . .	105
<b>F Test journal: Band Pass Filter</b>	<b>106</b>
F.1 Test purpose . . . . .	106
F.2 Test frame . . . . .	106
F.3 Test results and data processing . . . . .	108
<b>G Test journal: Photodiode Circuit</b>	<b>110</b>
G.1 Test purpose . . . . .	110
G.2 Test frame . . . . .	110
G.3 Test results and data processing . . . . .	112
G.4 Sources of error and other uncertainties . . . . .	112
G.5 Test purpose . . . . .	113
G.6 Test frame . . . . .	113
G.7 Test results and data processing . . . . .	115
G.8 Sources of error and other uncertainties . . . . .	118

# Part I

# Project Scope

# Chapter 1

## Introduction

In modern warfare it is desirable to avoid civilian casualties. However, due to the nature of war, accidents occur on a regular basis. Taking a look at the ongoing war in Afghanistan during the period from 2001 to mid 2016, it is estimated that about 31,000 civilians were killed and 41,000 were injured[1].

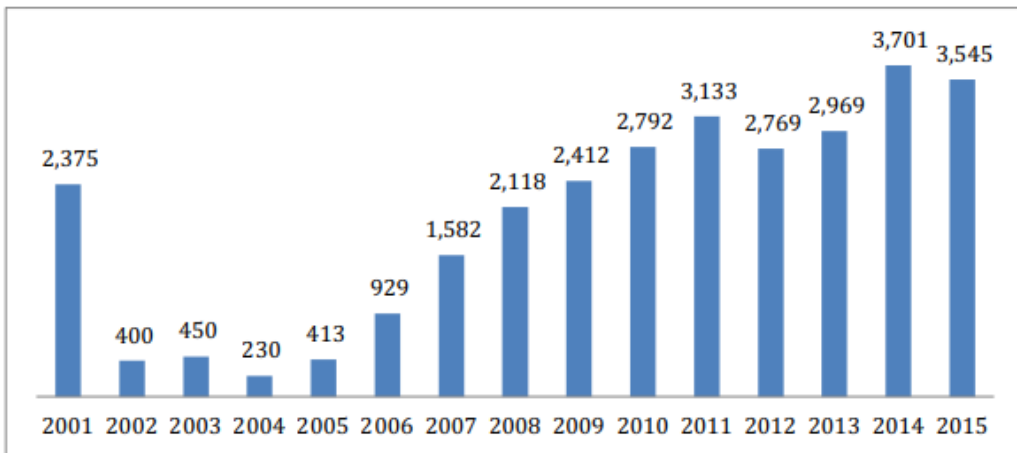


**Figure 1.1:** Number of Civilians Killed in Afghanistan from 2001 to 2015 [1].

In Afghanistan, explosives are often used to neutralise a threat, but these explosives cause a lot of collateral damage following their impact. Additionally, as the range of projectiles and bombs increases, their accuracy tends to decrease, which further increases the risk of collateral damage or friendly fire. It is estimated, that the count of Afghan civilian casualties from air strikes has risen more than 50 percent in the year 2017, than 2016[2].

A way to reduce the casualty count, could be to use a method which guides the projectile to produce a more precise hit. By guiding and achieving a precise shot, it is possible to reduce the explosive material to a minimum. As the amount of explosive material is reduced, the blast radius is reduced and in turn the area of impact is curbed, lowering the risk of casualties.

## 1.1 Examples of Guided Projectiles

In this section some examples of already crafted guided projectiles are presented. These examples are based on the arsenal of the United States. These examples are only projectiles used to hit ground targets. In the list of active missiles in the United states, there are two subcategories which are used for surface targets. Air-to-surface, which uses aircraft to fire their missiles to targets on the surface, and surface-to-surface, which uses missiles launched from the ground or ocean, to a target on the surface. Since some of the missiles presented use the same form of guidance, only one missile per guidance type will be used as an example.

In the air-to-surface missile "AGM-114 Hellfire", the used form of guidance technology is called Semi-active laser homing (SALH)[3]. The SALH guidance technique employs a laser, which is kept pointing at a target. The radiation from the laser bounces off the target and is scattered around in all directions. The missile is launched in the area near the target, and once the missile is in close enough proximity of the radiation a laser seeker placed on the missile, detects which direction the energy is coming from, and adjusts the trajectory of the missile towards it[4]. The SALH guiding technique is illustrated on figure 1.2.

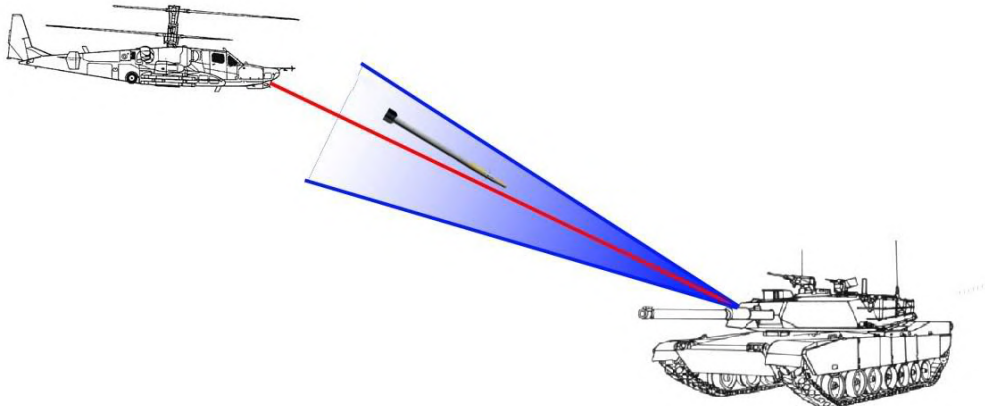


**Figure 1.2:** Example of a SALH guided missile, shot from an aircraft towards a ground target [5].

Another example of a guided air-to-surface missile is the "AGM-65 Maverick D/F/G" for its guidance system, it uses infrared homing[6]. Infrared homing, also known as heatseeking, is a passive guidance system, which tracks the infrared light emitted from a target. The infrared light comes as a result of heat radiation, hence the name heatseeking. Infrared homing is a passive guidance type, in the sense that no targeting laser is used to track the target. This results in a harder to detect missile, due to a lack of active targeting. The actual guidance of the missile itself is of course still active. The AGM-65D uses infrared imaging, where the IR sensor is a focal plane array, which produces an image in infrared. By using this technique, the missile is harder to trick with decoys, and doesn't target the sun[7].

In addition to self-propelled missiles, another class exists called guided artillery shells. Here, a guiding system is implemented in artillery shells, which are not self-propelled. This results in different methods being used to control the flight path from the launcher to the target. An example of a guided artillery shell is the M982 Excalibur. The Excalibur uses GPS and an Inertial Measurement Unit to hit their targets. This results in impressive accuracies, the Excalibur for example, having a Circular Error

## 1.2. Introduction to the System to be Replicated

Probable (CEP) of 4 meters[8]. CEP is a method to measure the precision of a weapon system. It is a circle centered on the mean, which means 50% of the hits is in this circle.[9] New iterations of the Excalibur aims to implement laser guidance as well, for the use of naval vessels.



**Figure 1.3:** Illustration of an Excalibur guided artillery shell [10].

As seen on figure 1.3, the Excalibur is equipped with canards in the front, which are used to manoeuvre towards the target[8].

As a final example, there also exists small-calibre guided projectiles the size of regular sniper rounds. In 2015, a United States agency called DARPA published a video of a new type of guided .50 calibre bullet, that they had developed. This bullet, called EXACTO, showed capable of both correcting for errors in aim and following a moving target [11].

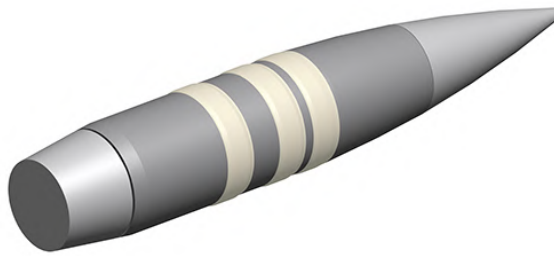


**Figure 1.4:** Rendered photo of the EXACTO bullet [12].

On figure 1.4 DARPA's rendering of the projectile can be seen, which shows no outer control surfaces. In fact, the exact method of how the projectile manoeuvres is still classified.

As these examples show, it is evident that guided projectiles indeed can help reduce problems with collateral damage and civilian casualties. Thus, this report aims to document the process of replicating a guided projectile in a smaller scale, to determine some of the problems and challenges associated with such development and how to solve them if possible.

## 1.2 Introduction to the System to be Replicated

As described earlier, in order to make it easier to investigate how to develop a guidance system it is necessary to lessen the scale from full scale missiles to something smaller.

### 1.3. Problem Statement

The proposed system is close to the Excalibur guided artillery shell, using laser guidance together with GPS and an inertial measurement unit (IMU), but the projectile itself is closer to a mortar rather than an artillery shell. The main difference here between a mortar shell and an artillery shell is the trajectory, and thus the range, of the projectile. Normally the trajectory of an artillery shell is more flat, compared to a mortar, as shown in figure 1.5.

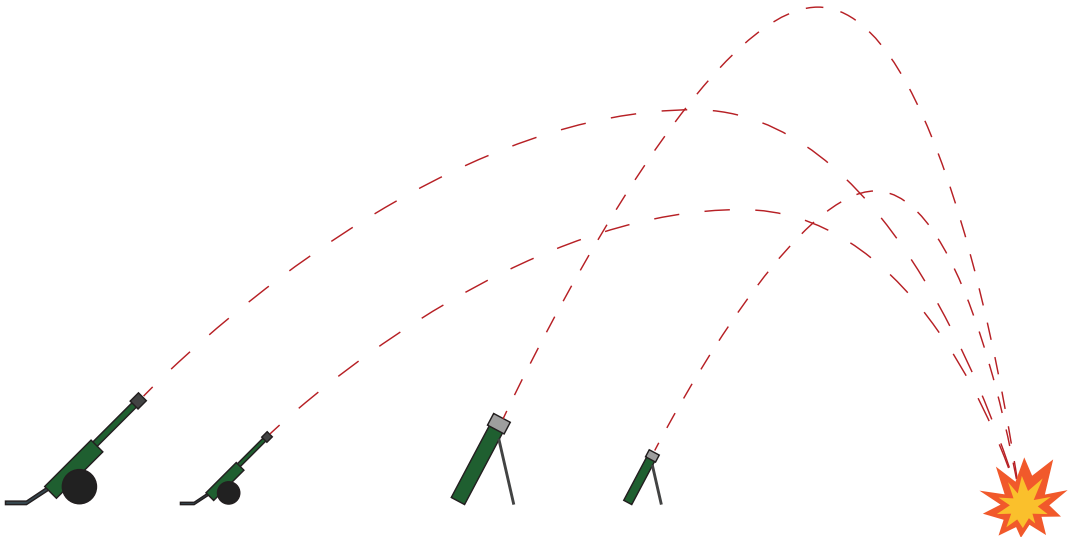


**Figure 1.5:** Illustration showing the trajectories of artillery (left) and mortars (right) [13].

In addition to this, mortars are much smaller and light weight compared to artillery shells, enabling them to be positioned by hand. These characteristics most likely makes some of the physical design challenges easier to overcome. However, the guidance principles used are assumed to differ only marginally between artillery shells and mortar shells.

The system to be replicated can be divided into four main parts; physical design of projectile, communication between projectile and launcher, feedback control to manoeuvre the projectile and processing of sampled signals from sensors in the projectile.

## 1.3 Problem Statement

From the analysis it can be concluded that guided projectiles are increasingly used in the military to enhance accuracy. Whether to compensate for weather, wind, target movement and other factors or to reduce the amount of explosives carried, the goal remains the same. Thus, it is decided to design a small scale guided projectile. To obtain insight into how a guidance system works and what challenges that are associated with the development of such a system, this report attempts to answer the following questions:

- How is a guidance system designed using optics and an IMU?
- Will the designed guidance system reduce the CEP of a projectile?

## Chapter 2

# Product Specifications

In this chapter, the different specifications of the projectile will be established. These specifications are established based on the problem statement. The different specifications for the product will be divided into three groups: Functional requirements, Design choices, and Hardware choices.

### 2.1 Functional Requirements

As the focus of the project is to design and develop a guided projectile with the intention of reducing its CEP, the only functional requirement is that the CEP must be reduced when the guidance system is used compared to when it is not.

However, in addition to this requirement, some constraints arise as a result of an air cannon provided by the university, to be used as a launcher. To use this, the projectile has some size constraints that must be met.

### 2.2 Limitations

In order to justify some of the decisions made during the project it is important to understand the limitations of the project. The primary limitations of the project are as follows:

- Time.
- Budget.
- Size requirements.

The project runs over an approximately four-month long period, where the first half is shared with coursework. As such, it is important to take this into consideration when choosing design methods, among other things. This is especially true when dealing with out of area of expertise subjects, such as aerodynamic design.

When deciding on which hardware to use, budget must be kept in mind. The budget is not set in stone but is usually in the range of 2000 to 5000 DKK. As such, components should be compared both

### 2.3. Design Choices

in quality and price, within reason of course. It should however be noted that if a component can be reused, like for instance a microcontroller, the budget can be negotiated.

Finally, due to using a pre-built launcher, there are some limitations on the size of the projectile and its electronics.

## 2.3 Design Choices

The design choices and a short explanation on why the choices are made can be found in table 2.1.

**Table 2.1:** Design choices

Nr.	The design choice	The justification
1.	Wings used to manoeuvre the projectile.	Wings are chosen over other options due to their simplicity compared to other solutions such as reactions wheels.
2.	Digital controller instead of an analog controller.	A digital controller is chosen because it is easier to design and make small changes compared to an analogue controller. A digital controller is slower than an analog controller, but the speed of the digital controller is deemed sufficient for the application.
3.	Use of sensors to measure in-flight dynamics.	During flight, the controller is going to use measurements of variables such as speed and attitude to guide the projectile.
4.	Logging of measured in-flight dynamics.	To be able to analyse the in-flight dynamics after the projectile has landed, and not only in real-time during flight.
5.	Targeting with photodiodes.	Using photodiodes gives higher accuracy and sampling speed than e.g. GPS. Additionally, it is electrically simpler to implement than for example infrared imaging.
6.	Flight time of at least 8 seconds.	For the controller to have time to react and guide the projectile, it is necessary that the projectile has enough flight time. With the air cannon provided, a flight time of at least 8 seconds should be possible.
7.	Wireless setup of the projectile.	In order to make small changes to the programming in the projectile before launch, without the need to disassemble it.
8.	Open-loop stability of the projectile.	To make modelling of the projectile and design of the controller significantly simpler, it is chosen that the projectile must have stable flight characteristics without the implementation of guidance systems.

# Chapter 3

## System Design Overview

This chapter covers the overall design of the system as well as the individual parts and their purposes. First an overview diagram of the system is presented. Followed by a description of purpose and functionality of the various parts are individually addressed.

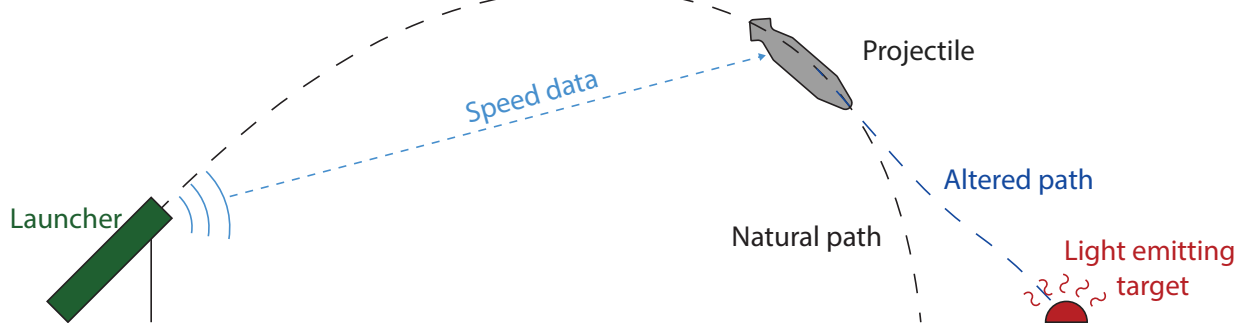


**Figure 3.1:** Illustration of the purpose of the system.

Figure 3.1 shows the general idea behind the system. In order to achieve the objective, a projectile is to be constructed, modelled and controlled using a control system. For the control system to work, the projectile is fitted with sensors, allowing it to determine its current location, deviation from the desired path, among other things. The most important of the sensors is a quad photodiode, which will allow for detecting the target. The reason for a quad photodiode is to support the measurement of error signals in two directions. The target is a battery-powered LED since it is much more powerful than a laser, thus being much easier to detect. This is done to limit the scope of the project to fit within the time and budget constraints.

In addition to this, the projectile is also fitted with a Bluetooth module. This allows for wirelessly changing parameters of control loops, motor offsets etc. It also allows the launcher to wirelessly transmit the muzzle velocity of the projectile, since the on-board accelerometer might not be able to

### 3.1. Projectile

handle the high g's of a launch. All subsystems will be explained further in sections 3.1 to 3.2.

With the purpose and how to achieve it laid out, a block diagram of the different subsystems can be made. The block diagram can be seen in figure 3.2 and will be referenced to in the design chapters of the report. This is done to give an overview over which parts of the full system is currently being designed.

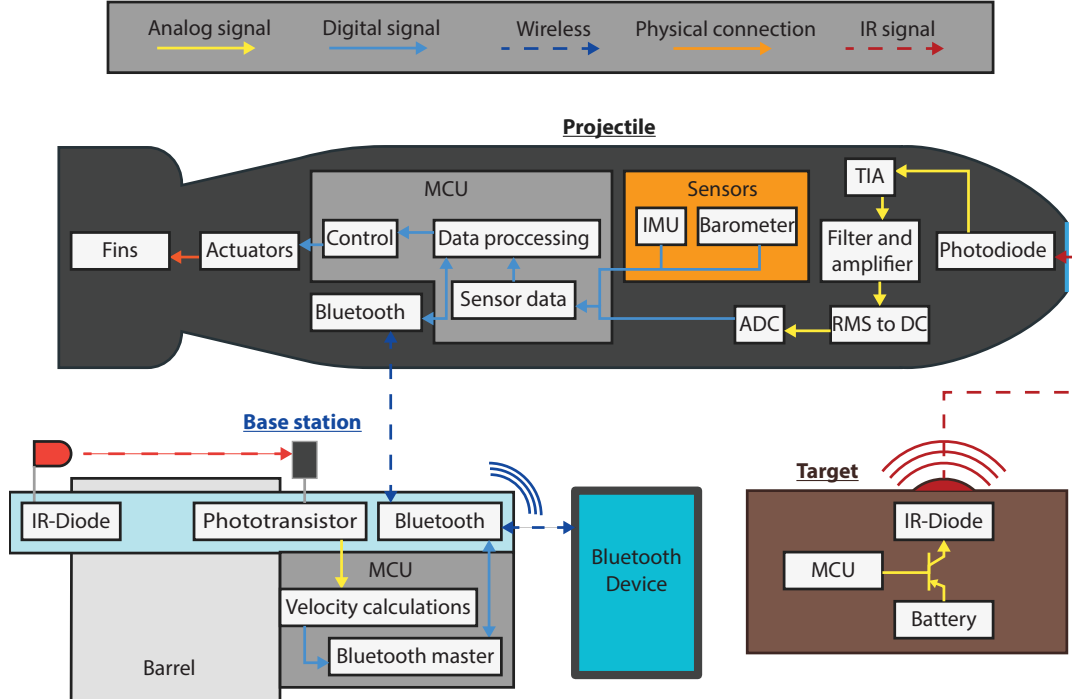


**Figure 3.2:** Block diagram of the systems in the project.

## 3.1 Projectile

The projectile is the main focus of the project, and it uses actuators to steer towards the target, based on input determined by an onboard controller. The different components in the projectile are shown in figure 3.2.

The physical body of the projectile is very important as it heavily influences the projectile's flight characteristics. If the body is not designed correctly, it becomes harder to manoeuvre the projectile and obtain stable flight. Thus, it is desired to have a projectile that is open loop stable, meaning that it is stable even without a controller to steer it towards its target. In order to design the projectile body properly, the aerodynamics of mortar shells and similar projectiles are examined. However, as aerodynamics are a very complex field of study, some simplifications and assumptions have to be made when designing the projectile. In order for the projectile to be able to manoeuvre during flight, it has to have some actuators to interact with its surroundings.

In order to hit a target, it is necessary for the projectile to be able to sense its surroundings, especially the target itself. As the target is emitting IR-light, an array of IR photodiodes is used to find in which direction the target is located. To accurately measure the output signals from the photodiodes, the signals needs to be heavily amplified and filtered for any out-of-band noise. In addition to the photodiodes, the projectile is equipped with an IMU and a barometer. The barometer measures the

### 3.2 Launcher and Target

projectile's altitude while the IMU, consisting of an accelerometer, a gyroscope and a magnetometer, is used to determine the speed and orientation of the projectile.

Most critical to the system is the control system, which is responsible for keeping the projectile on course. It is this which enables the projectile to manoeuvre during flight and doing so in a stable manner.

The sensors and motors are all connected to a central MCU. The MCU runs the control loop calculations, as well as reading data from the sensors and controlling the motors that control the wings. The MCU is also used to log all sensor data for post flight analysis. Finally, it also handles communication between the base station and the projectile.

## 3.2 Launcher and Target

To shoot the projectile a launcher is required. The launcher must fire to projectile far and high enough to result in at least 8 seconds of flight time. It is required to at least give the projectile enough airtime to be able to detect the target diode and correct the trajectory.

The target will be a diode placed at the desired location for impact. This will allow the control system in the projectile to use this as a heading for the desired trajectory and correct its current trajectory accordingly.

In addition to the launcher and target, a base station is also to be designed. This base station will allow for muzzle velocity measurements, as well as communication with the projectile.

## 3.3 Hardware Choices

To implement the system according to the requirements, a hardware platform will have to be decided upon. There are many viable options and not one right choice. These choices are based on the requirements, what was available and on what would provide the best development experience.

### 3.3.1 Microcontroller

To interpret sensor input and control the projectile in flight, a micro-controller-unit (MCU) is required. For this purpose, a programmable system on chip (PSOC) 5LP featuring an ARM Cortex-M3 was chosen. For easing the implementation, a CY8CKIT-059 development board was chosen as the design platform of choice. The PSOC 5LP was primarily chosen due to its abundance of on-board customisable analog and digital peripherals. These include elements such as operational amplifiers, ADC's, DAC's, various hardware communication protocols, a small amount of programmable logic devices (programmed with Verilog), and a DMA controller. Additionally, the authors have previous experience designing for the PSOC, which decreased development time. One caveat of the chosen MCU is its lack of a dedicated floating-point unit, meaning that all floating point logic will have to be emulated, resulting in a performance degradation. While all calculations are performed using floating point, these only need to be performed a few hundred times per second, which the ARM Cortex-M3 easily handles.

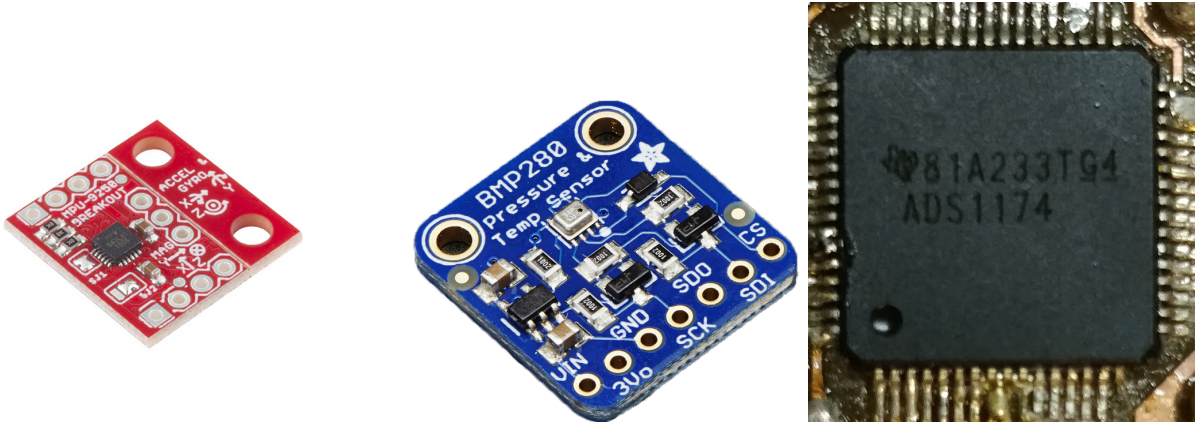
### 3.3. Hardware Choices



**Figure 3.3:** CY8CKIT-059 Development Board [14].

#### 3.3.2 Sensors, Logging, Communication, and Actuators

To monitor the projectile's flight dynamics, both with and without a control system, it is of interest to measure the projectile's instantaneous orientation in space. For this purpose, an MPU9250 Intertial Measurement Unit (IMU) with an accelerometer, magnetometer, and gyroscope will be used. Additionally, a BMP280 barometer will be used to measure the projectile's altitude. The conversion of the analog signals from the quad photodiodes to a digital signal an ADS1174 quad ADC is chosen. The IMU, barometer, and ADC were all chosen partially due to their ability to communicate using SPI, as only having to develop sensor firmware for a single communication protocol would limit the complexity of the code.



(a) MPU9250 breakout board from Sparkfun [15]

(b) BMP280 breakout board from Adafruit [16]

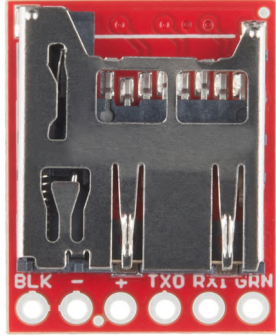
(c) ADS1174 ADC

**Figure 3.4:** Images of sensors and ADC used

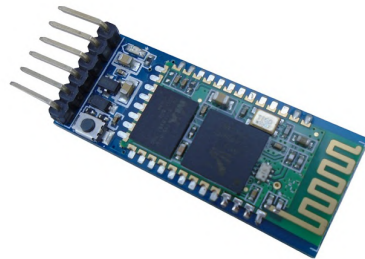
For logging sensor data, an OpenLog break-out board from Sparkfun is used. This board features an atmega328 microprocessor, which is used to write incoming UART serial data directly to a micro-SD card. This board was chosen as it is very simple to use and does not require any special firmware to interface with the PSOC. For wireless communication, a Bluetooth HC-05 module was chosen. Like in the case of the OpenLog, this was chosen due to its simplicity. The module is simple to connect a variety of Bluetooth devices, and can even function as a master device where it is possible to connect it to another HC-05 slave device. The module communicates using UART, and simply relays any wirelessly received data to any peripherals connected to its TX port. Similarly, it will transmit any

### 3.3. Hardware Choices

data send to its RX port to any device connected to it.



(a) Openlog board from Sparkfun [15]



(b) HC-05 board [17] [16]

**Figure 3.5:** Images of Logger and Bluetooth Module

To change the orientation of the projectile during flight, it is equipped with actuators connected to the tail fins. For this purpose, it is decided to use servo motors as they are simple to interface with using a microcontroller, they can be set to a specific angle, and continuous 360-degree rotation is not required. Due to the space limitations within the projectile, the SG51R servo motors were chosen. These were the smallest servo motors available for this project. Despite their small size, these motors have a stall torque of 0.6kg/cm (source) which should be enough for rotating a control surface.

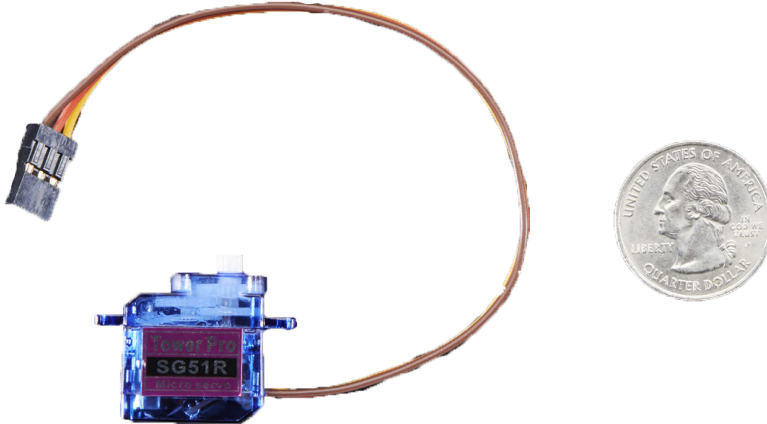


**Figure 3.6:** Picture of SG51R servo motor used [18].

#### 3.3.3 Printed Circuit Board

It is decided that all circuits must be made on printed circuit boards, as there is no other way to fit all the digital and analog circuitry within the projectile. Additionally, the used PCB's will help fulfil the low noise design requirements needed to successfully detect the IR diode at long distances.

#### 3.4 Conclusion of Part One

With the project scope defined and subsystems laid out, the individual subsystems and their functionalities can be designed. This is done in part two of the report, which focuses primarily on the theoretical and practical design choices made in order to fulfil the requirements. Additionally, the final implementation will be discussed, highlighting some of the issues faced in implementing the systems.

# **Part II**

# **System Design**

## Chapter 4

# Design of Ground Systems

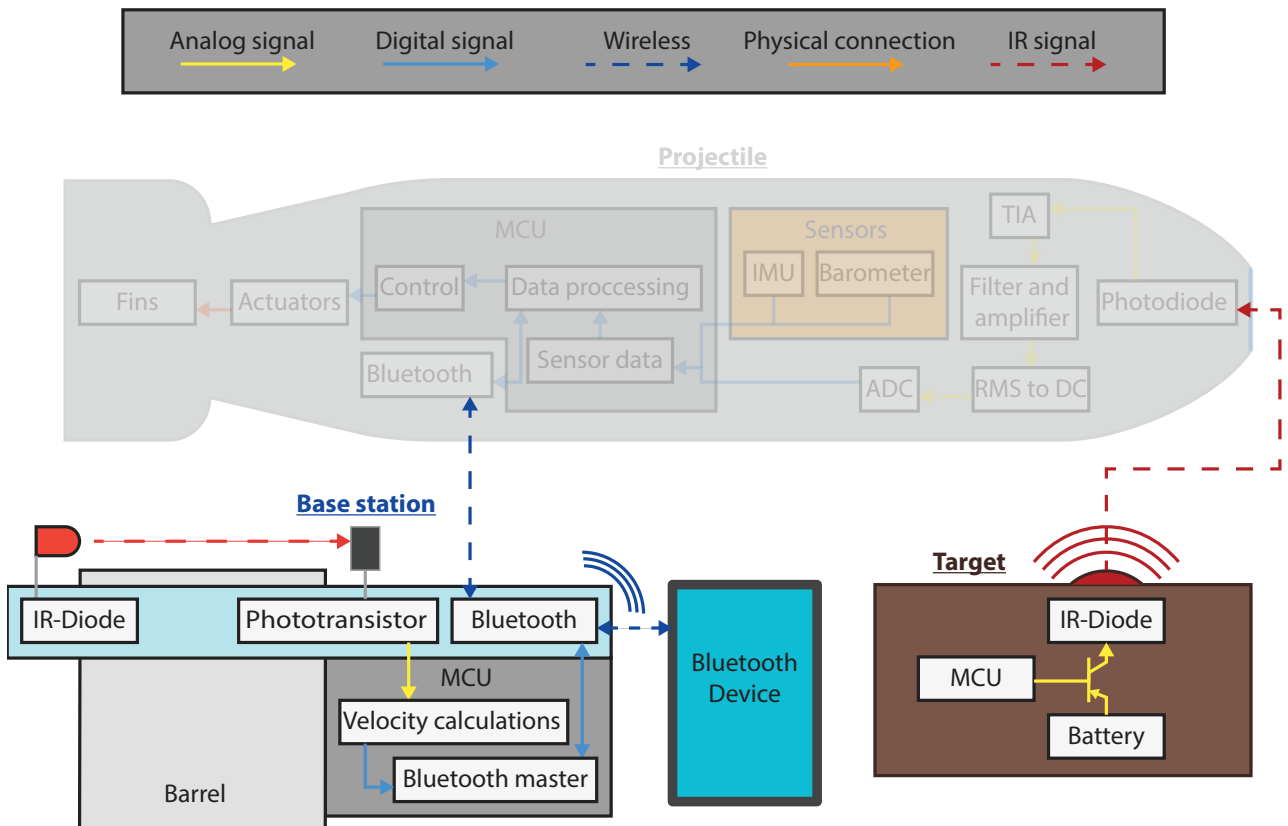
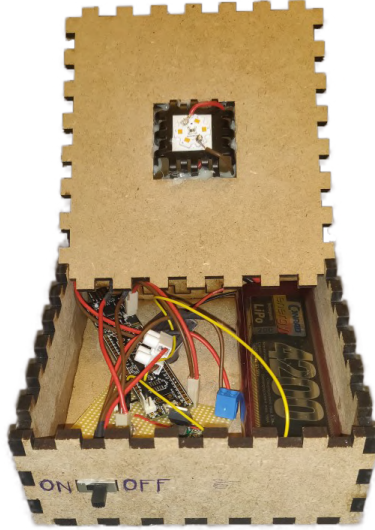


Figure 4.1: Illustration of ground system as part of the total system

This chapter focuses on the design of the ground-based systems. These include the target, the launcher and launch system and the base station.

#### 4.1. Target

Instead of using a laser pointing at a target, a box with an LED has been created. By creating an emitting LED as the target, allows the photodiode in the projectile to "see" the target, as it has become stationary. The LED emits light with a wavelength of 850 nm, which is in the infrared area of the light spectrum and cannot be seen by the human eye. The LED has a minimum forward voltage of 2.7 V and maximum of 3.7 V and generates a nominal output of 1.150 W [19].



**Figure 4.2:** Picture of the LED used as the target.

To power the LED a lithium polymer battery (LiPo) battery is used, the battery has a voltage output of 7.4 V and a capacity of 4200 mAh. As the LED has a maximum voltage of 3.7 V, the voltage needs to be stepped down. This is done with a DC-DC step down buckconverter, which takes the voltage of the power source down to a specified level. To distinguish the LED from other light sources a LED dimmer is made. This is done by using a PWM signal and transistor. To create a PWM signal a PSOC is used, which needs a power source of 5 V. To power the PSOC a LM1084 which is a 5 V regulator, it is used to step the voltage down from the same power source as the LED to 5 V. The transistor used for the dimmer is a BD137. As the system drains a lot of power and the battery has a limited capacity, it is desirable to be able to turn the system off when it isn't in use, an on/off switch has been added. On figure 4.3 the circuit of the system can be seen.

#### 4.2. Projectile Launcher

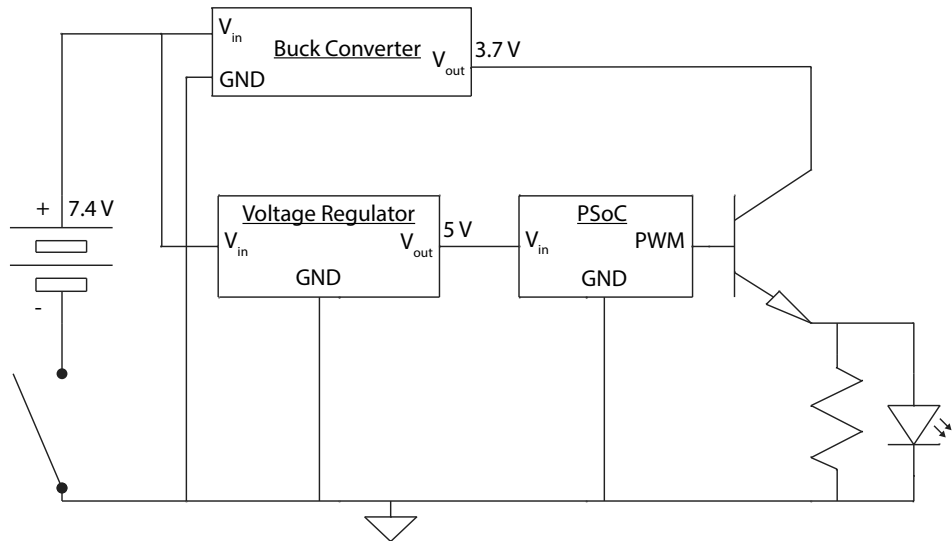


**Figure 4.3:** Circuit diagram of the LED circuit.

## 4.2 Projectile Launcher

The launcher of the projectile consists of a modified air compressor. The air compressor has a maximum pressure threshold of 10 bar.

To make the air compressor a projectile launcher, a 2-inch output hole has been made. On this output a 2-inch ball valve is connected followed with 2-inch pipes forming a barrel. The barrel has a length of 184 cm, and the angle of it is adjustable. As mentioned earlier the maximum pressure of the launcher is 10 bar, but it is possible to set the pressure at a specific level, by disconnecting the launcher from power. By having an adjustable pressure level, makes it possible to set the initial velocity of the projectile, and by changing the angle of the barrel, makes the initial direction of the projectile changeable.

#### 4.3. Gravity Assisted Launch System



**Figure 4.4:** Picture of the projectile launcher.

Figure 4.4 shows a picture of the projectile launcher. The handle of the ball valve is connected to a launch system called Gravity Assisted Launch System, which will be further described in section 4.3

### 4.3 Gravity Assisted Launch System

To fire the launcher from a safe distance, a system named "Gravity Assisted Launch-System", is created. This system consists of a rope, three pulleys and a 12 kg weight. The weight is a round 12 kg iron weight with a hole on the top of it to fasten the rope.

The weight is lifted approximately 1 m off the ground, so it has enough falling length to open the valve on the launcher. To make sure the weight doesn't strike from side to side it is fixed in place with pieces of wood guiding it to the ground. The weight is being held by a nail, which is pulled out with another rope making the weight fall from a distance.

#### 4.4. Base Station



**Figure 4.5:** Picture of the Gravity Assisted Launch System.

On figure 4.5 a picture of the system can be seen. The pulley placed in the bottom guides the rope to the launcher and is positioned so the weight only pulls until valve is near fully opened, making sure it doesn't stress the valve or valve handle by overturning the handle. The pulley on the top right guides the rope to weight.

## 4.4 Base Station

In addition to safely launching the projectile a desired distance, the launcher should also be able to measure the muzzle velocity of the projectile. To do so, a base station is added to the launcher setup, allowing this functionality. The reason for wanting to know the muzzle velocity is both for data logging and ensuring similar firing speeds, but also to wirelessly transmit the speed to the projectile. This is needed since the airspeed influences the transfer functions for modelling the projectile, and the projectile is not able to measure such high acceleration with its accelerometer. Furthermore, the base station can also be used as a communication platform for communicating with the projectile.

The base station itself consists of a microcontroller, capable of running a simple velocity measurement, as well as wireless communication with the projectile and e.g. a mobile phone as a user interface.

The main concern with the microcontroller itself is the speed at which it can measure the muzzle velocity, since this can be upwards of 50 m/s. This means that a projectile which is 300 mm long, takes just  $\frac{0.3}{50} = 6ms$  to pass a sensor setup. Since most modern microcontrollers can sample at frequencies over 1 MHz, this is not much of an issue.

### 4.4.1 Muzzle Velocity Sensor

The muzzle velocity sensor itself uses infrared photodiodes and phototransistors, to measure velocity. There are two ways of doing this, either using one or two sensor pairs. Using one sensor can be done by measuring how long the projectile is blocking the light from the diode, and the length of the projectile to calculate the velocity. Using two sensors works by measuring the time between the first and second diodes are blocked by the projectile, and the velocity can be calculated if the distance between the two sensors is known.

#### 4.4. Base Station

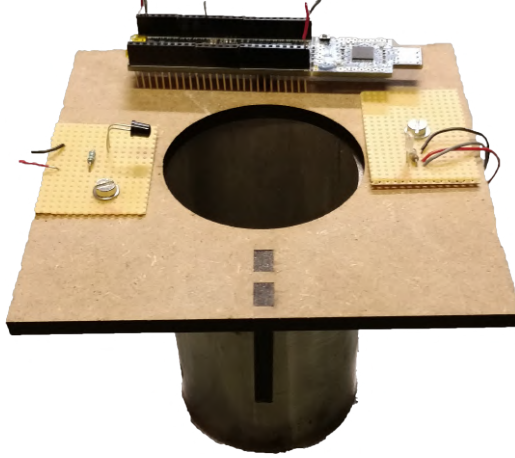


**Figure 4.6:** Illustration of base station setup

The second setup is more robust and versatile, since the projectile length does not matter. The disadvantage to this is the increase in physical complexity. Since two sensors are used, twice the wiring, ports and ADCs are needed. Additionally, the second sensor must be mounted further from the muzzle, which requires a fairly accurate build, since it should not hit the projectile, as it exits the launcher.

The advantage of the one sensor setup is simplicity, since only one sensor is needed, and it can be mounted directly on the muzzle. The disadvantage is that the projectile length must be manually updated. Since the projectile is designed precisely, and as such has a well-defined length, this is a minor nuisance, more than an actual issue.

It is chosen to use one sensor to save time on build complexity. The way the sensor is implemented is by using a comparator block, in the PSoC microcontroller, and comparing the voltage from the phototransistor to a reference. If the input voltage goes below the reference, an interrupt is triggered, and a timer is used to measure the time between the IR light is broken and unbroken. The speed is calculated based on the length of the projectile, and transmitted via Bluetooth, to the projectile.

In addition to the speed, a cyclic redundancy value is calculated based on CRC32, and transmitted to the projectile. The projectile generates its own crc code and compares the two. This is done to check for errors in the transmission, since an incorrect exit velocity can have negative effects on the control systems.

##### 4.4.2 Communication

As described briefly in the previous section, the base station would also allow for communication with the projectile before and briefly after launch. In addition to the transmission of the muzzle velocity, the base station serves as a relay for changing parameters of some of the systems, on board the projectile.

The base station is controlled via Bluetooth, e.g. from a phone, and allows the user to check and change parameters within the control system, in the projectile. Additionally, the user can also check and change the offsets on the actuators that control the wings, since these have some flexibility inherent from the connection with metal wires. Finally, the user can set the base station and projectile into "launch mode", which starts data logging in the projectile, and ready both systems for the muzzle velocity transmission. After calculating the projectiles muzzle velocity, the base station must immediately transmit the velocity and its complementary CRC32 value to the projectile. As the projectile

#### 4.4. Base Station

has been observed to fly at up to 50 m/s, and the HC-05 Bluetooth module has a maximum range of 10 meters [17], the velocity payload must be received at the projectile within 250 ms. This is shown to be very achievable, since at the slowest bitrate the base transmitted the eight bytes and received a response from the projectile in 40 to 50 ms.

# Chapter 5

## Projectile Design

This chapter covers the physical design of the projectile. these are the highlighted parts on figure 5.1.

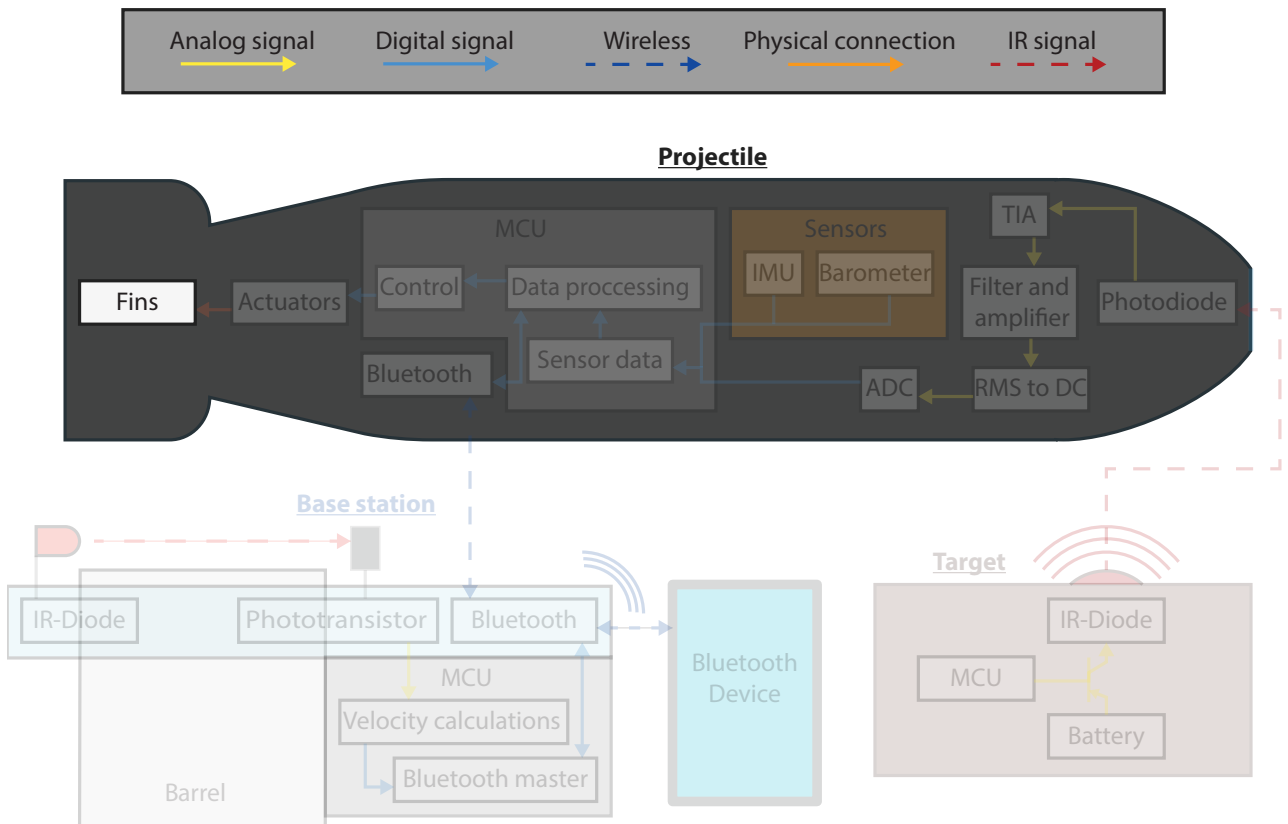


**Figure 5.1:** Illustration of the projectile as part of the total system.

First the requirements for the model are specified. Then an overview of the tools and background knowledge available are presented. With an overview of the tools and the problems to solve, the design process is subsequently explained.

## 5.1 Design Requirements

To make the final product, a physical model is designed. This model must fulfil a number of requirements for the product to be functional, the key requirements are as follows

- **Reusable:** To make it practical to work with the projectile it should be as reusable as possible and require as little maintenance between full system tests as possible. This is due to the time and resource constraints of the project.
- **Stable open loop system:** To greatly simplify the requirements for the control system, it is desired that projectile is stable in flight without any control applied to the system.
- **Steerable:** To control the projectile, the control system needs be able to affect the flight path of the projectile.
- **Room for electronics:** There must be room for the electronics to control the projectile.
- **Range:** As a long range is desired, it is desired to have as good aerodynamic properties as possible to reduce air resistance.

These are the main things that must be considered when designing the model.

## 5.2 Tools for Model Design

To construct the model multiple options were available. Due to the intended iterative approach of the design, it was decided early that the model should be done in 3D-print. There are numerous advantages of 3D-print. The main reason was that it was most easily accessible way of producing a model. And after some tests of the print durability it was decided to continue using 3D-print for all parts until another method was needed due to the limitations of the 3D-print available. A list of pros and cons has been compiled to show the limits of 3D-print:

Pros	Cons
<ul style="list-style-type: none"><li>• Good for complex models</li><li>• Good for medium to small models</li><li>• Good for prototyping</li><li>• Decent durability</li></ul>	<ul style="list-style-type: none"><li>• Bad for very small and larger models</li><li>• Has imperfections (aerodynamics)</li></ul>

These are properties of the 3D-printers. Since there was limited experience with designing aerodynamic models, it was also decided to do multiple iterations, to learn what works. With the above in mind, the choice was made for 3D printing design. For the software to create the 3D models, SolidWorks was used. It is a professional tool that is very powerful and versatile and is great for more complex assemblies.

### 5.2.1 Construction Materials

Using the 3D-printers, two materials are available, PLA and ABS. PLA and ABS are the most common materials for 3D-printing. They cost about the same per material. The materials are available on two

### 5.3. Design Methodology

different 3D-printers. To print PLA one of three printers could be freely used and the settings could be easily adjusted with the software. On the other hand, the ABS printer is not accessible directly by the students and the settings are limited. However, the ABS printer has better tolerances on the print and can create dissolvable support for the prints. A comparison of using PLA and ABS has been made.

PLA	ABS
Hard and brittle.	Softer but stronger and far more ductile
Biodegradable	Not biodegradable
Easy to print on free to use printers	Only printable on a supervised printer
Inconsistent and bad tolerances	More consistent and better tolerances and has dissolvable support for complex models
No cost other than materials and maintenance	Has a one-time use print plate that costs 60 dkk on top of materials and maintenance.
hard to get a smooth surface	Using acetone, the surface can be smoothed to an almost perfectly glossy finish

Based on this it is clear that PLA is good for prototyping, but that ABS is superior for the projectile as durability is important[20].

## 5.3 Design Methodology

Since the authors had no prior experience with aerodynamics, and it is not a priority for the studies, the design of the projectile is based on simple design rules based on a basic understanding of the topic. The design was based mostly on mimicking similar designs such as mortars, and then iterating the design based on empirical data from testing. This was decided as aerodynamics are a complex topic that are out of scope in this project.

### 5.3.1 Aerodynamics

This project is about the control of a projectile and not the aerodynamics. Thus, the aerodynamics of the projectile will not be studied in any depth. However, the aerodynamics properties are strongly impacting on the effectiveness on the projectile and will therefore have to be taken into consideration to some degree. Therefore a few simple principles have been considered when designing and producing the model. Firstly, the design is based on what is seen on other similar projectiles such as mortars; then it was desired to have as low drag and high stability as possible. To reduce drag, the main focus was the shape, as this has the greatest impact on drag. The effect from basic shapes is illustrated on figure 5.2. While designing the model a teardrop shape was the reference, as this provides the lowest drag coefficient possible. When the shape must differ from the teardrop shape, there is focus on reducing discontinuities on the surface and design as round corners as possible.

### 5.3. Design Methodology

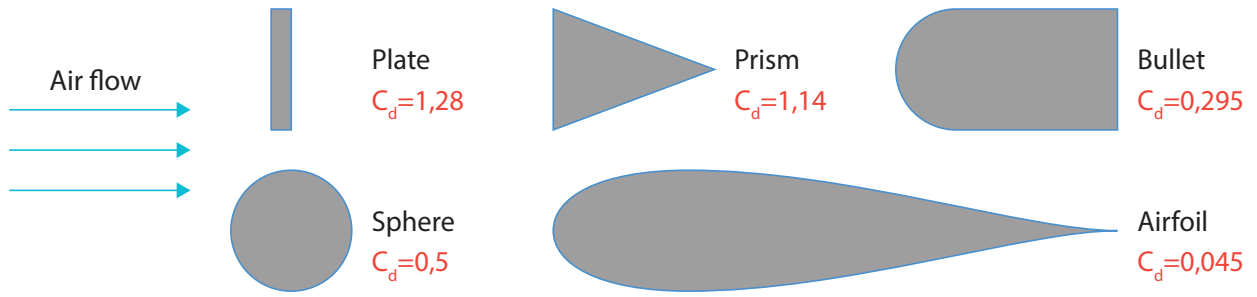


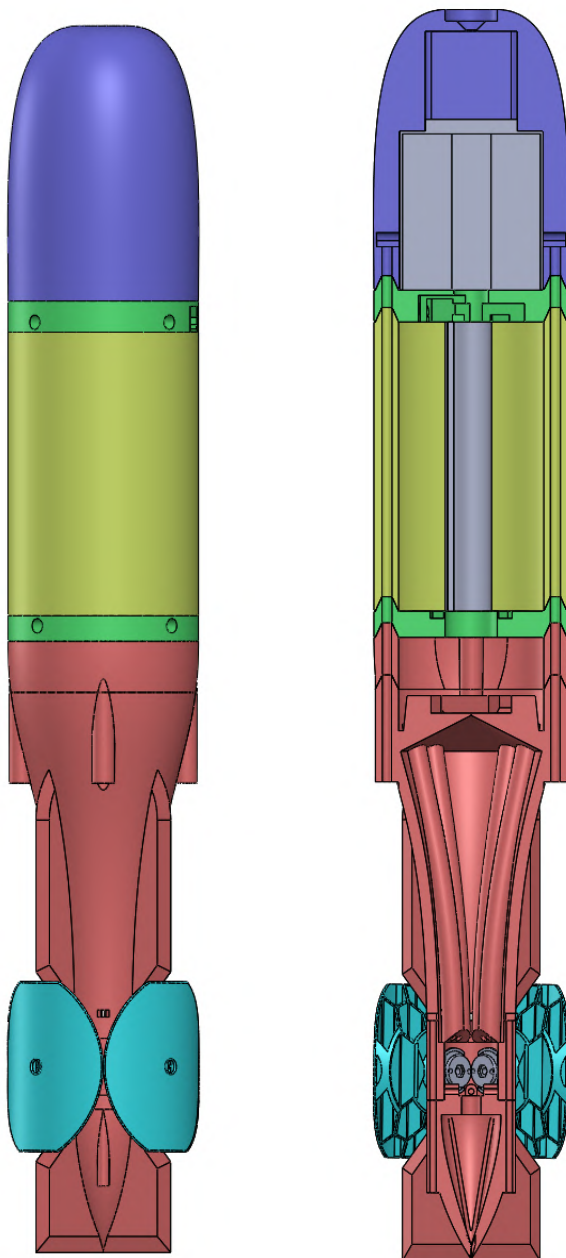
**Figure 5.2:** Overview of drag coefficients of common shapes with same frontal area[21].

There are challenges with producing rounded shapes with a 3D-printer on a very small objects, such as the edges of the wings. This will be to the best ability of the 3D-printer in use. The roughness of the surface is also worth considering. The 3D-print has natural roughness due to the layers. These layers can be smoothed with manual labour, either by sanding the surface, or in the case of ABS filament, using acetone. But this is not a priority due to time constrains. As stability was a priority, a simple principle was considered. To maintain stability in flight the projectile should have its centre of mass ahead of its centre of pressure[21].

The further these two points are apart the greater the stability. The centre of pressure is the sum of both drag and lift, and drag is undesirable anywhere. Thus, it is always attempted to get as much mass and as little lift towards the front of the projectile, and to have as much lift and as little mass as possible towards the rear end. Since drag also adds to the centre of pressure, it is more important with low drag in the front. While the drag is undesirable, it can be used in the rear to increase stability if needed, but this should be avoided as it is a trade off with range [21].

## 5.4 Design Overview

Before introducing the designs of the individual parts in the projectile, an overview of the projectile is presented.



(a) 3D-model of fully assembled projectile.  
(b) A section cut 3D-model of the full projectile.

**Figure 5.3:** An overview of the projectile modules. **Blue** part is the nose. **Green** part is the room separators. **Yellow** part is the body. **Red** part is the tail. **Cyan** parts are the wings. **Gray** parts are other 3D-models designed.

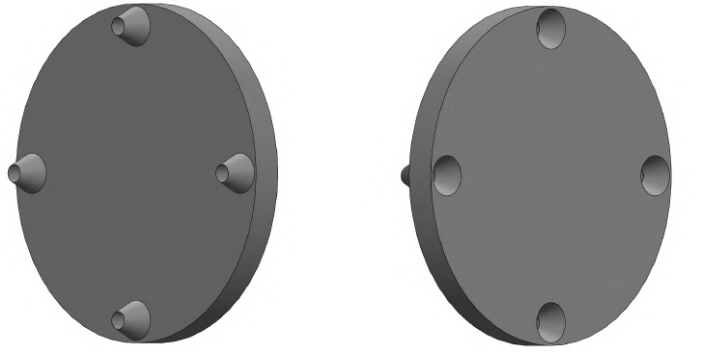
On figure 5.3 the full assembly is shown with highlights of the individual parts and their functions. First the design of the assembly interface will be explained, after which each part be explained starting from the top. The whole projectile is designed to fit in the barrel of the launch system which has a diameter of 68.6 mm. To ensure that the projectile fits the barrel even if there are small imperfections

## 5.5 Assembly Interface

on its surface, the outer diameter of the projectile is chosen to be 67 mm.

### 5.5 Assembly Interface

It was decided to design the projectile as a modular assembly. This required an interface between the modules. To provide extra strength for the design it was decided to add four through-going threaded rods. These provide tensile strength and keeps the modules together by compression. To avoid twisting, an interlocking pattern was used where the modules are connected, as seen on figure 5.9.



(a) Top part of interface. (b) Bottom part of interface.

**Figure 5.4:** The interface between the different modules of the projectile.

The rods are fastened in both ends with nuts. The holes for the rods and nut can be seen on the section cut on figure 5.3(b).

### 5.6 Nose Design

When designing the nose there was a few design goals. First it must contain the photodiode along with its analog circuits, as well as the batteries. It is in the front and affect the centre of pressure and centre of mass greatly. Thus, the drag and weight is important. Additionally, since the nose is what hits the ground it should be the most durable part of the projectile, in order to be reusable. On figure 5.5(a) is the model of the nose. On figure 5.5(b) is a model of the battery container. The batteries are easily placed inside, and on top there is room for the photodiode PCBs. The container is then slid into the nose.

## 5.6. Nose Design

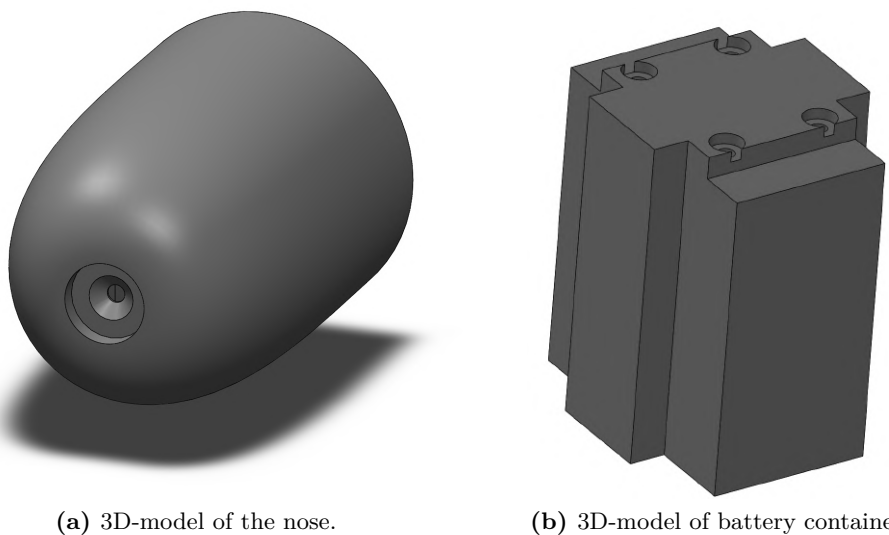


**Figure 5.5:** 3D-models of the nose and battery container.

When the sled is inserted into the nose it is held in place by the compression of the through-going rods and the room separators. As seen on figure 5.6 this provides a compact design. The nose is 3D-printed in solid ABS and therefore has good durability. With the mass of the batteries it has good weight which helps with the centre of mass. To further improve stability the nose is designed with as little drag as possible. Because the nose has such a large impact on the aerodynamics the printed model is sanded to smoothen the surface.

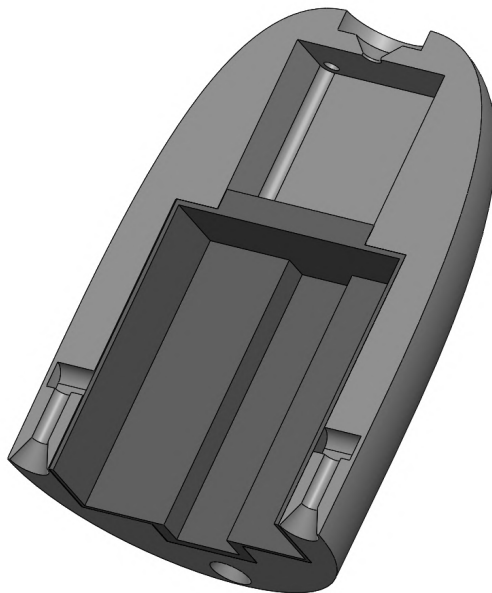
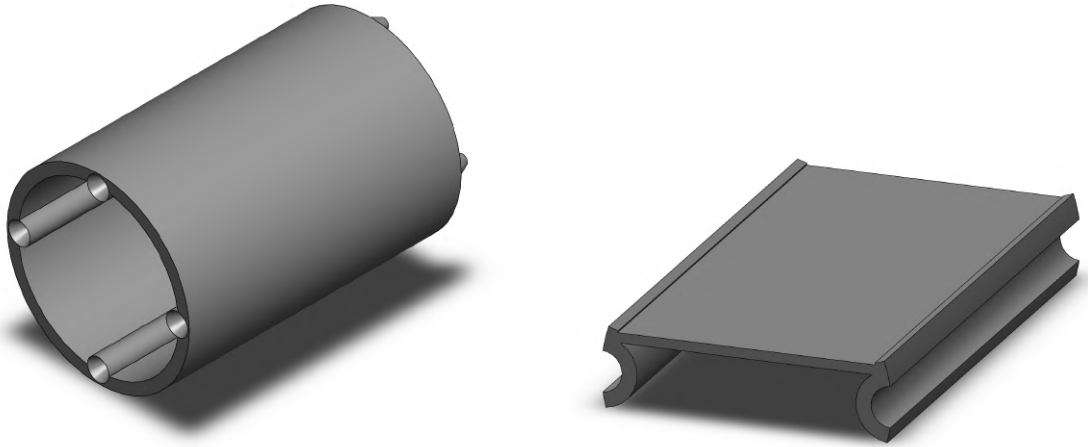


**Figure 5.6:** Section cut 3D-model of the nose with battery container.

To protect the photodiode, a cut-out for a piece of acrylic is at the very tip.

## 5.7 Body Design

The body of the projectile must contain the main part of the electronics. After early testing, it was determined that the body did not have problems with durability. Thus, it was designed to have as thin walls as possible, as seen on figure 5.7(a).



(a) 3D-model of the body for the projectile.

(b) 3D-model of the attachment plate for electronics.

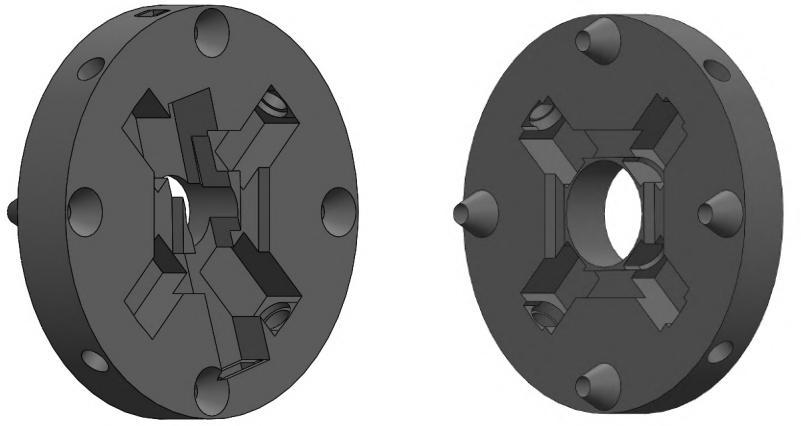
**Figure 5.7:** 3D-models used for the body.

The plate on figure 5.7(b) is designed to be modified based on needs. Therefore, any mounting holes are not printed as they are subject to change and are very easy to fix with a drill. The place is offset from the centre as one of the PCBs require more space than the other.

## 5.8 Room Separator Design

The room separators are custom parts that serve multiple miscellaneous functions. They provide barriers between the modules and can be used to mount parts. Additionally, they give strength to the construction. They are both flat on the side away from the body, and are used for mounting of LEDs, USB-port and a switch. Where pass-through holes are needed, a drill is used.

## 5.9. Tail Design



(a) 3D-model of top room separator.      (b) 3D-model of bottom room separator.

**Figure 5.8:** Both room separators are similar but serve different purposes.

Apart from the LED mounting holes, the top separator holds the batteries in place and has mounting holes for the power button and the mini-USB. The bottom separators main purpose aside from LED mounting, is to hold the servos in place.

## 5.9 Tail Design

The tail seen in figure 5.9(a) is the most complex model to build for the projectile and has numerous key functions to fulfil.

## 5.9. Tail Design

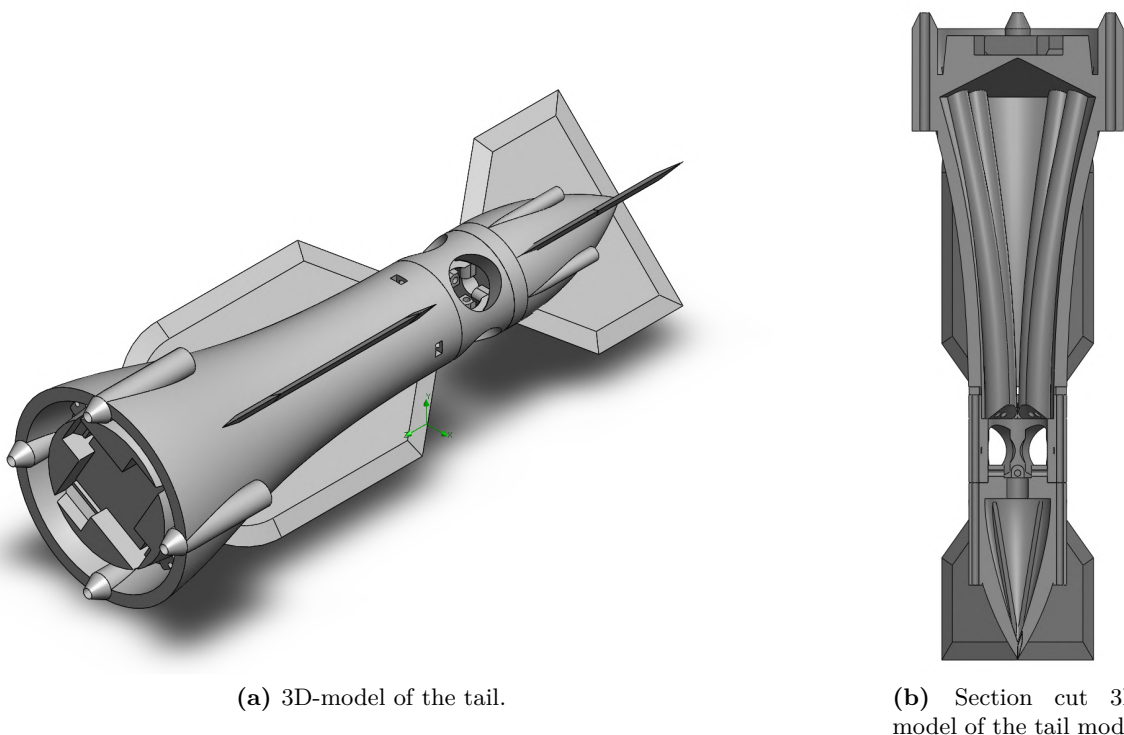


**Figure 5.9:** 3D-models of the tail.

The tail must provide stability and a way of attaching movable wings for control, while also being durable enough for reuse. To provide stability in flight a few things can be done. First, as much wing area as possible is wanted and as little weight. To increase the wing area, additional static fins are added. Another tail is added at the end to approximate the teardrop shape, and whilst adding more fins. For the wing area to have more effect on the centre of pressure, the tail was designed to be as long as practically possible and to move wing area as far rearward as possible. To reduce mass, most parts are hollow. The hollow structure can be seen on the section cut on figure 5.9(b). To add to the durability and to mount the tail, the same method used to assemble the modules are used with a smaller rods and nuts. This also adds durability to the weakest region of the tail where the bearings are inserted. This was deemed necessary based on early tests. To make sure the wings can be connected sturdily, while also being free to rotate controlling the direction, they were attached to the tail with ball bearings as the interface. To connect the wings to the bearings and the wires, a 3D-printed pin was designed, as seen on figure 5.11. The pin can be fastened using an M2 nut and bolt.

## 5.9. Tail Design

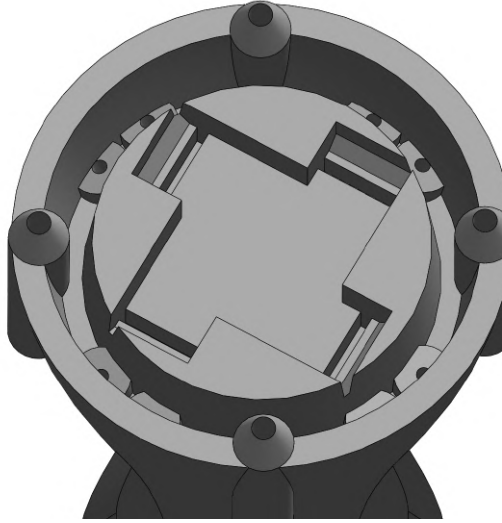


**Figure 5.10:** The imprints of the servos for mounting.

The bolt provides great strength for the otherwise thin and fragile 3D-print. Two holes are added to the pins to connect the wires. To fit a servo for all four wings into the limited space in the tail, the smallest servos available were used and placed in the most compact configuration. Due to the ease of making custom complex models with 3D-print, it was decided to make the mounting space for the servos according to an exact 3D-model from the manufacturer. This ensures that the servos fit perfectly into the tail, and the result looks like an imprint of the servos, as seen on figure 5.10. The servos are then held in place by the room separators.

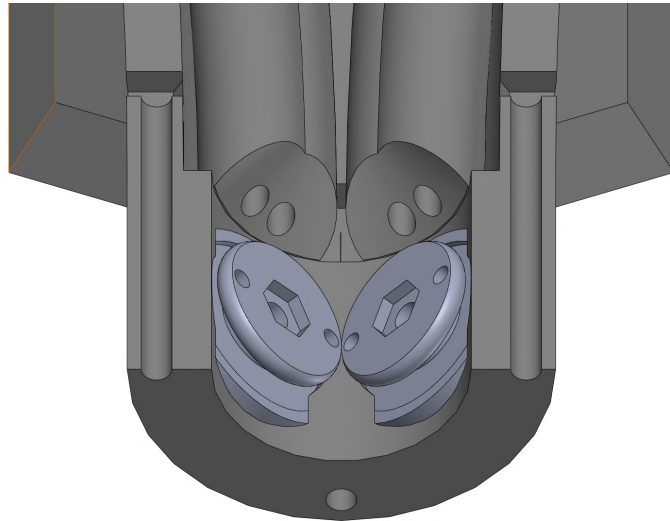


**Figure 5.11:** Section cut 3D-model of the wing connector of the tail model.

To connect the servos to the wings it was decided to use stiff metal wire. For minimum slack on the steering it was decided to use two wires for each wing, to both push and pull. Again, due to the easy construction of complex shapes, the wires were guided by tubes, along the wall of the tail, from the servo to the wings. The tubes can be seen on the section cut of the tail on figure 5.9(b), the holes for the servos can be seen on figure 5.10, which connects in the wing connectors on figure 5.11. To ensure that the pin and wing are rotationally locked once fastened an interlocking pattern is added to the end of the pin and the pin on the wings.

## 5.10. Fin Design

The main things to consider when designing the fins are wing area, durability and torque required to rotate the wing. A grid fin offers great performance in all these factors [22]. Therefore, the grid fins are the design implemented, as seen on figure 5.12.

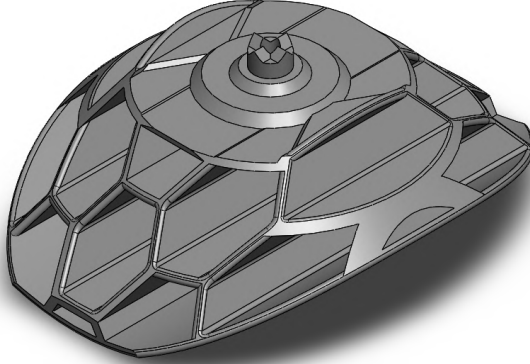
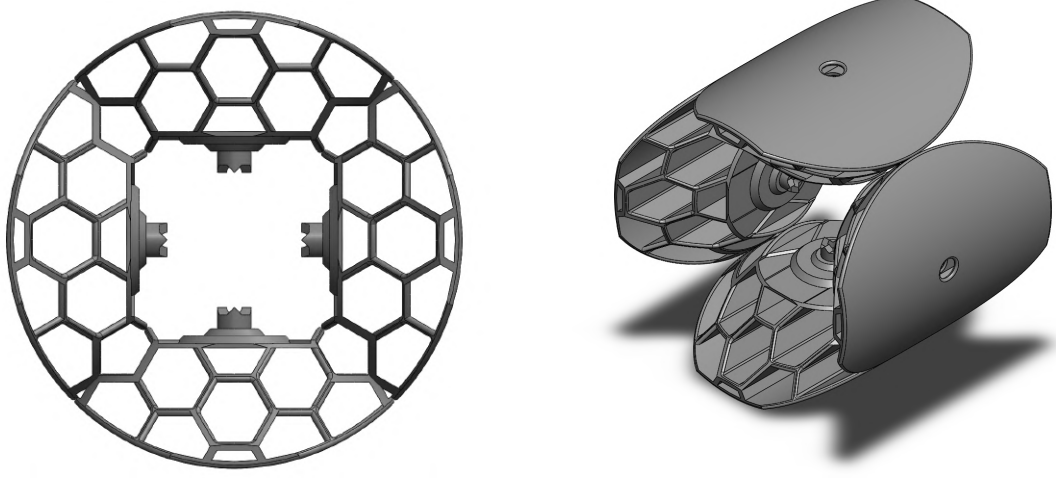


**Figure 5.12:** 3D-model of the fin design.

The grid fins provide greater angle of attack (AOT) before stalling. They have far superior strength, and a honeycomb pattern was used to provide the best durability. This was again possible because 3D-printing was used. Another advantage is that they require significantly less torque to rotate, which is desired due to the speed improvement of the small and relatively weak servos. The disadvantage of the grid fins is their worse drag to lift ratio than traditional fins. However, while drag reduces range, it also improves stability, since the wings are placed in the rear of the projectile, and therefore moves the centre of pressure towards the rear. The grid fin can offer great wing area in a compact design. This is important as the fins have limited size as they must fit in the diameter of the barrel. The wings are also designed to be as big as possible while also being able to fully rotate independently of each other. An illustration of the space utilisation can be seen on figure 5.13.

## 5.10. Fin Design



(a) Front perspective of the fin 3D-models.

(b) Angled perspective of the fin 3D-models.

**Figure 5.13:** 3D-models of the configuration of the fins.

If the max effective AOT is known, the fins can have a longer design with more wing area. However, it was not known at time of design, and was descoped.

# Chapter 6

## Design of Direction Detection System

This chapter details the design process for the circuitry used to detect the relative position of the projectile compared to the target. These are the highlighted subsystems in figure 6.1.

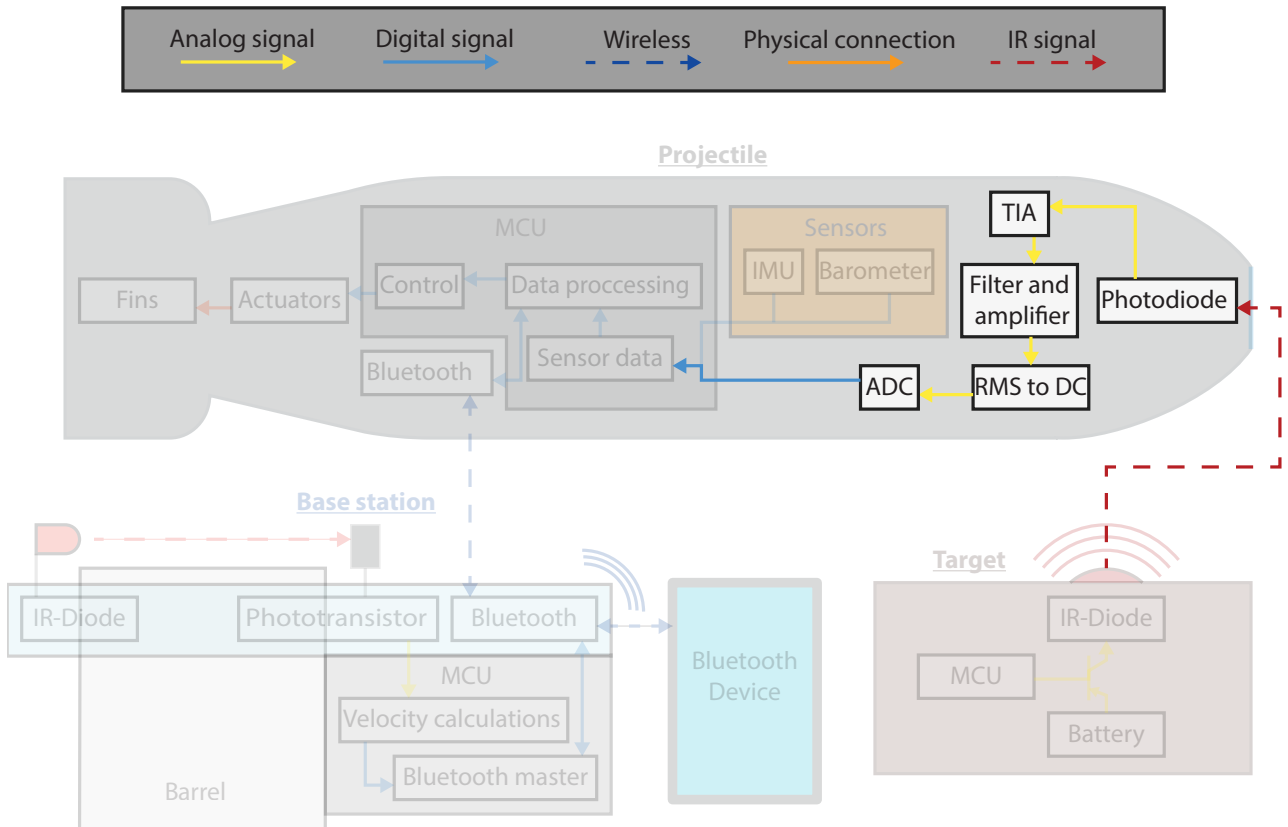


Figure 6.1: Illustration of the direction detection system as part of the total system.

Firstly, the direction detection theory for quad photodiodes is explained and a list of requirements for the circuits is created. Following this the aperture and focal lengths required for the pinhole which goes on top of the quad photodiodes are derived. Subsequently it is described how the target diode is pulsed at a fixed frequency to improve detection range. Finally, the design of the various circuit elements is implemented. The analog and digital systems are split this way to play to each of their

## 6.1 Direction Detection Theory

strengths. The analog systems amplifies and filters the input signals before they are processed by the MCU. This chapter only focuses on the analog systems.

### 6.1 Direction Detection Theory

To determine the position of a light spot with respect to the centre of the quad photodiode the relative intensity of light striking each diode is used. Equation 6.1 is used to calculate the X and Y components of the position [23]:

$$X = \frac{(A + D) - (B + C)}{A + B + C + D}$$

$$Y = \frac{(A + B) - (C + D)}{A + B + C + D} \quad (6.1)$$

Where A, B, C, and D represent the intensity of light on each of the four photodiodes as shown in figure 6.2 :

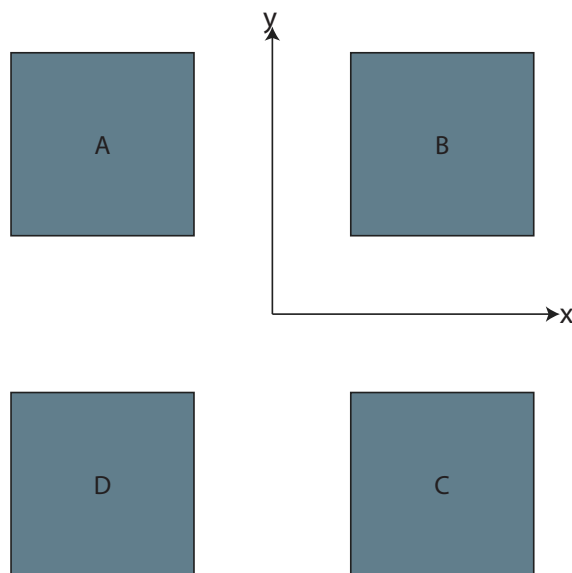


**Figure 6.2:** Illustration of the quad photodiodes and their labels and axis matching that of equation 6.1.

However, if this method is to be used the light from the target must be able to hit each photodiode individually, in order to discern the targets direction. If the projectile is pointed directly at the target, the light intensity from the target would strike the four photodiodes equally at the same time. Thus, it is necessary to focus the light into a more precise beam to be able to detect the direction and thereby the location of the target. To do this a pinhole is placed in front of the photodiodes.

## 6.2 Design of Pinhole

The design of the pinhole depends on three properties; shape, size and distance from the photodiodes. Each of these properties have some influence on the others, thus some choices must be made before final values can be determined. A choice is made considering the size of the pinhole, based on measurement accuracies. Through geometry and trigonometry, the different properties can be derived. For an in-depth analysis of the pinhole properties and their calculations, see appendix A.

The result of the analysis is that the pinhole needs to be circular with a radius,  $r$ , of approximately 1.2 mm and at a distance,  $L$ , of approximately 0.3 mm. An illustration of the photodiodes with an overlay of the pinhole can be seen on figure 6.3.

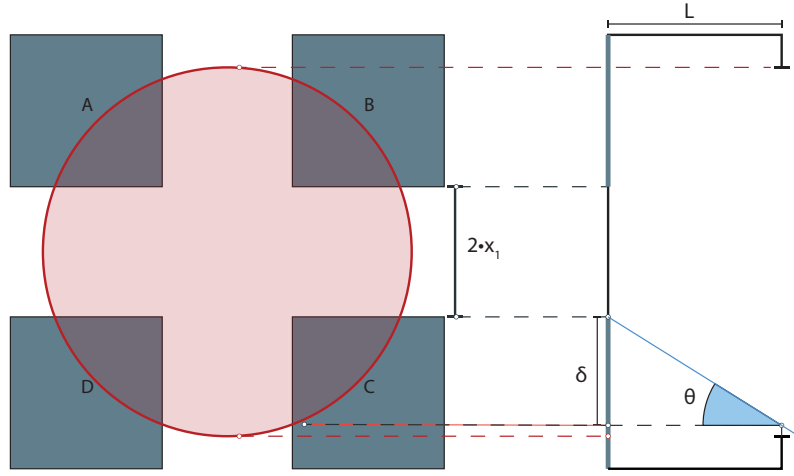


**Figure 6.3:** Illustration of photodiodes with circular pinhole overlay, seen from above and from the side.

However, these are very small measurements for practical use and thus realistically only approximations of these can be obtained. This creates some variations between the theoretical design and the practical implementation, to be countered by the controller.

## 6.3 IR Pulse Modulation

Another challenge to overcome is to isolate the IR diode's light from that of surrounding noise sources. While the target diode is matched to the photodiode sensor's most sensitive wavelength of light (850 nm), the photodiode has a very wide sensitivity range, which among others includes the visible light spectrum. Due to this, environmental light sources, such as the sun or common street lamps have the potential to saturate the circuitry or interfere with the accuracy of the direction detection logic.

One way to overcome this would be to use optical bandpass filters. However, as these are very expensive and thus outside of the project budget range an alternative is needed. Instead the target diode is pulse modulated. This does not change how the photodiode sensor sees the target. However, it allows for the use of filters to isolate the light from the target diode. This is because most outside light sources are near DC frequencies. By modulating the target diode at a high enough frequency, a bandpass filter can be used to isolate the modulated signal from out of band noise.

The target diode is pulse modulated at 10 kHz. This is done to move the signal far enough away from DC, allowing for the filtering of the signal. The reason that a higher frequency was not chosen is that

#### 6.4. Circuit Requirements

the opamps used in the photodiode amplification stages have a higher gain here, and that the RMS to DC converter's accuracy quickly deteriorates for small voltages above 10 kHz. The final frequency will be tuned based on the implemented filters, but 10 kHz is used for designing the filters.

The PWM signal used for this is generated by a PSoC. However, a PSoC cannot directly power the target diode, as this requires 1 A of current, while the PSoC can only deliver 8 mA. To circumvent this a transistor is used. This transistor is placed between the battery and the diode. As mentioned earlier, the diode must discharge between pulses. Since the transistor is closed between pulses, the diode cannot discharge properly and the PWM signal does not reach zero before the next pulse. To ensure the diode can discharge, a resistor is placed in parallel with the target diode. The resistor value can be calculated from the internal capacitance of the diode, the charged voltage level and the time it has to discharge. This is not done since it is not an integral part of the project and is found to work satisfactorily with a  $210 \Omega$  resistor. The final circuit can be seen on figure 4.3.

## 6.4 Circuit Requirements

Before the direction detection circuits can be designed, gain and filtering requirements must be established. These are calculated with respects to the desired maximum range at which the direction detection system should accurately be able to establish the relative position of the IR target. It is decided that the direction detector should have a maximum range of 100 meters.

Using the established range, the output current of a single photodiode at the given range is calculated. To do this, the power emitted from the IR target must first be determined.

The chosen IR LED emits  $P_{on} = 1.375 \text{ W}$  when turned on. However, as it is pulse modulated with a duty cycle of 50% the effective power output is limited to half of that,  $P_{square} = 0.6875 \text{ W}$ . Furthermore, as the signal is modulated as a square wave only the power contained in the 10 kHz fundamental harmonic is of interest as the other harmonics are suppressed by bandpass filtering. To find the power contained in the fundamental, a general form for the power ratio between the fundamental and PWM signal with 50% duty cycle is first derived as an intermediate step. A 50 % duty cycle PWM signal can be modelled as a square wave with an voltage amplitude,  $V_A$ , and a DC offset equal to the amplitude. This is illustrated in figure 6.4 :

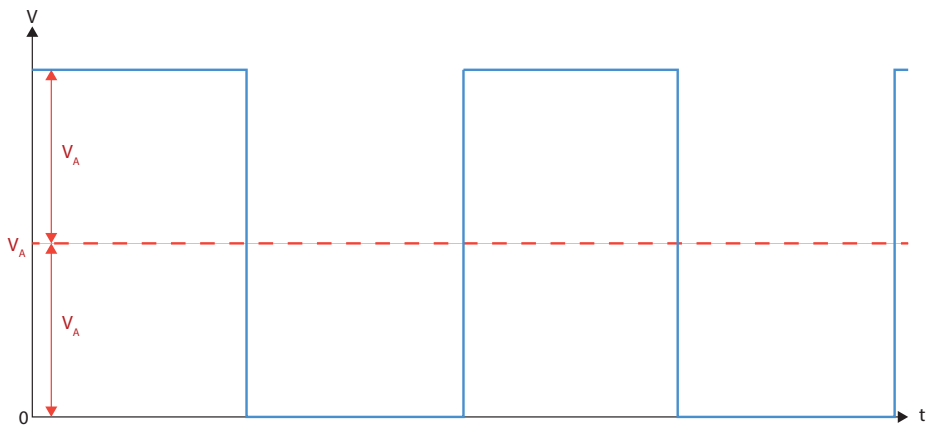


**Figure 6.4:** Illustration of the characteristics of a 50% duty cycle PWM Signal.

From this it should be evident that the average power dissipated across a given load  $R$ , can be expressed

#### 6.4. Circuit Requirements

as:

$$\begin{aligned} P_{\text{PWM}} &= 0.5 \cdot \frac{(2 \cdot V_A)^2}{R} \\ &= \frac{2 \cdot V_A^2}{R} \end{aligned} \quad (6.2)$$

The Fourier coefficients of such a signal are known to be:

$$\begin{aligned} a_0 &= V_A \\ a_n &= 0 \\ b_n &= V_A \cdot \frac{4}{n\pi} \cdot k \begin{cases} k=0, \text{ for } n \text{ even} \\ k=1, \text{ for } n \text{ odd} \end{cases} \end{aligned} \quad (6.3)$$

From this it can be seen that the fundamental has an amplitude of  $A_{\text{PWMfundamental}} = b_1 = V_A \cdot \frac{4}{\pi}$ . To simplify the power calculations the RMS value is found:

$$\begin{aligned} A_{\text{RMSfundamental}} &= \frac{A_{\text{PWMfundamental}}}{\sqrt{2}} \\ &= \frac{V_A \cdot \frac{4}{\pi}}{\sqrt{2}} \end{aligned} \quad (6.4)$$

The power across a load can now be expressed as:

$$\begin{aligned} P_{\text{PWMfundamental}} &= \frac{A_{\text{RMSfundamental}}^2}{R} \\ &= \frac{(V_A \cdot \frac{4}{\pi})^2}{2R} \\ &= \frac{V_A^2 \cdot \frac{8}{\pi^2}}{R} \end{aligned} \quad (6.5)$$

Now a relationship between the signals and its fundamental harmonics power can be established:

$$\begin{aligned} \frac{P_{\text{PWMfundamental}}}{P_{\text{PWM}}} &= \\ &= \frac{\frac{V_A^2 \cdot \frac{8}{\pi^2}}{R}}{\frac{2 \cdot V_A^2}{R}} \\ &= \frac{4}{\pi^2} \\ &\approx 0.405 \end{aligned} \quad (6.6)$$

Using this relation, the power contained in the fundamental of the PWM signal emitted from the IR LED is calculated:

#### 6.4. Circuit Requirements

$$\begin{aligned} P_{\text{fundamental}} &= P_{\text{square}} \cdot 0.405 \\ P_{\text{fundamental}} &= 0.278 \text{ W} \end{aligned} \quad (6.7)$$

The emitted power is distributed across the radiation pattern of the diode in the shape of a half sphere. While the LED does not emit light in a uniform distribution it is assumed to do so for the sake of simplifying calculations. The flux density at 100 meters of the power stemming from the fundamental frequency can be found as:

$$\begin{aligned} E_{\text{fundamental}} &= \frac{P_{\text{fundamental}}}{\text{Area}_{\text{Half sphere}}} \\ &= \frac{0.278}{2\pi 100^2} \\ &\approx 4.4 \text{ pW/m}^2 \end{aligned} \quad (6.8)$$

Now the output current of a photodiode can be calculated using its active area, the flux density, as well as the photodiodes responsivity. The responsivity is an expression for the output current as a function of optical input power and is given by the datasheet to be 0.45 A/W. Similarly, the area is given to be 0.75 mm<sup>2</sup>. The output current is expressed as:

$$\begin{aligned} i_{\text{output}} &= \text{Responsivity} \cdot \text{Area} \cdot E_{\text{fundamental}} \\ &= 0.45 \cdot 0.75 \cdot 10^{-6} \cdot 4.4 \cdot 10^{-6} \\ &\approx 1.5 \text{ pA} \end{aligned} \quad (6.9)$$

This is a very low current which is susceptible to interference and disturbance from noise. It has to be converted to a voltage and massively amplified to be detectable by the 16-bit ADC. As the output current of the photodiodes increases quadratically as they approach the IR target, the ADC is set to operate from zero to five volts, corresponding to its maximum full scale, so as to maximise the range that can be used for direction detection before the ADC is saturated. With a full scale of five volts the ADC's ideal resolution is 76 pV. To get the output current to this level it would have to be amplified by about 154 dB. However, this is the minimum ideal amplification required for detection, and does not take ADC-introduced noise and distortion into account. These imperfections affect the ADC's true dynamic range which is commonly expressed in terms of its effective number of bits (ENOB) [24]. The ENOB of the chosen ADC is not specified in its data sheet. However, as its SNR and THD are stated to be 97 dB and -105 dB respectively, its Signal to noise and distortion ratio (SINAD) can be calculated [24]:

$$\begin{aligned} \text{SINAD}_{\text{dB}} &= 20 \log_{10} \left( \frac{\text{Signal}}{\text{NoiseAndDistortion}_{\text{Total}}} \right) \\ &= 20 \log_{10} \left( \frac{\text{Signal}}{\sqrt{\text{Noise}_{\text{RMS}}^2 + \text{Distortion}_{\text{RMS}}^2}} \right) \\ &= 20 \log_{10} \left( \frac{1}{\sqrt{10^{\frac{-97}{10}} + 10^{\frac{-105}{10}}}} \right) \\ &= 96.36 \text{ dB} \end{aligned} \quad (6.10)$$

#### 6.4. Circuit Requirements

This in turn allows the ADC's ENOB to be found using the following equation [24]:

$$\text{ENOB} = \frac{\text{SINAD}_{\text{dB}} - 1.76}{6.02}$$

$$= \frac{96.36 - 1.76}{6.02}$$

$$\approx 15.7 \text{ bits} \quad (6.11)$$

$$(6.12)$$

This results in an effective resolution of 94  $\mu\text{V}$ .

This only takes ADC imperfections into account and does not consider noise or interference from other source, which could impact the measurements. Additionally, this analysis assumes that the entire area of a diode is struck by the IR light. But as a pinhole is required a large part of the diode area can be under shade at any given time and thus limiting its current output. Furthermore, if the photodiodes output signal is only amplified to the ADC's minimum resolution then the direction resolution is also limited and thus it is impossible to discern small direction changes. For all of the above-mentioned reasons the amplification should be much greater than the theoretical minimum requirement of 154 dB. The exact gain required to negate these effects has not been quantified and thus it is not possible to determine the minimum satisfiable system gain. However, to remain confident that above does not present any issues a conservative guesstimate has been made and the gain requirement for the system is set to 200 dB. This results in the 1.5 pA base current being converted and amplified to a voltage of 15 mV. While this gain makes it possible to detect the target 100 meters away, it will inevitably result in saturation at close distances, and thus limit the minimum range that the projectile is able to pinpoint the targets direction. From equation 6.7 it is seen that as the flux density changes quadratically with respect to the distance to the target. That is to say, the photodiodes current output will quadruple if the distance to the target is halved. Using this relationship an equation for finding the distance to the target where saturation occurs is formulated:

$$\text{range}_{\text{Saturation}} = \frac{100}{2^{\log_4(\frac{V_{\text{Saturation}}}{i_{100\text{Meters}} \cdot \text{Gain}})}}$$

$$= \frac{100}{2^{\log_4(\frac{5}{1.5 \cdot 10^{-12} \cdot 10^{10}})}}$$

$$= \frac{100}{2^{4.19}}$$

$$\approx 5 \text{ m} \quad (6.13)$$

This essentially means that the projectile will be unable to steer towards the target for the last five meters of its flight path. This is seen as an acceptable loss, as the theoretical maximum range achieved as a result of the added gain is much greater than the range lost.

Due to this large gain requirement it is critical that the first circuit stage is a large gain stage. This is done to keep the amplification required in later circuit stages to a minimum. This improves SNR, as the amplification of the noise introduced by the following circuitry is minimised. For similar reasons, it desired to design the circuit using as few components as possible to reduce the amount of noise being generated. In addition to improving the noise performance of the circuit, this is also needed to keep the circuit footprint to a minimum to ensure that it fits in the nose of the projectile.

#### 6.4. Circuit Requirements

No matter how much is done to optimise the circuit for noise immunity, noise will always be present in some capacity. Therefore, it is necessary to include narrow band bandpass filters to suppress this along with near DC components originating from environmental light sources. If this is not done the circuit is likely to be in a constant state of saturation. To match the fundamental frequency of the pulsed IR diode, the passband of the bandpass filter must be centred around 10 kHz. While the filter should attenuate all frequencies outside of 10 kHz, attenuation of lower frequencies is prioritised as environmental light sources can be orders of magnitude more powerful than the light emitted from the target IR diode. For example, on Earth, sunlight has a flux density of  $1300 \text{ W/m}^2$  [25]. This is approximately 170 dB greater than the flux density of the diode at 100 meters. Due to the presence of these large magnitudes at low frequencies, it is decided that the bandpass filter should be designed to nullify the required 200 dB gain at 1 Hz. In other words, the difference in magnitude between the 10 kHz passband and 1 Hz should be 200 dB.

Before the analog signal is converted to digital data, the signal is converted from RMS to DC. This is done to offload the MCU, since it would have to sample four channels of 10 kHz signals multiple times, convert the sampled signal to an RMS value and then use it for relevant computations. Using the RMS to DC converter lets the MCU sample at a much slower rate, leaving more processing power to relevant calculations.

Using the established requirements, the circuit can be designed. Figure 6.6 shows the final circuit design for a single photodiode (i.e the circuit will have to be built for each of the four diodes):

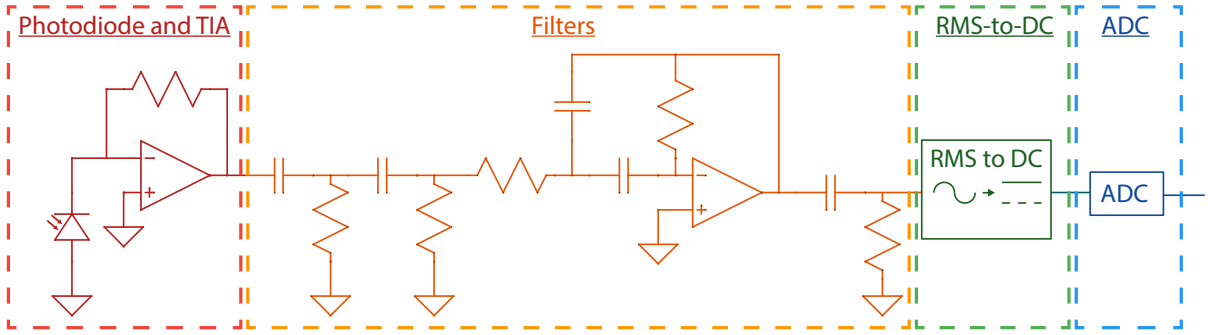


**Figure 6.5:** Complete Circuit diagram of a single photodiode channel

The circuit is comprised of four main sections:

1. The Photodiode and Transimpedance stage which converts and amplifies the photodiodes output current to a voltage.
2. The Filtering stage further amplifies and bandpass filters the signal.
3. The RMS-to-DC converter converts the 10kHz signal to a DC voltage equal to the RMS value of the signal.
4. The ADC converts the output voltage of the RMS-to-DC block to a digital signal that can be interpreted by the PSOC microcontroller.

The design of each of these sub-circuits is described in the following sections.

## 6.5 Photodiode and Transimpedance Amplifier

In this section, an introduction is given on the photodiode and current-to-voltage converter and amplifier. With the basis of the following introduction and the analysis found in appendix B the design of the TIA is completed in section 6.5.3. The design is based on the previously established requirements. Following, the design is tested.

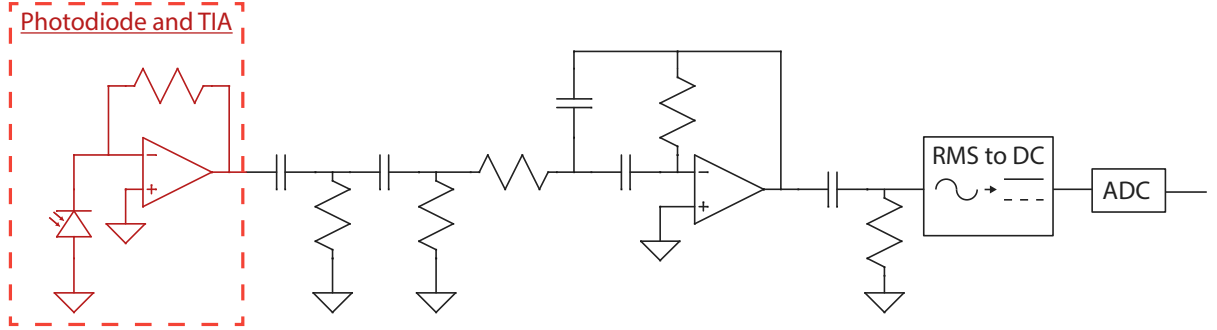


**Figure 6.6:** something

### 6.5.1 Properties of a Photodiode

Photodiodes operate electrically like normal diodes. However, when exposed to light they produce a current in the PN- or PIN-junction. Photodiodes can be forward and reverse biased or left unbiased. When a photodiode is biased it is referred to as photoconductive mode (or current output mode) and when it is left unbiased it is referred to as photovoltaic mode (voltage output mode) [26]. An example of photovoltaic mode is solar cells, which are very large photodiodes that produce an electricity. In both modes the photodiode produces a voltage and a current, however the voltage is highly nonlinear while the current output is proportional to the light radiated on the diode [26].

In photoconductive mode the width of the depletion region is increased by the bias voltage. This has a direct effect on the responsivity of the photodiode, which is greatly increased by the bias [27, p. 63-64]. The increased width of the depletion region also decreases the capacitance between the anode and cathode of the photodiode. [27, p. 64]. These improved properties of photoconductive mode results in a faster response time and better linearity, however there are also drawbacks to the mode. The required bias introduces offset and noise inaccuracies. The voltage source introduces a leakage current and voltage noise, which often surpasses that of the photodiode amplifier input. The errors introduced by the bias can be greatly reduced with passive R-C filtering, however this adds additional circuitry and complexity in the design [27, p. 64]. An unbiased photodiode is often preferred for low frequency light detection (below 350 kHz) and sensing of ultra low light sources [26]. For the photovoltaic mode, the current generated by the illuminated light shows superior responsivity against temperature variation compared to the photoconductive mode. In addition, the circuit is much simpler because there is no voltage supply or power supply filtering required [26].

A photodiode can be modelled using ideal components which results in the circuit which is shown on figure 6.7. The circuit consists of a current signal  $i_p$  in parallel with an ideal signal diode  $D$ , a capacitor  $C_D$  (the junction capacitance) and a resistor  $R_D$  (the shunt resistance) and finally there is also a series resistance  $R_S$ . The current signal is the photo-generated current and the diode is the PN-junction. The voltage output  $e_p$ , is a logarithmic function of light intensity upon the photodiode. The shunt resistance is between the two junctions of the diode and is for most diodes extremely high,

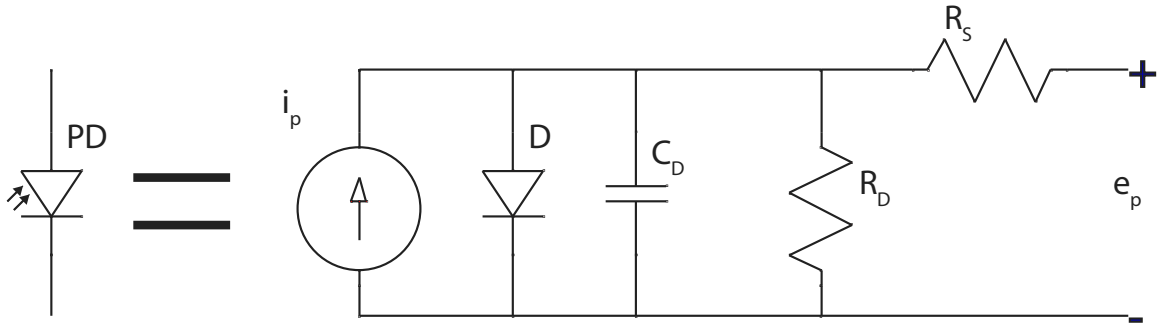


**Figure 6.7:** Circuit model of a photodiode

therefore it can be excluded from most analysis. Additionally, the series resistance is usually very low and can therefore also be excluded from analysis [27, p. 4]. Finally, the junction capacitance introduces the most significant performance effects by affecting the stability, bandwidth and noise of the photodiode and amplifier circuit.

### 6.5.2 Transimpedance Amplifier

As mentioned in the previous section, the voltage output of a photodiode is a logarithmic function and therefore highly nonlinear. Per contra, the current output is linear with the light intensity and exhibits much better offset and bandwidth performance than the voltage output. However, because instruments like ADCs monitor voltage variation and not current, it is necessary to convert the current output to a voltage signal. The current-to-voltage converter or transimpedance amplifier (TIA) in its simplest form consists of an operational amplifier (op-amp) and a feedback resistor  $R_f$ , as shown on figure 6.8. The TIA can practically eliminate both the voltage output and offset error which is produced by the photodiode. This is accomplished by the TIA which presents its virtual ground (a zero-load impedance) at its input to the photodiode. When the diode is presented with a zero-load input impedance it does ideally not produce a voltage across itself and the current can flow freely into the input of the amplifier without producing a significant voltage at the input [27, p. 23]. Now, with  $i_p$  at the input of the amplifier the feedback forces the amplifier to absorb this current and the high input impedance of the input converts this current to a voltage which in turn is amplified by the open-loop gain. Then, the amplified signal at the output of the amplifier is send into  $R_f$ , this diverts  $i_p$  from the photodiode to  $R_f$  which restores zero voltage at the amplifier input [27, p. 23].

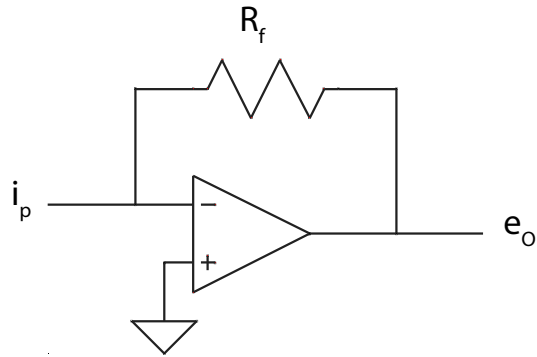


**Figure 6.8:** Circuit model of a simple transimpedance amplifier [27, p. 23]

While excluding any noise or offset components, the voltage output  $e_o$  of the TIA is determined by the input current  $i_p$  and the feedback resistor, as shown by equation 6.14 [27, p. 23].

$$e_o = I_p \cdot R_f \quad (6.14)$$

This concludes the introduction of the TIA operation, the next step is to analyse the bandwidth, stability and noise components of the photodiode amplifier circuit.

### 6.5.3 Design of the photodiode amplifier

Following the extensive analysis of the bandwidth, stability and noise components of the photodiode amplifier circuit in appendix B, the theory can now be implemented to assure that the designed circuit achieves its requirements. Additionally, the stability and noise analysis will help in the process of designing the best possible amplifier for the purpose of photo detection. In section 6.4, the stated requirements for the photodiode amplifier is that it must be able to amplify the signal by 200 dB with a gain bandwidth of at least 10 kHz. However, an early component selection of the OPA2380 as the op-amp for the TIA circuit limits its gain to a maximum of 140 dB at 10 kHz [28, p. 7]. This means a  $R_f$  of  $10 M\Omega$  must be selected. Then, to achieve the remaining and required 60 dB gain, an active filter is implemented which is designed in section 6.6. Due to very limiting space constraints, the circuitry must be as small as possible. Therefore, the photodiode is unbiased, and the current-to-voltage converter configuration is kept as simple as possible.

Assuring that the required bandwidth and stability is achieved requires further calculations. First, stray capacitance  $C_S$  of  $R_f$  is estimated at  $0.5 \text{ pF}$  [27, p. 32]. The bandwidth of the amplifier with the chosen  $R_f$  and approximation of  $C_S$  is calculated via equation B.1:

$$BW_t = \frac{1}{2 \cdot \pi \cdot 10 M\Omega \cdot 0.5 \text{ pF}} = 31.8 \text{ kHz}$$

This result meets the required bandwidth for the TIA and the selected  $R_f$  value. Now, the stability of the system can be verified. First, the photodiode must be selected so that the net input capacitance  $C_i$  of the TIA can be calculated. The chosen photodiode is an OPR5925 quad photodiode which has a  $C_D = 10 \text{ pF}$  with a bias of 10 V [29]. Due to the circuit operating the photodiode as unbiased  $C_D$  is then estimated to:

$$C_D = 0.75 \text{ mm}^2 \cdot 16 \frac{\text{pF}}{\text{mm}^2} = 12 \text{ pF}$$

## 6.6. Design of Analog Filters

This estimation is based on typical capacitance versus reverse bias graph and the area of a single diode of the OPR5925 [26]. Now,  $C_{id} = 1.1 \text{ pF}$  and  $C_{icm} = 3 \text{ pF}$  are found in the datasheet of the OPA2380, which along with  $C_D$  are summed in the calculation of  $C_i$ :

$$C_i = 12 \text{ pF} + 1.1 \text{ pF} + 3 \text{ pF} = 16.1 \text{ pF}$$

In the datasheet of the OPA2380 it is obtained that the unity gain bandwidth  $f_c$  of the amplifier is 100 MHz [28]. Now the required  $C_f$  to obtain stability is calculated:

$$C_C = \frac{1}{2 \cdot \pi \cdot 10 \text{ M}\Omega \cdot 100 \text{ Hz}} = 0.16 \text{ fF}$$

$$C_f = \sqrt{16.1 \text{ pF} \cdot 0.16 \text{ fF}} = 50.63 \text{ fF}$$

Here it is obtained that  $C_i \gg C_f$  holds true, thus the above  $C_f$  calculation is correct. In turn, it can be noted that because  $C_S$  is larger than  $C_f$  that the feedback loop of this circuit is stable.

Now with the designed circuit, it can be implemented on a PCB and tested. A test of the photodiode and TIA is carried out in appendix D and later the circuit is also a part of the test in appendix G.4. The conclusion of these tests is that the circuit functions as it should and that it can be implemented into the direction detector.

## 6.6 Design of Analog Filters

In order to ensure only the desired signal reaches the ADC for the control system, a filter is needed. This filter will primarily focus on removing low frequency signals, coming from the photodiode, as a result of daylight being near DC. In addition to this, an amplification of the desired signal, the modulated target diode light, is also necessary. Figure 6.9 shows the section of the analog circuit, which is to be designed.

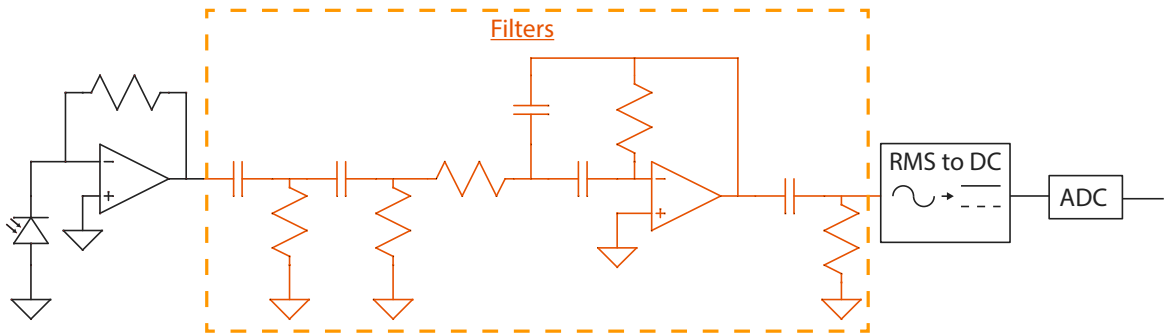


**Figure 6.9:** Illustration of the full analog circuit, focusing on the filter section.

### 6.6.1 Design Requirements for Analog Filters

The requirements for the filter are as follows:

- 200 dB or more attenuation at 1 Hz.
- 60 dB amplification at 10 kHz.

## 6.6. Design of Analog Filters

- Lower than 60 dB amplification outside 10 kHz.
- Sharp as possible passband.
- Only one active stage.
- Small as possible footprint on PCB.

These requirements come from wanting to eliminate low frequency signals, attenuate undesired signals outside 10 kHz and to amplify the desired signal enough for the ADC. The total amplification from the photodiode to the ADC must be 200 dB, therefore 60 dB is needed after the TIA stage, which amplified 140 dB. These numbers come from section 6.4. The requirement for only using one active stage, is to reduce noise. Reducing the component number of the filter is important since it is to be placed on PCBs in the nose of the projectile, as well as needing four channels.

### 6.6.2 Choice of Filter Types

To fulfil the requirements for the filter, an active bandpass filter can be used. Since only one active stage is allowed, this puts an upper limit on the order of the filter, in this case chosen to be second order. This is to reduce complexity of the filter design.

A second-order bandpass filter with a center frequency of 10 kHz cannot fulfil all the requirements on its own. This is due to only dropping 20 dB per decade, from the 60 dB at the center frequency. This means that the filter will only reach an attenuation of 20 dB at 1 Hz. This is 180 dB off, and to fulfil this requirement, additional passive high pass filters are used. For this, a simple RC ladder circuit is designed.

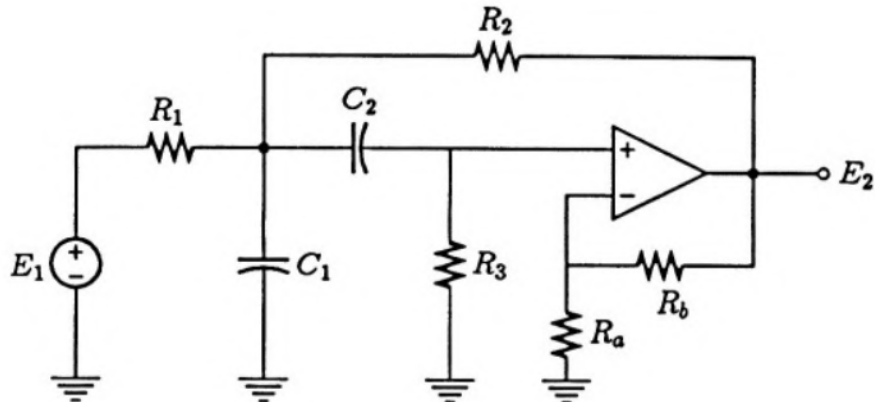


**Figure 6.10:** Circuit diagram of Active Sallen-Key bandpass filter topology [30].

The active bandpass filter type is chosen between a Sallen-Key filter or a multiple feedback (MFB) filter. Sallen-Key is a widely used filter topology, which is easy to design, however it uses two resistors to change the gain of the opamp. The filter topology also uses an extra resistor for the filter itself. The circuit of this filter can be seen on figure 6.10.

## 6.6. Design of Analog Filters

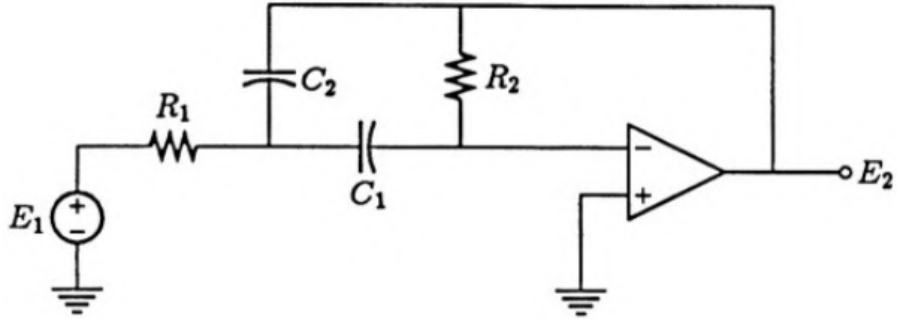


**Figure 6.11:** Circuit Diagram of Active MFB Bandpass Filter Topology [30].

An MFB filter, see figure 6.11, requires three less resistors than a Sallen-Key filter does, and is therefore the chosen filter topology. This decision is made since four filters are needed and thus results in a simpler PC layout with less components and less filter response drift due to component tolerances.

### 6.6.3 Filter Design

#### Passive highpass filter

Since an additional attenuation of 180 dB is needed, the order of the highpass filter must be chosen accordingly. To prevent the highpass filter from interfering with the bandpass filter, the cutoff frequency of the highpass filters are set to be at 1 kHz. This is one decade before the 10 kHz center frequency of the bandpass filter, and as such, the highpass filters should not interfere with it. This leaves three decades, from 1 kHz to 1 Hz, which means in order to provide an attenuation of at least 180 dB at 1 Hz, the order of the highpass filter must be three.

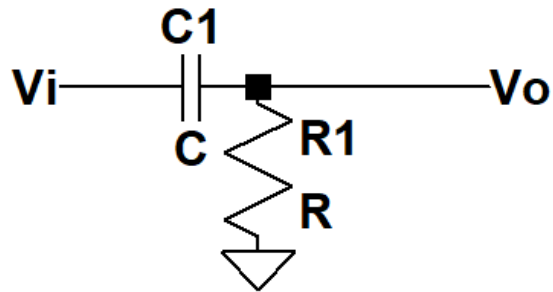


**Figure 6.12:** Circuit of an RC highpass filter.

The cutoff frequency of an RC highpass filter can be found by equation 6.15.

$$\omega_c = \frac{1}{RC} \quad (6.15)$$

To achieve a cutoff frequency of 1 kHz, equation 6.15 can be solved for  $\omega_c = 2\pi \cdot 1\text{kHz}$ . The equation has two variables, so one is chosen and the other calculated from this.  $C$  is chosen to be 10  $\mu\text{F}$ , to reduce the size of  $R$ . This is done to reduce the output impedance of the RC filter, to minimise

## 6.6. Design of Analog Filters

the interaction between the RC circuit and the active filter. 10  $\mu\text{F}$  is chosen since this is the largest available SMD capacitor easily available. The resistor value can now be calculated by equation 6.16.

$$R = \frac{1}{2\pi \cdot 1\text{kHz} \cdot 10\mu\text{F}} = 15.9\Omega \quad (6.16)$$

Using 10  $\mu\text{F}$  capacitors and 16  $\Omega$  resistors, the highpass filters can be implemented. 16  $\Omega$  is chosen since this is available as an SMD component. Two of the three highpass filters are placed in front of the bandpass stage, while one is placed after. The reason for this is to reduce the low-frequency signals from the TIA, since these have been amplified by 140 dB. Two highpass filters will attenuate this by 120 dB at 1 Hz and is done to ensure the opamp in the active filter does not clip. During experimentation with the filters, it was noted that having the highpass filters after the bandpass filter resulted in a sharper passband. This is likely due to imperfect impedance matching, which will be described further in section 6.6.3. Due to this, the final highpass filter is to be placed after the bandpass filter.

The last highpass filter is placed afterwards, which means it must be designed differently. This is because the highpass filter must have at least ten times greater input impedance than the output impedance of the bandpass filter. The output impedance of the bandpass filter is heavily influenced by the output impedance of the opamp. The chosen opamp is a TI084 [31], which does not have an accurate output impedance value in its datasheet. As such, a worst-case value is assumed, from other similar opamps, which is upwards of 100  $\Omega$ . This means the input impedance of the highpass filter must be at least 1 k $\Omega$ . The input impedance of an RC highpass filter can be found by equation 6.17.

$$Z_i = \frac{1}{sC} + R \quad (6.17)$$

Normally this would be in parallel with the load impedance, however the input impedance of the RMS to DC converter is  $10^{12}\Omega$ [32]. This means the load impedance is negligible compared to the impedance of the filter itself, when in parallel.

Using equation 6.15 and 6.17, the component values can be calculated. It is seen that the input impedance is frequency dependant, which is expected. Normally the output impedance of the previous stage is known as a frequency dependant value as well, and the two can be compared to ensure proper impedance matching. In order to ensure the input impedance of the highpass filter is always high enough, R is set to be 1 k $\Omega$ , which means C must be 160 nF to achieve  $f_c = 1\text{kHz}$ . However, this increases the output impedance of the highpass filter, which is not an issue since the ADC used has an input impedance of 28 k $\Omega$ . This means the output impedance of the highpass filter must be less than 2,8 k $\Omega$ . The output impedance of an RC highpass filter can be calculated using equation 6.18.

$$Z_o = \frac{R}{sCR + 1} \quad (6.18)$$

Looking at equation 6.18, it is seen that for DC the impedance is R, and for increasing frequencies, the impedance will drop. This means the output impedance for the highpass filter will never be higher than 1 k $\Omega$ . in the 10 kHz passband of the bandpass filter, the impedance of the highpass filter will be:

$$|Z_o| = \left| \frac{16\Omega}{j2\pi \cdot 10\text{kHz} \cdot 160\text{nF} \cdot 16\Omega + 1} \right| = 1,58\Omega$$

## 6.6. Design of Analog Filters

### Active bandpass filter

There are three main characteristics describing the MFB bandpass filter. These are:

- $f_c$ , denoting the center frequency of the filter.
- Q, denoting the sharpness of the passband.
- G, denoting the gain of the filter.

From the requirements of the filter,  $f_c$  must be 10 kHz, the gain must be 60 dB and as sharp as possible. In order to achieve this, the three equations for component values, are examined. These are equation 6.19 to 6.21 [30].

$$f_c = \frac{1}{2\pi R_1 R_2 C_1 C_2} \quad (6.19)$$

$$Q = \frac{\sqrt{\frac{R_2}{R_1}}}{\sqrt{\frac{C_2}{C_1}} + \sqrt{\frac{C_1}{C_2}}} \quad (6.20)$$

$$G = \frac{R_2 C_1}{R_1 (C_1 + C_2)} \quad (6.21)$$

Since the three equations have four variables, they cannot be solved on their own. In addition to the primary characteristics of the bandpass filter there are two others, which can be included to solve the equations. These are the in- and output impedances of the filter. It is chosen to only use the input impedance, since this must be matched correctly with the highpass filters. The equation for the input impedance of the bandpass filter can be seen in equation 6.22. The equation is derived from the circuit in figure 6.11 and the process is documented in appendix C.

$$Z_{in} = \frac{C_1 R_1 s + C_2 R_1 s + 1}{s(C_1 + C_2 - \frac{R_1(s^2 + (\frac{1}{C_1 R_2} + \frac{1}{C_2 R_2})s + \frac{1}{C_1 C_2 R_1 R_2}))}{s}} \quad (6.22)$$

To simplify the equation, it is assumed that  $C_1 = C_2$ . This is done to maximise the Q factor of the filter, which is the case when the capacitors are equal, which can be seen in equation 6.20. In theory, the three remaining equations can be solved to find the three component values. This proved to be more difficult than previously anticipated and yielded no useful results. Instead, the input impedance will be calculated after finding the component values.

In order to calculate the component values with the remaining equations, a value must be predetermined. During experimentation with the MFB filter topology, it was noted that the TI084 opamp did not work as anticipated, with capacitor values below 1 nF. As such, the capacitors are chosen to be 1 nF, since this allows for higher resistor values, which in turn improves input impedance.

Using this capacitor value, the gain will determine the relationship between the two resistors. This means finding the desired value for G, which is 60 dB, or 1000 times, as can be seen in equation 6.23.

$$G = 10^{\frac{60}{20}} = 1000 \quad (6.23)$$

## 6.6. Design of Analog Filters

Setting  $C_1$  and  $C_2$  equal to each other, and solving equation 6.21 for  $R_2$  gives equation 6.24.

$$R_2 = 2 \cdot R_1 \cdot G \quad (6.24)$$

Substituting  $R_2$  from 6.24 into equation 6.19 results in equation 6.25.

$$\omega_c = \frac{1}{\sqrt{2R_1^2 \cdot G \cdot C^2}} \quad (6.25)$$

Solving equation 6.25 for  $R_1$ , with  $G = 1000$ ,  $C = 1nF$  and  $\omega_c = 2\pi 10kHz$ , gives  $R_1 \approx 357\Omega$ . Using equation 6.24,  $R_2$  can be found to be  $714 k\Omega$ . With all component values calculated, the filter can be constructed and tested. Additionally, the input impedance is calculated using equation 6.22 at 10 kHz. The filter has an input impedance of approximately  $16 \Omega$ , which is ten times larger than the output impedance of the previous highpass filter, which is approximately  $1.6 \Omega$ , found by using equation 6.18. A simulation of the designed bandpass filter can be seen in figure 6.13.

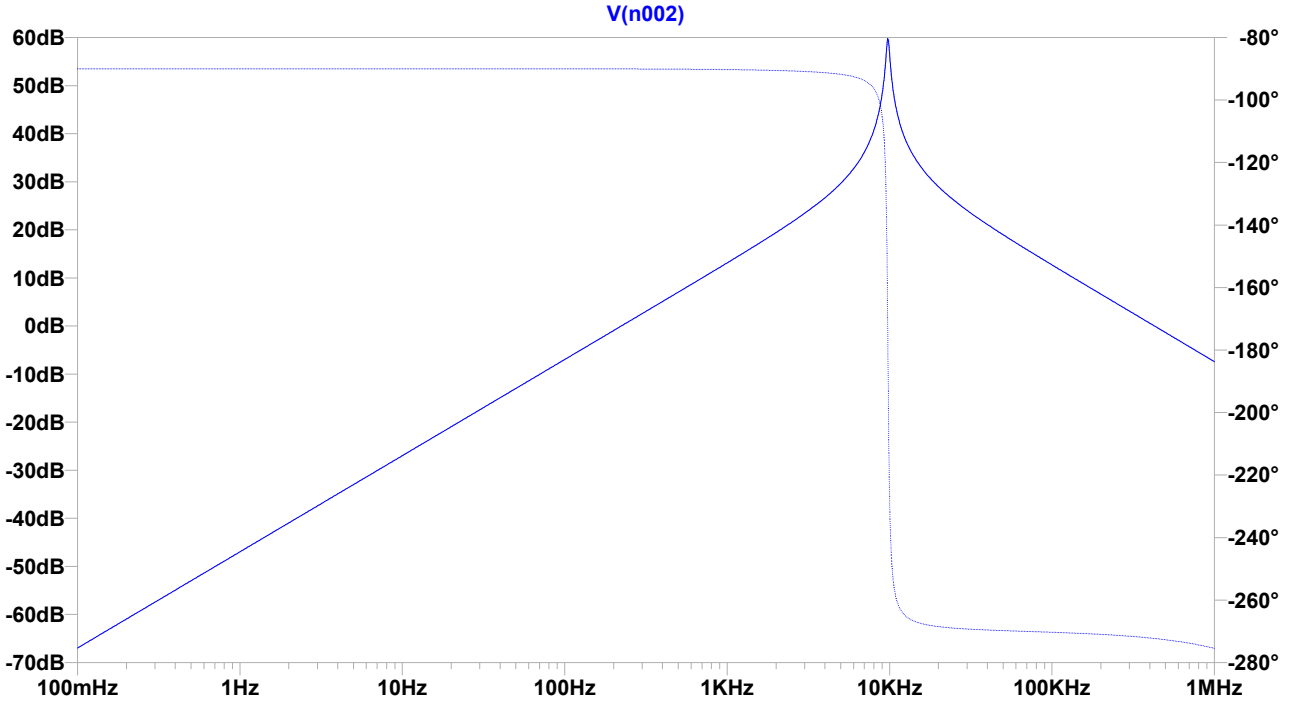


**Figure 6.13:** Simulation of the bandpass filter.

### 6.6.4 Final Filter Topology and Frequency Response

With both filters designed and simulated, the final filter can be constructed as seen in figure 6.14. The opamp in the circuit and simulations is not an ideal opamp, but rather an approximate model for the TI084, using its gain-bandwidth characteristics.

## 6.6. Design of Analog Filters

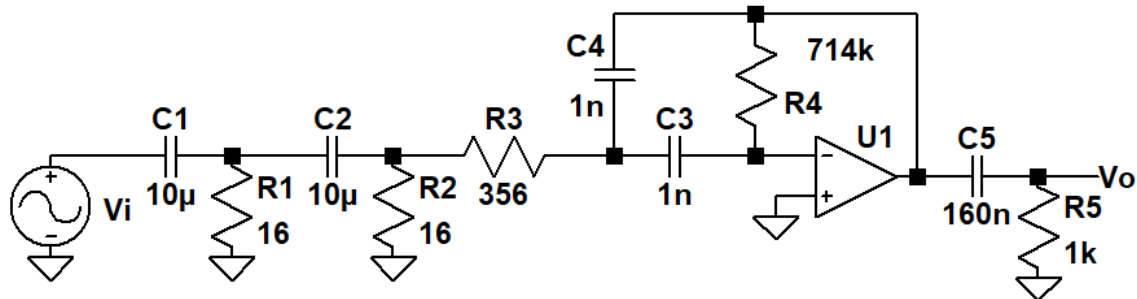


Figure 6.14: Circuit of the final filter.

This filter is simulated and results in the frequency response seen in figure 6.15. Additionally, the filter has been tested and the results of these tests can be found in appendix E and F. These tests were done after the PCBs were all put together, and as a result, the individual test did not yield much useful data, as the frequency response shows that there is a problem with channel D at the high pass filter. But since the full analog system works, it is concluded that the filters work satisfactorily. The reason a separate test is not conducted again is due to time constraints.

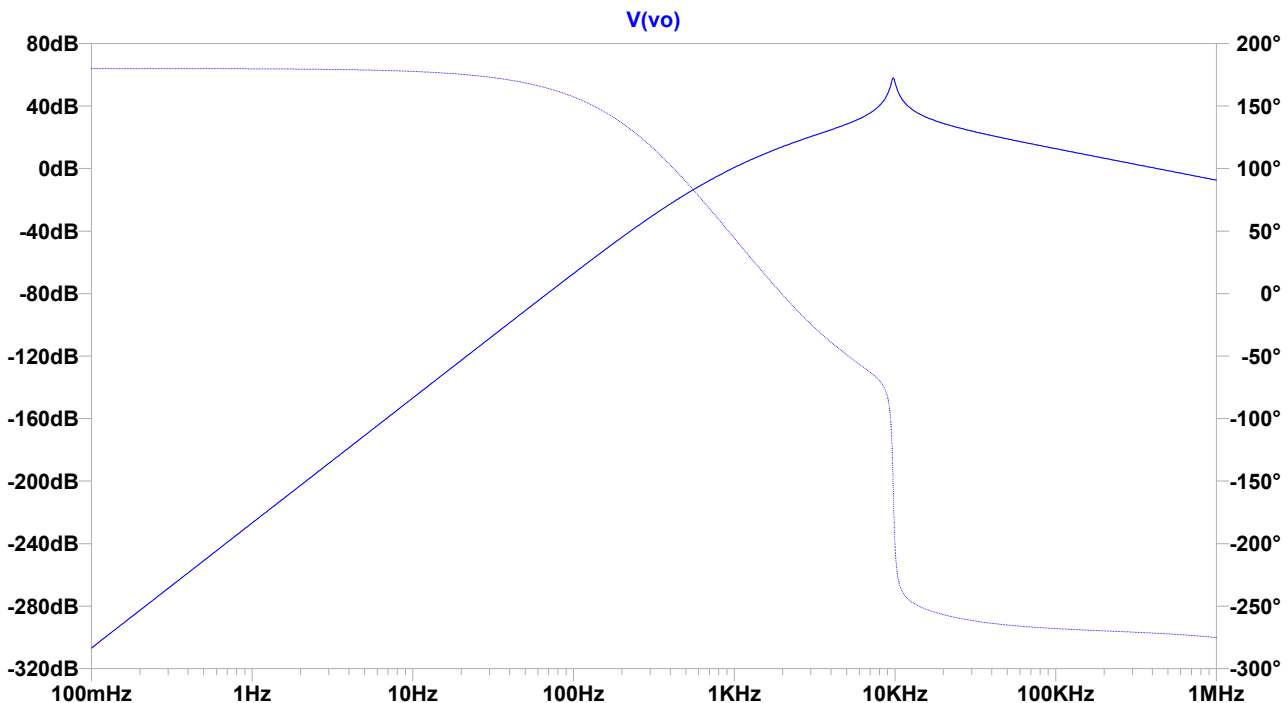
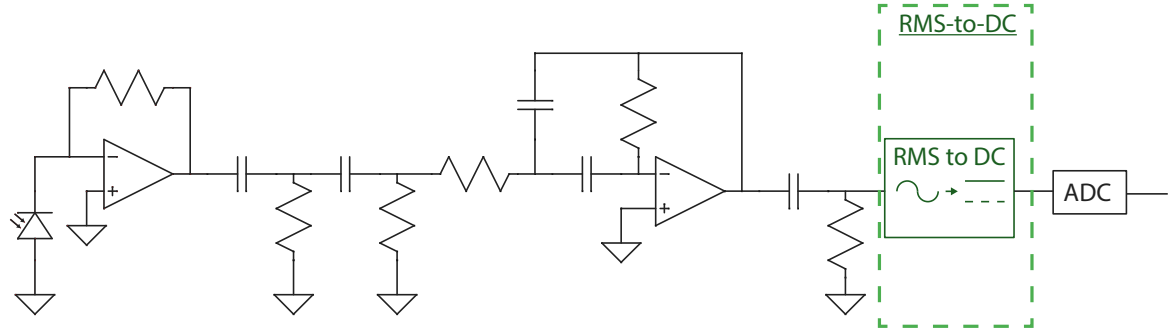


Figure 6.15: Simulation of the final filter circuit.

## 6.7 RMS-to-DC conversion



**Figure 6.16:** Full circuit diagram of the analog system, focusing on the RMS to DC converter.

The signal from the photodiode through the filters is a 10 kHz signal. To use the signal its magnitude is needed. It requires significant processing time and sampling rate to calculate the magnitude of a 10 kHz signal. So to greatly reduce the load on the MCU, an RMS-to-DC IC has been used to get a dc signal proportional to the amplitude of the filtered signal.

The RMS-to-DC converter used in the circuit is the AD736 [32], this is used because of its low bias current and the high accuracy. On figure 6.17 a block diagram of the circuit's functions can be seen.

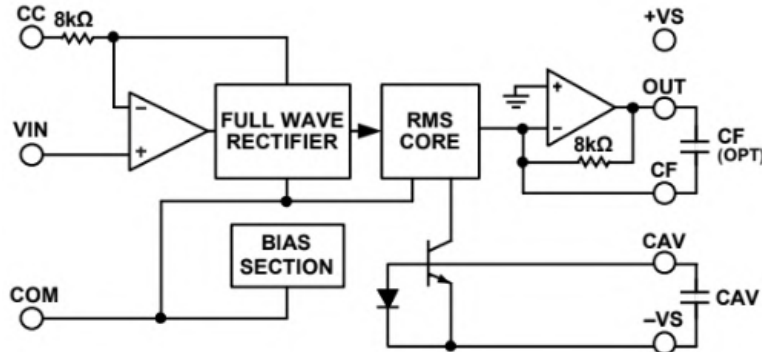


**Figure 6.17:** Function block diagram of AD736 RMS-to-DC converter [32].

## 6.8 Analog to Digital Conversion of Photodiode Signal

In order to use the photodiode signal as an error signal for the digital controller, the signal must be converted to a digital format. To do so an Analog to Digital Converter (ADC) is used, see figure 6.18. The digital data is to be processed by the PSoC microcontroller, which has a built in ADC block. This block is not used because four channels are needed, which would require multiplexing of the input signals, thus furthering complexity.

Instead an ADC IC is used. The ADC used is an ADS1174 [33], which features four 16-bit ADC channels. The 16-bit resolution gives 65536 steps, which results in 94  $\mu$ V steps when taking the ENOB from section 6.4 into consideration. In addition to these features, the IC also uses the SPI protocol for data transfer, which is already used for other sensors in the projectile. This means that

## 6.8. Analog to Digital Conversion of Photodiode Signal

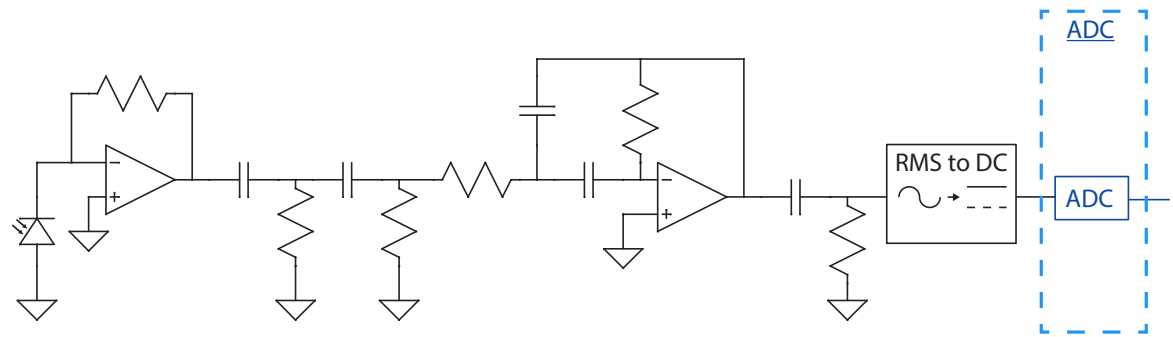


**Figure 6.18:** Illustration of the full analog circuit, focusing on the ADC.

the IC is simpler to implement into the existing system.

# Chapter 7

## Auxiliary Circuits

### 7.1 Power Supplies and Voltage Regulators

To power the electronics inside the projectile three different power supplies are needed. A supply for the microcontrollers and photodiode circuit, a negative supply for the op-amps in the photodiode circuit and a supply for the servo motors and LED's. As the supplies needs to be located inside the projectile both the form factor in terms of size and the weight are essential design parameters. Initially button cell batteries were considered, but the current requirements exceeded the supply of the cells.

To power the micro controllers and photodiode circuit a 9 V battery is used. For the negative supply for the op-amps another identical 9 V battery is chosen. The  $-9\text{ V}$  supply is obtained by connecting the plus terminal to the ground of the 9 V battery, and then the negative supply is obtained at the minus terminal of the battery. Both of the 9 V supplies are regulated down to  $\pm 9\text{ V}$ . Additionally, the 9 V supply is also regulated down to 5 V and 3.3 V. To supply the servo motors and LED's three AAA batteries in series which have voltage of 4.5 V are used.

### 7.2 LED's on the Projectile

To enable a visualization of the projectile's path in the air four coloured LED's are placed in each room separator of the projectile. The LED's are used for long exposure photos allowing for a visual documentation of the projectile's orientation. In the bottom room separator four RGB LED's are placed so it is possible to have four different colours in 90 degrees spacing. By having four different colours it is possible to see if the projectile rolls around itself in the air. In the top room separator four identical LED's are placed these are used to see if the projectile's orientation changes mid-flight.

### 7.3 Optocoupler

In order to reduce the amount of noise from the stepper motors, an optocoupler is used. The noise comes from the motors drawing up to 2 A of current, while also having a large inductance.

The optocoupler is placed between the microcontroller and stepper motors, thus galvanically isolating the control circuit. The optocoupler used is an ILQ1 [34], which has four isolated channels and is ideal since four stepper motors are used. The downside of this optocoupler IC, is that it requires a larger

### 7.3. Optocoupler

input current that the PSoC can provide. In order to alleviate this a transistor is used as a switch. The optocoupler circuit for one channel can be seen in figure 7.1.

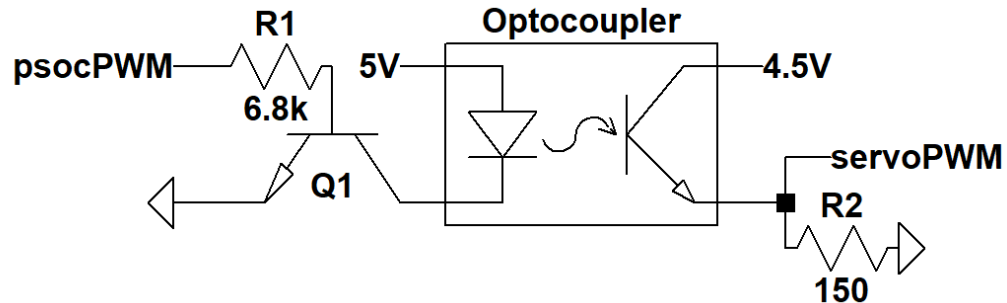


**Figure 7.1:** Circuit diagram of optocoupler circuit.

# Chapter 8

## Embedded Design

This chapter describes the design and functionality of the embedded firmware. These subsystems include the highlighted parts of figure 8.1.

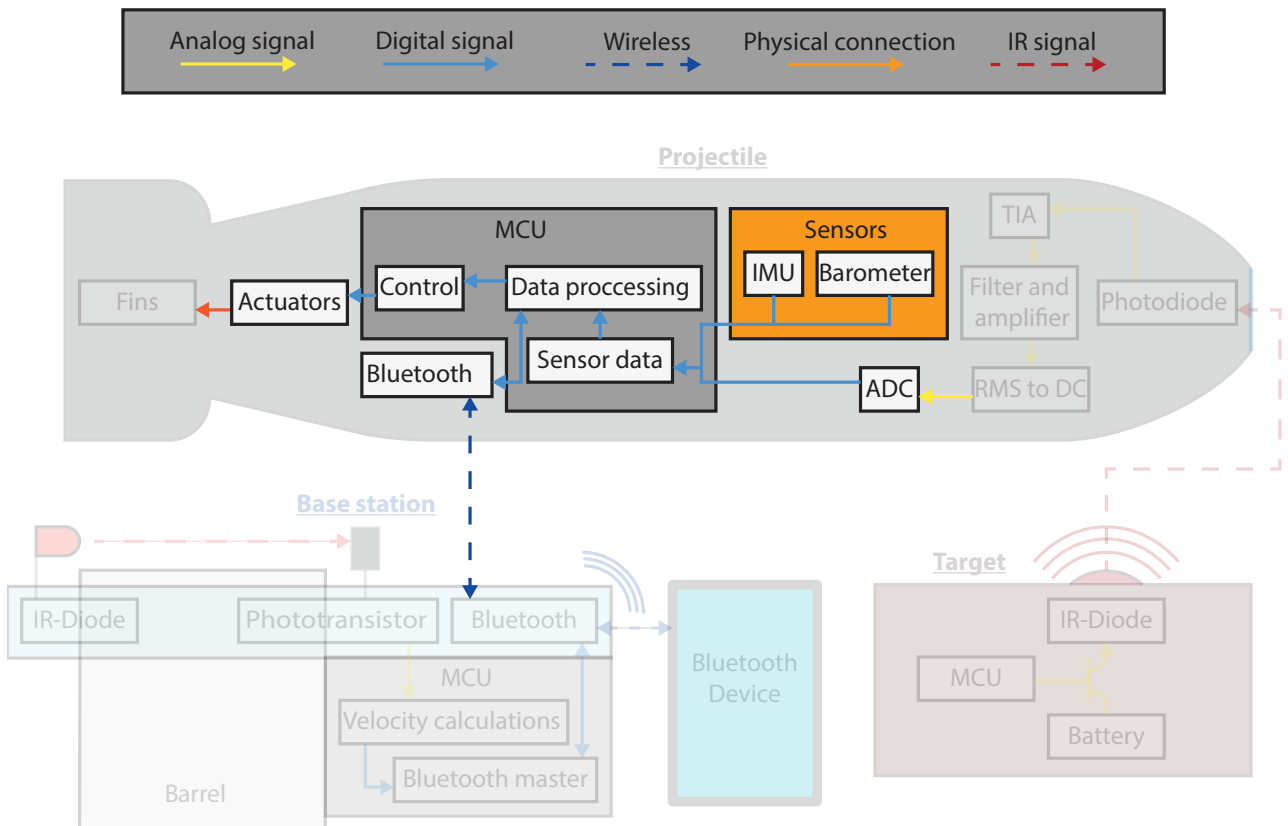


**Figure 8.1:** Illustration of the embedded design as part of the total system.

First the choice of programming paradigm is justified. In the following, it is explained how efficient peripheral communication is set up and performed in the PSOC ecosystem. Then, a complete list of runtime tasks is presented and their interaction with each other is described. Finally, it is explained how logged data is processed externally from the projectile.

## 8.1 Choice of Programming Paradigm

Since the embedded firmware, which runs on the PSOC in the projectile, includes multiple concurrent time sensitive tasks, it was decided to write the code on top of a real time operating system (RTOS). This in contrast to a 'bare metal' application, which would run directly on the hardware and thus the programmers are responsible for ensuring that all computations occur in the expected manner. For the RTOS, a FreeRtos implementation compatible with the PSOC 5LP was chosen [35]. All code is written in C as it is the only programming language that the PSOC IDE natively supports.

## 8.2 Peripheral Communication

As mentioned in chapter 3, a total of five peripherals are connected to the PSOC. The IMU and barometer are connected to their own separate SPI module within the PSOC. Likewise, the quad ADC has its own dedicated SPI module. These peripherals are connected to different SPI channels as the SPI implementation on the ADC was discovered to be incompatible with that of the other two sensors. The UART block is connected to the HC-05 Bluetooth module as well as the openLog component. Figure 8.2 shows how the internal hardware blocks are set up within the PSOC to facilitate efficient communication with the peripherals using DMA.

Starting with the SPIM block, it is the SPI Master for the BMP280 and MPU9250. The blocks MISO, MOSI, and SCLK pins are connected to its peripheral counterparts. The Slave Select (SS) pin feeds into a demultiplexer, which selects which device is to be selected. The demultiplexer is controlled by the current value in the SPI\_Control\_Reg. This value can be changed in the Firmware. Additionally, the SPIM modules RX and TX interrupt pins are connected to internal DMA blocks. Each block represents one DMA channel and each component is chained through a demultiplexer to their own respective RX and TX DMA channel. The purpose of the TX DMA channels is to, when requested by the firmware, transfer the read requests for the desired registers to the TX FIFO buffer of the SPIM, which will subsequently transfer them to the selected peripheral. The TX interrupt is set high whenever the internal FIFO buffer of the SPIM module is not full, thereby triggering the DMA channel to continuously keep the FIFO buffer full of read requests. The DMA channel continues to transfer data to the TX buffer until all read requests of interest are placed in the buffer. Similarly, the RX DMA channels are used to transfer data from the SPIM module's RX buffer to a pre-selected location in memory. Here, the RX interrupt signals triggers whenever the RX buffer is not empty, thus prompting the DMA to always move received data to memory. Like the TX DMA, the RX DMA stops transferring data when it has received all the requested data. The exact number of bytes this encapsulates differs between the two sensors and is set when configuring the DMA. As an example, to receive all sensor data from the MPU9250, 22 bytes must be requested. Unlike the TX DMA block, the RX blocks are also connected to an interrupt request block (the blocks with the lightning bolt symbol). These interrupts are triggered when the DMA completes its data transfer, and essentially tells the firmware that new sensor data is available for processing.

The functionality of the SPI block used for communicating with the ADC, SPIM\_ADC is almost identical to that of the SPI used for the IMU and barometer. The biggest differences are the lack of demultiplexers as well as MOSI and SS pin connections. Since this module is only connected to one peripheral it does not need to use the same demultiplexing scheme as the other module. The missing pin connections can be explained by the fact that the ADS1174 does not have MOSI or SS pins. Note that while the ADS1174 does not have a MOSI connector it is still necessary to use a TX DMA channel, as the SPIM\_ADC needs to have data in its TX buffer to activate its serial clock and receive data. There are no requirements as to which bytes are moved to the TX buffer using the TX

## 8.2. Peripheral Communication

DMA channel, it is only necessary that the amount of bytes moved match the amount of bytes its desired to receive.

Finally, the UART block is also connected to a DMA block. This allows for easy transfer of bulk data (such as logged sensor data) to the UART peripherals. Furthermore, the UART block's RX interrupt port is connected to an interrupt request which is used by the firmware to process incoming Bluetooth commands.

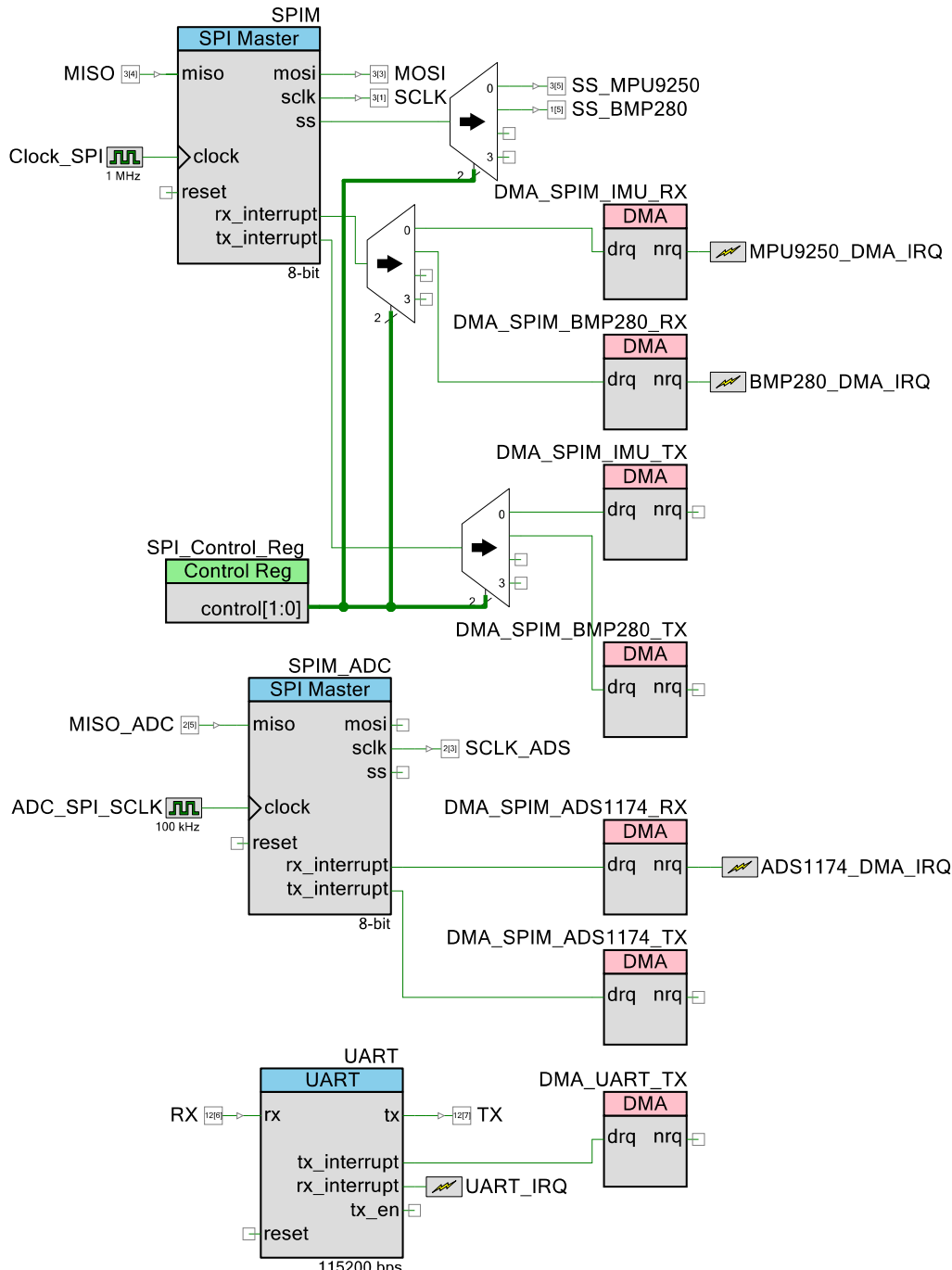


Figure 8.2: Block diagram of the PSOC Peripheal connections.

## 8.3 Tasks and Interrupt Service Routines

Several tasks and interrupt service routine are created within the FreeRtos ecosystem. The overall purpose of these tasks/ISRs is to facilitate the execution of the main control task by receiving and processing the sensor data required for effective control. To perform this in a computationally efficient manner tasks are only run when needed to. When not active, tasks are in a blocked state where they do not consume processing power. Task are unblocked and allowed to resume execution through periodic timing events or by receiving a notification event from another task or ISR. Additionally, it is critical that interrupts are kept as short as possible to minimise their interference with the otherwise executing task. This is done by deferring work to a task (by sending a notification event) tailored for the specific interrupt request. To gain further insight into the firmware tasks and their functionality, following is a list of subsections describing these. Subsection titles ending with "ISR" indicate that an interrupt service routine is described, while titles ending with "Task" indicate a task description.

### 8.3.1 SPIM Queue Management - Task

To avoid data request collisions between the IMU and the barometer an SPI transaction queue is created. The SPIM Queue Management task is notified every time a transaction is added to the SPIM queue, or if a SPIM becomes available to transfer new data (i.e. if DMA transaction for the IMU or barometer completes). If a transaction request is present in the queue, it dequeues the head and enables the corresponding DMA channel.

### 8.3.2 Data Available - ISR

Both the MPU9250 IMU and the ADS1174 ADC have physical data ready pins, which are activated when data is ready to be transferred from the peripheral to the PSOC. When the pin is activated for the IMU, an ISR queues a DMA transaction event for the IMU in the SPI queue. Before exiting, the ISR notifies the SPIM Queue Manager Management. This task immediately executes the transaction if no other transactions are present in the queue. Since the ADC has its own separate SPI channel, its data ready ISR does not need to queue DMA events and instead executes it immediately. Additionally, the UART channel also triggers an ISR whenever data is received. This ISR moves the data to memory and notifies the UART command management task upon receival of the end of command byte (in this case chosen to be 0xDE).

### 8.3.3 DMA Complete - ISR

When a DMA transaction to either of the three sensors completes, their own unique ISR is called. These ISRs notify each sensors respective data conversion task.

### 8.3.4 Get Barometer Data - Task

Unlike the IMU and ADC, the BMP280 barometer has no data ready pin which, DMA requests can be tethered to. To overcome this a task is designated to periodically run and queue a DMA transaction. To ensure that new data is available this period must be less than or equal to the barometers sampling rate. Since altitude measurements are not considered mission critical this period is arbitrarily set to 100 ms.

### 8.3. Tasks and Interrupt Service Routines

#### 8.3.5 Convert Sensor Data - Task

For each of the three sensors a data converter task exists. These tasks take the raw sensor data placed in memory by a DMA channel and converts the data to a floating-point representation.

#### 8.3.6 Calculate Quaternion - Task

To know the projectiles instantaneous orientation in space a quaternion must continuously be calculated. Quaternions provide mathematical notation to express and calculate orientation and rotation in a computationally efficient manner compared to other orientation representations. To calculate the orientation quaternion, it is not sufficient to simply use the information from one sensor, such as a gyroscope, as error and drift in the sensor data quickly renders the calculated orientation unusable. Instead data from the IMU's accelerometer, gyroscope, and magnetometer are combined in a process of sensor fusion to achieve a high degree of orientation accuracy. For this purpose, a computationally efficient orientation algorithm by Sebastian Madgwick [36] is applied. The C implementation of the algorithm is derived from work by Kris Winer [37]. Additionally, this implementation features an algorithm to filter the gravity component from the IMUs acceleration measurements. The details of the inner workings of these algorithms are out of scope and are not covered in this report. One important detail of the Madwick algorithm is that it is iterative and that it asymptotically converges to the correct orientation the more times it is run for a given set of data. For this reason, this is the default task to run when no other tasks are running (i.e. it has the lowest priority). Thus, ensuring that useful work is always performed in the CPU even when no critical task is being executed

#### 8.3.7 Main Control Loop - Task

The main control loop is the most important task in the firmware and is thus assigned the highest priority to ensure that it always runs at the intended interval. The control task uses the data from the sensors to calculate a new angle for the servo motors. Further details regarding the implementation of this task can be found in chapter 9.

#### 8.3.8 UART Command Management - Task

When the UART's data available ISR receives an end of command byte, the UART Command Management task is notified. The task is responsible for interpreting and responding to the received command. For example, in case of receiving a velocity from the base station, the CRC32 of the velocity value is calculated and compared to the received CRC32 value. If they match the velocity value is stored for later use and if they do not match a default velocity value is chosen. This fall back value is embedded in the firmware and is based on muzzle velocities measured during previous launches.

#### 8.3.9 Calculate Velocity - Task

The calculate velocity task remains idle until it receives a muzzle velocity value from the communication task. Upon reception of this values, it begins to periodically integrate the calculated linear acceleration and add it to the received muzzle velocity. Due to sensor inaccuracies this is not a valid long-term approach for velocity estimation. However, since a single launch only lasts approximately

## 8.4. PWM Motor Control

ten seconds, it is assumed that this method provides reasonable velocity measurements for the purpose of control.

### 8.3.10 Data logging - Task

To log the measured and calculated data points a task is designated to periodically convert all data to an ASCII representation and send this to the UART using DMA. To maximise performance all data points are converted to their raw hexadecimal representation as opposed to their base 10 decimal representation. This conversion is achieved by iterating over look up table converting a byte at a time to its ASCII representation. For example, the IEEE 754 single precision floating point hexadecimal representation of the value "9.81" is "0x411CF5C3" [38]. This can be split up into four separate bytes: "0x41", "0x1C", "0xF5", "0xC3". Using a look up table with 256 entries each of these bytes can then be converted to their respective two-character string. These strings are finally concatenated to produce the final ASCII representation. Not only is this computationally faster than converting the floating point values to a decimal representation, it also ensure that no precision is lost during the transmission as the true floating-point value is transmitted. The logged data is stored in the comma separated value format, where each data point is separated by the comma character (',') and the new line character ('\n') signifies that all desired data points have been logged.

## 8.4 PWM Motor Control

To control the servos, a PWM signal is needed. The servos are set based on the length of the PWM pulses. To set the servos to the centre position a pulse length of 1.5 ms is needed. To adjust the servo to either side a longer or shorter pulse is needed. Thus, the pulse length to adjust the servo is usually between 1 ms to 2 ms. However, this can vary a lot between servos, and has to be taken into consideration. It is recommended that the servos receive a pulse about once every 20 ms at most. Based on this, code has been designed to tune and control the servos. To adjust the servos for offset errors it is possible to set an offset for each individual servo. The servos can then be set to the desired rotation. To further simplify control of the servos functions has been made to control the 2 axes and the rotation separately.

## 8.5 Post Processing

For viewing and processing live or logged data a python application has been written. The application either accepts data from live serial stream or from a file stream. Data is converted from its ASCII floating point representation to true floating point and plotted as line graphs with a scrolling x-axis (time axis) where new data enters from the right and old data exits the graphing view from the left. By default, the latest 100 data points are visible at a time, however this is configurable. If data is live streamed from the projectiles serial port it is possible to get a live view of all sensor readings. This is immensely useful for development and debugging of the firmware. If instead data is streamed from a file a logging period can be specified whereby data can be extracted at the same pace. If it is not desirable to view a live recreation of the logged data, it is also possible to plot all the data at once. Figure 8.3 shows a screen-shot of live serial data being plotted. Additionally, the application can display a live 3D model of the projectile and orient it according to the logged quaternions. This is useful for obtaining a more tangible understanding of the projectiles in flight movements. Figure 8.4 shows a screen-shot of this in action.

## 8.5. Post Processing

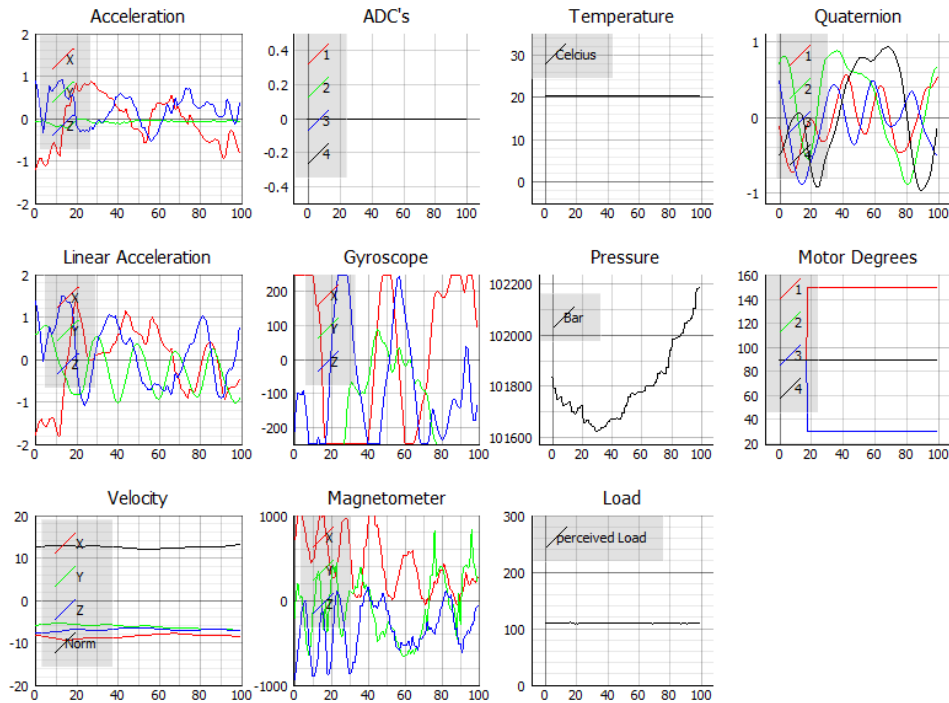


**Figure 8.3:** Screen-shot of live data plotting.

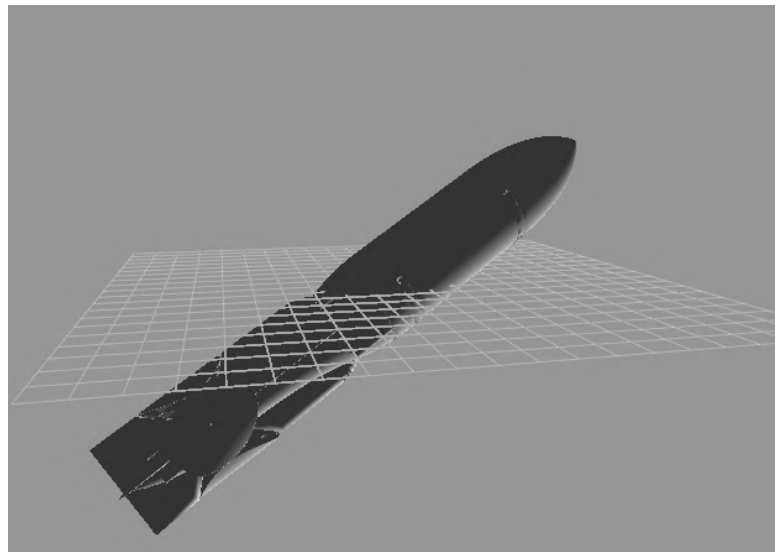


**Figure 8.4:** Screen-shot of orientation animation.

# Chapter 9

## Design of Controller

This chapter describes the design procedures of the controller for the system. First models of the projectile and the disturbances that influence it during flight are investigated. Followed by this are some thoughts and considerations about the design of a controller for the system.

### 9.1 Introduction

As stated in the problem statement, the projectile needs to be able to guide itself towards its target. This is achieved by using a controller to adjust the wings of the projectile and thus manoeuvring it in the air. In section 2.3 it was decided that the system relies on feedback, and thus a simple block diagram for the system can be created. This block diagram is seen in figure 9.1

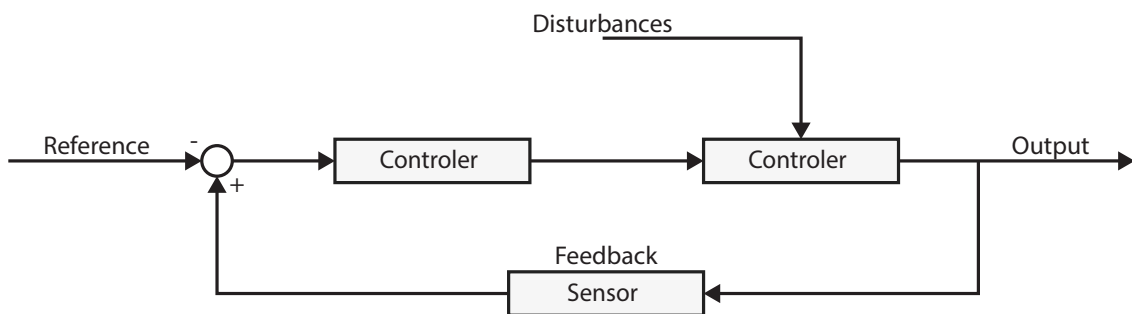


**Figure 9.1:** Simple block diagram showing the main modules of the control system.

The purpose of the controller is to regulate the behaviour of the projectile such that its output matches a set reference. In order to design the controller, it is necessary to create models of both the projectile (the plant) and the disturbances acting upon the projectile. In the following sections both the projectile and the disturbances are investigated with the intention of creating model of them both.

## 9.2 The Projectile

In order to control the projectile, its behaviour to different inputs must be modelled. The behaviour of the projectile is governed by physical forces and relations acting upon it during the path of travel. The way the projectile interacts with its surroundings is through its four wings, which changes the forces acting on it depending on their position. In order to precisely describe the relation between the position of the wings and the response of the projectile, the aerodynamics of the projectile must be investigated thoroughly. As stated earlier the aerodynamics is a complex field of study and lies beyond the scope of the semester objectives, which is why a different approach is chosen. Instead of modelling based on the physical aspects of the projectile in the air, an approximation is made by comparing the projectile against another system with a better-known model. It is thus chosen to approximate the projectile with wings as behaving similarly to a boat in water with a rudder. This is chosen due to air being similar to water when comparing their fluids dynamic properties. However, in order to compare the two, some assumptions are made, namely that it is possible to model the projectile in two separate planes with the same model, and that the dynamics of the two planes are decoupled. The system is then described using transfer functions for boats proposed by K. Nomoto, namely the second-order Nomoto model, seen in equation (9.1) [39],[40].

$$\frac{r}{\delta} = \frac{K(1 + T_3 \cdot s)}{(1 + T_1 \cdot s)(1 + T_2 \cdot s)} \quad (9.1)$$

where  $r$  is the yaw rate of the boat,  $\delta$  is the rudder deflection angle and  $K, T_1, T_2$  and  $T_3$  are constants. The Nomoto models are only valid under the assumption that the boat moves with constant velocity, the propelling thrust is constant, and that the rudder angle is small [41]. Thus, it is assumed that similar transfer functions can be used to describe the behaviour of the projectile under the same conditions. Additionally, an extension to the models can be made to include the servo motors that controls the wings of the projectile. To model the servo motors, it is necessary to look at the model of a DC motor, as the servo motors are DC motor based. The transfer function of a DC motor can be written as:

$$\frac{\omega_l(s)}{V_a(s)} = \frac{K_s}{\tau \cdot s + 1} \quad (9.2)$$

where  $\omega_l$  is the DC motor load angular velocity response, and  $V_a$  is armature voltage input [42]. As the servo motor works very fast, the time constant  $\tau$  can be removed from the equation which means the transfer function of the servomotors can be written simply as a constant. Thus, to extend the model to include the servo motors, the constant,  $K$ , gets multiplied with another constant from the servo motors,  $K_s$ . The model describes now the relationship between servo motor command and yaw rate of the projectile. However, as the photodiodes determines the orientation of the projectile in relation to the target, the model should be further extended to describe the relationship between servo motor command and orientation,  $\Psi$ , of the projectile. As the yaw rate,  $r$ , is the time derivative of  $\Psi$ , the required transfer function can be obtained by adding an integrator  $\frac{1}{s}$  to the transfer function. Thus, the final transfer function can be written as:

$$\frac{\Psi}{\delta_{\text{servo}}} = \frac{K_s \cdot K(1 + T_3 \cdot s)}{s \cdot (1 + T_1 \cdot s)(1 + T_2 \cdot s)} \quad (9.3)$$

In order to determine the constants usually a series of manoeuvring tests are made, tests which turns out not to be feasible to perform with the projectile. Therefore, a different approach is chosen, however it is still assumed that the behaviour can modelled by a first or second order transfer function. Furthermore, it is assumed that the transfer functions varies with the velocity of the projectile, as the aerodynamic forces depends on the square of the velocity.

### 9.3. The Disturbances

To investigate the dynamics of the projectile while it is in-flight, some initial test launches were made. All sensor values are logged during flight, to be processed afterwards. The results from the tests shows that during regular non-controlled flight, the projectile is unable to exhibit reliable open loop stability, but instead marginally stable behaviour. However, during some of the tests, the projectile seemed to be quite stable, with some rotation along its x-axis, as can be seen on the rotation graph on figure 9.2.

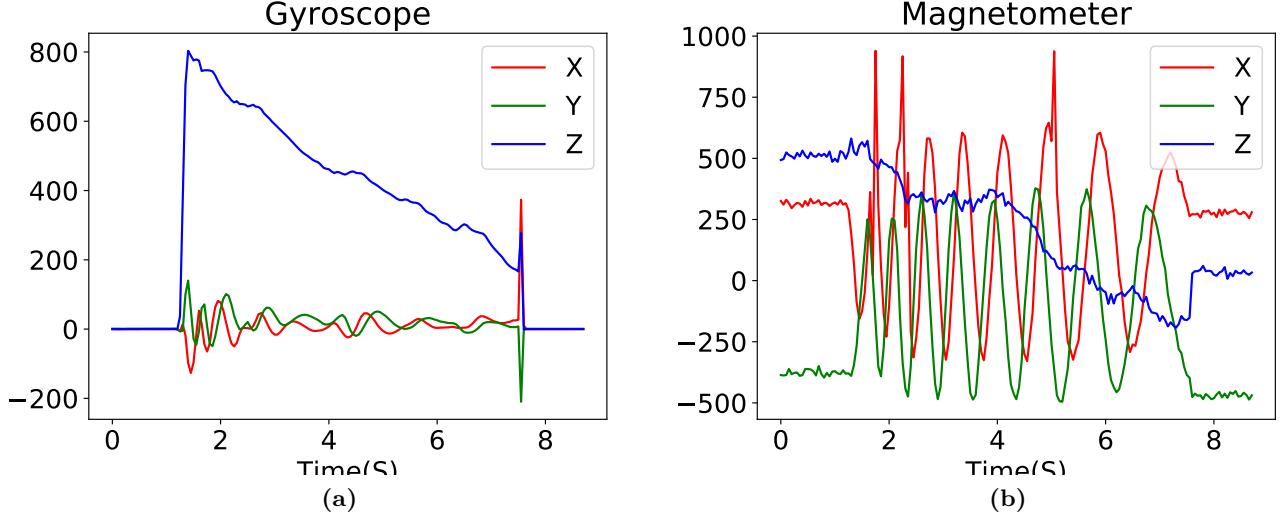


**Figure 9.2:** Measured raw data from an initial test launch showing readings from the gyroscope and magnetometer.

From the gyroscope data it can be concluded the projectile rotated around the x-axis during flight, as there is a positive angular velocity during the entire flight. Additionally, the magnetometer data shows two sinusoidal waves with increasing period, which corresponds to the decreasing angular velocity. The number of rotations can be determined by counting the wave tops in the magnetometer data.

Unfortunately, it has not been possible to reliably recreate these results. If the projectile had behaved identically each time, it would have been possible to implement an anti-rotation controller based on a rotational step response. The rotational step can be created because the angular acceleration is mostly linear, as seen on the linear measurement from the gyroscope. The anti-rotation controller is necessary because it is impossible to make reliable measurements of a directional step while the projectile rotates. With a non-rotating projectile, a directional step response could be determined experimentally and then used to calculate a transfer function.

## 9.3 The Disturbances

Upon launch during the flight trajectory, the projectile is influenced by aerodynamic forces as well as the weather i.e the wind but also slack between the wings and the servo motors. The controller needs to be able to counter these disturbances to some degree in order to route the projectile towards the target. Thus, some knowledge of the disturbances and their characteristics are desirable. The disturbances from aerodynamic forces due to imperfections along the projectile body can be somewhat modelled by tests in a wind tunnel, where the projectile is isolated from other disturbances. However, to perform such tests a much deeper understanding of aerodynamics is necessary, both in the design and the

#### 9.4. Thoughts About Controller Design

verification. This activity is outside the scope of the activities covered in the project and as such also excluded in the report. Therefore, no further investigation into these is made. The weather is very hard to model as well, as gusts of wind are almost unpredictable and therefore no further investigations are made here either. Lastly there is the slack between the wings and the servo. This could be modelled with potentiometers coupled with the ball bearings that hold the wings. Thereby the exact position of the wings can be measured and fed back to the servos. However, this measure never got implemented due to time restraints.

## 9.4 Thoughts About Controller Design

As stated earlier it is not possible to determine transfer functions for the projectile, due to instabilities during flight. Thus, it is not possible to implement a controller in the system, as there is no model to test it with. However, a lot of considerations has gone into how the controller would be implemented and which requirements it should fulfil, based on both observed and assumed behaviour of the projectile. Even the design process itself has been investigated. In the following, these thoughts and considerations is described.

Firstly, in order to structure the design process of the controller, the process is divided into several steps. These steps can be seen in the list below which is inspired by a list from “MULTIVARIABLE FEEDBACK CONTROL: Analysis and Design” [43].

### Steps in controller design:

1. Study the system (plant) to be controlled and obtain initial information about the control objectives.
2. Model the system and simplify the model, if necessary.
3. Analyse the resulting model; determine its properties.
4. Decide which variable are to be controlled (controlled outputs).
5. Decide on the measurements and manipulated variables: what sensors and actuators will be used and where will they be placed?
6. Decide the type of the controller to be used.
7. Decide on performance specifications, based on the overall control objectives.
8. Design a controller.
9. Analyse the resulting controlled system to see if the specifications are satisfied: and if they are not satisfied, modify the specifications or the type of controller.
10. Simulate the resulting controlled system, either on a computer or a pilot plant.
11. Repeat from step 2, if necessary.
12. Choose hardware and software and implement the controller.
13. Test and validate the control system, and tune the controller on-line, if necessary.

#### 9.4. Thoughts About Controller Design

As stated earlier the system to be controlled is the projectile. The objective of the controller is to enable the projectile to handle disturbances acting upon it during flight and thereby hit its target with higher accuracy i.e. decrease its CEP as stated in the problem statement. Based on some assumptions it is expected that it is possible to model the projectile with a second-order transfer function, however it is not possible to conduct tests to verify this. From the observed behaviour of the projectile during flight it is assumed that two controllers are needed. One to control the rotation of the projectile around its x-axis and one to control its orientation.

The controlled variables in the system are the orientation of the projectile and the angular velocity around the x-axis, both of which is changed by changing the angle of the four wings on the projectile. The measurement of the orientation is based on the set of photodiodes in the nose of the projectile, which based on incoming light through the pin hole, determines the direction of the target in relation to the projectile's current orientation. To measure the angular velocity, the onboard gyroscope is used. The reference orientation that the orientation controller must maintain is the orientation that keeps the target directly in front of the projectile. The rotation controller needs to be able to initially increase the rotation of the projectile to keep it stable as it rises towards the vertex of its flight parabola and then stop the rotation as the projectile descends towards the target to enable the directional controller to change the orientation of the projectile. To influence the projectile both controllers can send a PWM signal to the servo motors connected to the wings and change the position of them.

Without transfer functions with realistic values a specific type of controller cannot be chosen, as the properties of the real system is unknown. However, based on desired system behaviour some performance requirements can be defined. Ideally the projectile should have no rotation around the z-axis during flight, and start changing its orientation towards the target a short time after it reaches the vertex. This is because the part of the flight path from the vertex to the target is mostly linear. For the orientation controller to work, the projectile needs to be able to detect the target, thus the nose of the projectile has to point downwards. Tests would need to be made to determine the exact time the projectile is oriented such that the target is detected, but most likely this happens some small interval after the vertex has been reached, approximately after half the flight time. This gives a time restraint for the settle time of the rotation controller. Likewise, the time restraint for the settle time of the orientation controller is the remaining time of the flight duration. The initial reference tests showed that the average flight time of the projectile is 7s, and thus the settle time of the orientation controller needs to be less than 3.5s.

Another factor to consider is the velocity dependence of the transfer function of the projectile. If the transfer function is very sensitive to variations in the velocity of the projectile, a method called gain scheduling can be utilised to increase accuracy. Gain scheduling means that the controller uses different gains to calculate its output, based on a changing value in the system. To utilise this, the different transfer functions for the system must be determined, and appropriate gains for each must be calculated. Thus, if a set of different transfer functions exists for varying velocities, the projectiles velocity measurement can be used to give different gains to the controller depending on the velocity of the projectile. A block diagram presenting an incorporated gain scheduling block in the control system is seen on figure 9.3

#### 9.4. Thoughts About Controller Design

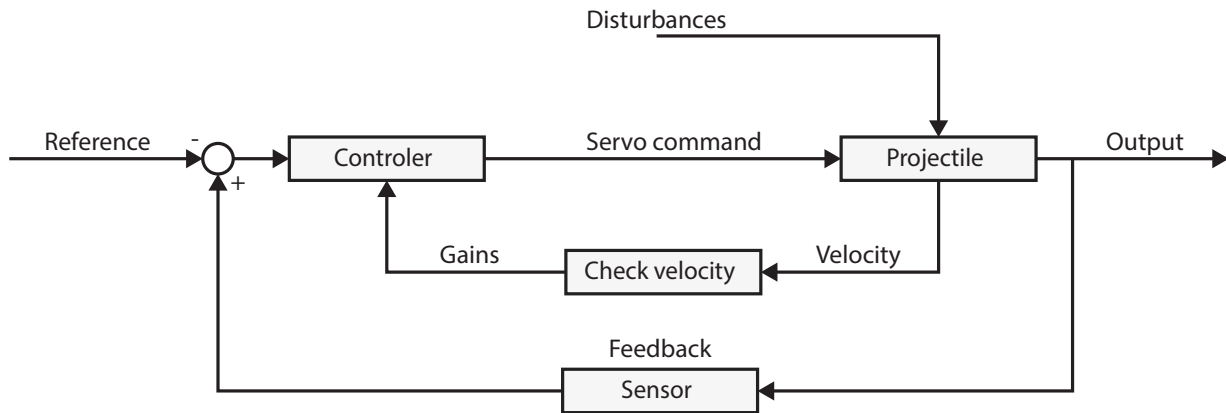


**Figure 9.3:** Simple block diagram showing the main modules of the control system with a block for gain scheduling.

Lastly, when implementing the controller care should be taken that the gain applied does not put the servos into saturation. At some point increasing the angle of the wings further will cause stalling instead of increasing the angular velocity.

The next step would be to design the specific controller, however as no specific type of controller has been identified this is not possible. Thus, the controller design process cannot go further.

# Chapter 10

## Implementation

With all subsystems designed they are to be implemented into the final product. The first subsystems to be implemented are the analog circuits. Following this, the circuits are placed in the projectile together with the digital systems and motors. Finally, the projectile is assembled, resulting in a finished prototype ready for testing.

### 10.1 Implementation of Analog Circuits

The analog circuits consists of the photodiode and its amplifiers and filters. These were designed to be as small as possible in order to fit inside the projectile. This resulted in a very compact PCB design, using SMD components and ICs, which meant they proved difficult to troubleshoot. This became apparent when testing the four channels of the photodiode circuit, as one of the channels was non-functional. The reason for this turned out to be a faulty channel. The fault appears to occur at one of the highpass filters before the active band pass filter. To circumvent this, a modified version of equation 6.1 using only three channels is used:

$$\begin{aligned} X &= \frac{A - B}{A + B} \\ Y &= \frac{C - B}{C + B} \end{aligned} \tag{10.1}$$

Where A,B, and C represent the intensity of light on each of the three active photodiodes as shown in figure 10.1:

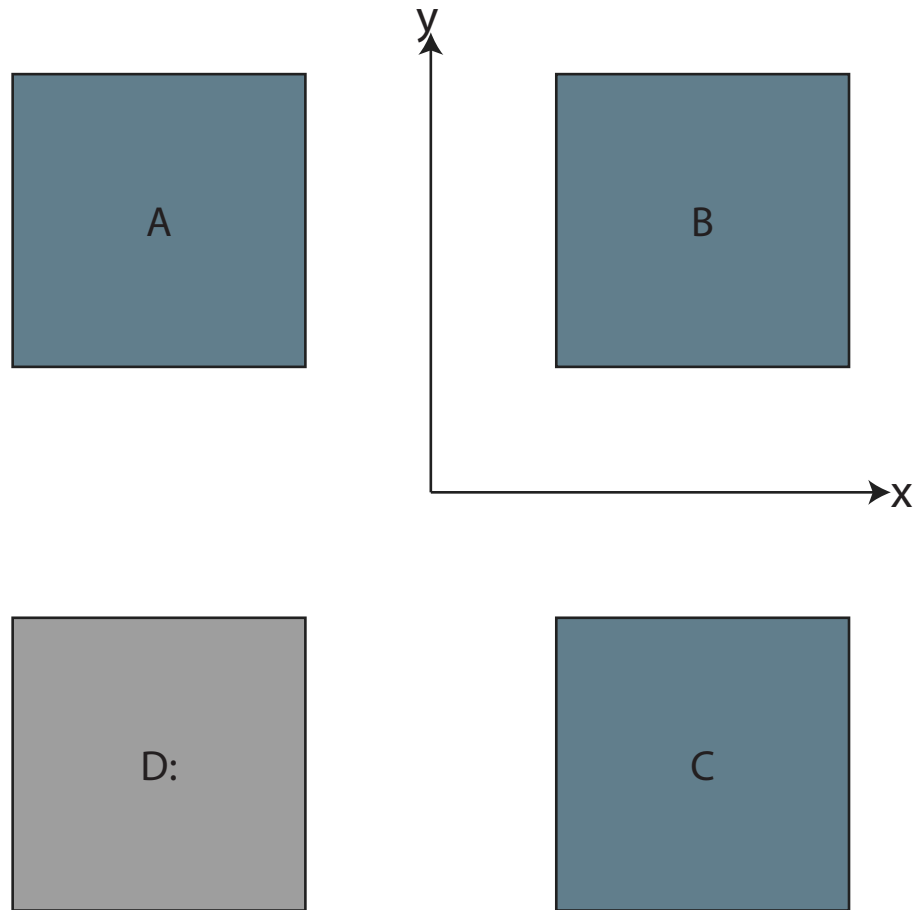


**Figure 10.1:** illustration of the quad photodiodes with the dead channel marked in grey.

While this is likely not as accurate as the full quad photodiode implementation, it provided a proof of concept of the functionality of the subsystem.

In addition to one channel not working, the RMS to DC converter exhibited some strange behaviour. Whenever the lights were turned off the circuit did not function, however with the lights on it worked as expected. This is the opposite behaviour of the photodiode circuit than from before the diode was pulse modulated, since the lights would drown out the diode. On top of this, the analog implementation resonates at a frequency of approximately 8 kHz when the lights are off. The reason for this is unknown.

The rest of the analog circuitry performed satisfactorily and as designed, excluding the ADC, which will be further explained in section 10.2.

## 10.2 Implementation of Digital Systems

There were no major issues with implementing the digital systems, however the interface between analog and digital did. This was due to the ADC IC not working after being soldered on the PCB. The ADC had worked fine when tested on its own, however due to having 64 pins and running out of the IC, it was chosen to use the internal ADCs in the PSoC. These ADCs are only 12-bit, meaning

### 10.3. Implementation of Projectile

a slight decrease in resolution from the previously used 16-bit ADC. Despite this, the functionality remains and as such no further troubleshooting is done on the ADC IC.

## 10.3 Implementation of Projectile

The projectile was assembled as seen on figure 10.2

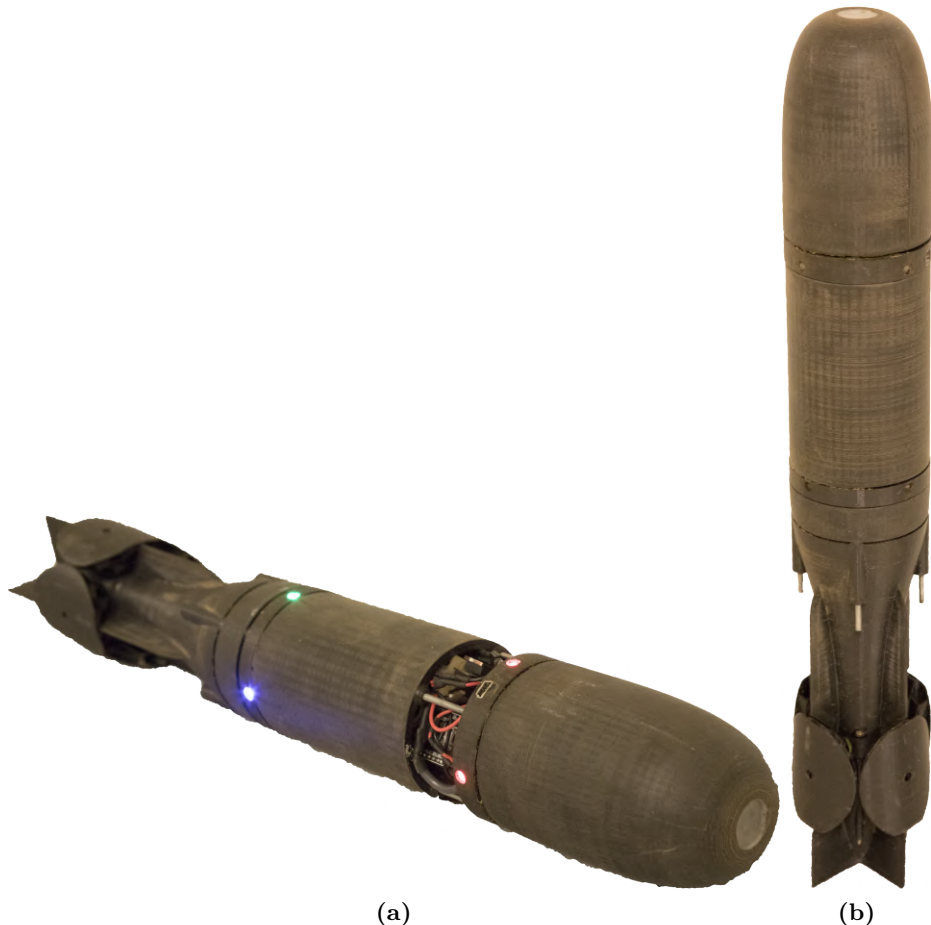


**Figure 10.2:** Pictures of implemented projectile

The implementation was a tight fit and was difficult to assemble, since a lot of electronics had to fit in a very tight space. all of the electronics and parts for are shown on figure 10.4.

#### 10.4. Implementations of Pinhole

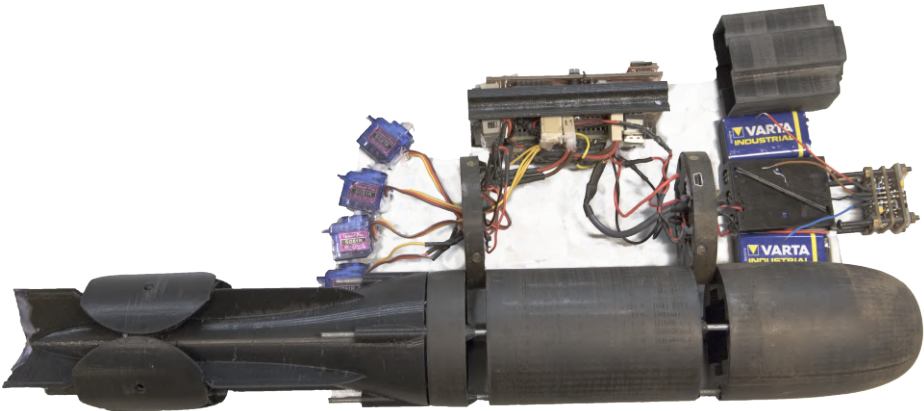


**Figure 10.3:** Exploded view of the implemented parts of the system.

Not only did the tight fit result in a long time to assemble but it was also at a scale where tolerances on 3D-prints and PCB was causing troubles and had to be adjusted by manual labour. Due to the tolerances there was also problems with gaps in the assembly and slack on the fins. Another major disadvantage of the design was the need to access the SD-card to get data from the test. Because of the time required to access the inner parts of the projectile, it was a very time-consuming task to get the data. A minor but time consuming problem with the design was the gaps in and around the buttons and connectors getting filled with dirt after each test, and thus had to be cleaned to be used. The main problem was the durability of tail since the projectile was not always stable in flight by the time it hit the ground and thus ended up breaking and therefore stopping the tests

## 10.4 Implementations of Pinhole

The implementation of the pinhole can be seen on figure 10.4

#### 10.4. Implementations of Pinhole

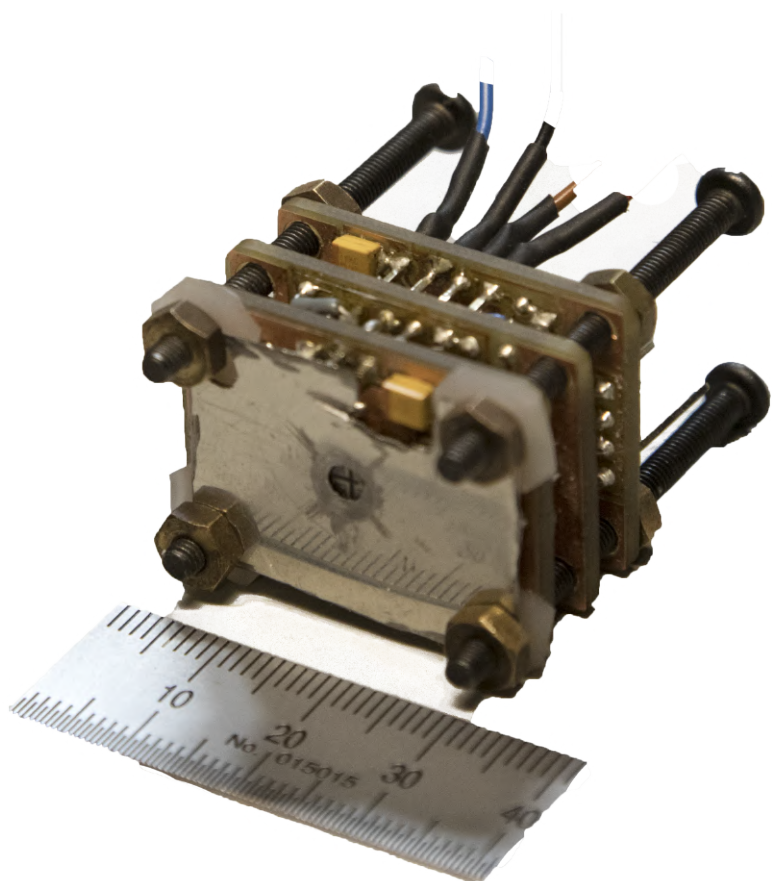


**Figure 10.4:** Picture of the implemented Pinhole and analog PCBs.

The Pinhole was implemented by slowly grinding through a metal plate until the hole had the desired size. To adjust the position of the pinhole the holes for the rods in the pinhole plate was designed with slack such that small adjustments could be made after the plate is fastened. To adjust the distance from the photodiodes the plate was mounted with silicone pads underneath and then tightened by nuts for the desired distance.

## **Part III**

# **Discussion and Conclusion**

# Chapter 11

## Discussion

To make this project possible, it was necessary to design a projectile, which could be controlled in the air. As this project was not a proposal that was given at the semester start, the project would need a lot of mechanical construction, in order to create the platforms i.e. launcher and the projectile. The research of these things consumed a lot of time. After using time on researching the construction of a launcher, the group was provided a launcher by the university, which could be used for the project.

The construction of the projectile has been an iterative process, where different shapes have been tested, to see which was most stable in the air. As mentioned in the design section of the projectile, the group have no experience with aerodynamics and the project's focus should be the control of a projectile and not the construction of it. Due to a lack of experience, the design of the projectile ended up taking longer than anticipated. This was compounded by the fact that construction and testing of each iteration was a multi-day endeavour. In addition to taking longer than expected, the projectile also turned out to not be open loop stable, especially at lower air-speeds. This prevented the creation of a model of the projectile, since an input-step analysis yielded little useful results. Ultimately this made it impossible to design a controller for the projectile, which instead had to be done theoretically. The projectile design, and lack of knowledge in this field, ended up hindering the development of the electronic systems.

Using the provided launcher resulted in some size constraints of the projectile. These size-constraints had to be considered in the design of the electrical systems, which proved to be a challenge. In previous projects, the physical size of the designed circuits was never an issue. Having to consider the physical footprint of PCBs, components and supply sources impacted the electrical designs more than first anticipated. While this increased the complexity of the design, it was seen as a great opportunity to consider an otherwise ignored aspect of electrical design.

Some of the subsystems were designed as a forethought, meaning they were designed and implemented before being needed. These subsystems ended up never being used, as the projectile and main focus of the project was not realised in time. As such, this time could have been better spent elsewhere.

# Chapter 12

## Conclusion

The purpose of this project is to gain insight into how analog and digital electronic systems can be combined to interact with the surrounding environment. In order to explore this wide reaching topic it was decided to investigate the development of guidance systems for projectiles.

To impose a more concrete objective, a goal of creating a control system which aims to reduce the CEP of a projectile is presented in chapter 1. To further guide the project, a set of initial design choices are made in chapter 2.

The development proved more challenging than initially anticipated, due to the need to develop an open loop stable physical projectile. The constructed design turned out to be open loop unstable and therefore it was not possible for to derive a transfer function on which a control system could be build upon.

However, tests of the direction detecting systems proved more successful. While, one of the photodiode channels was non functional, it was possible to partially solve this issue through software, and further tests were possible. These tests showed that the system was indeed able to detect the target IR diode and its direction up to a FOV of 90° as was specified.

In conclusion it has not been possible to determine if a guidance system based on optics and an IMU can be designed and be able to reduce the CEP of a projectile. However, based on tests of the direction detecting systems, it is assumed that such a system can in fact be designed with photodiodes and a negative feedback control system.

# Bibliography

- [1] N. C. Crawford, “Update on the human costs of war for afghanistan and pakistan, 2001 to mid-2016,” [https://watson.brown.edu/costsofwar/files/cow/imce/papers/2016/War%20in%20Afghanistan%20and%20Pakistan%20UPDATE\\_FINAL\\_corrected%20date.pdf](https://watson.brown.edu/costsofwar/files/cow/imce/papers/2016/War%20in%20Afghanistan%20and%20Pakistan%20UPDATE_FINAL_corrected%20date.pdf), 2016, 01-11-18.
- [2] J. Smith, “Afghan civilian casualties from air strikes rise more than 50 percent, says U.N.” <https://www.reuters.com/article/us-afghanistan-casualties/afghan-civilian-casualties-from-air-strikes-rise-more-than-50-percent-says-u-n-idUSKBN1CH1SZ>, 2017, 03-11-18.
- [3] Wikipedia, “Agm-114 hellfire,” [https://en.wikipedia.org/wiki/AGM-114\\_Hellfire](https://en.wikipedia.org/wiki/AGM-114_Hellfire).
- [4] ——, “Laser guidance,” [https://en.wikipedia.org/wiki/Laser\\_guidance](https://en.wikipedia.org/wiki/Laser_guidance).
- [5] Amalahama, “Blackshark and laser guidance,” <https://forums.eagle.ru/showthread.php?t=24710&page=2>, 2007.
- [6] A. Parsch, “Directory of U.S. military rockets and missiles - AGM-65,” <http://www.designation-systems.net/dusrm/m-65.html>.
- [7] Wikipedia, “Thermographic camera,” [https://en.wikipedia.org/wiki/Thermographic\\_camera](https://en.wikipedia.org/wiki/Thermographic_camera).
- [8] D. T. I. C. Mike Milner, “Precision strike association excalibur overview,” [https://web.archive.org/web/20150511200421/http://www.dtic.mil/ndia/2012annual\\_ps/Milner.pdf](https://web.archive.org/web/20150511200421/http://www.dtic.mil/ndia/2012annual_ps/Milner.pdf).
- [9] K. R. Newsom, “AFOTEC technical journal, volume 2, number 1.” <https://apps.dtic.mil/dtic/tr/fulltext/u2/a205489.pdf>.
- [10] “Defense industry daily Excalibur 155mm GPS shell lg,” [www.defenseindustrydaily.com/](http://www.defenseindustrydaily.com/).
- [11] DARPA, “EXACTO guided bullet demonstrates repeatable performance against moving targets,” [www.darpa.mil](http://www.darpa.mil).
- [12] ——, “Photo showing DARPA’s rendering of the EXACTO bullet.” [www.darpa.mil](http://www.darpa.mil).
- [13] sjumilitaryscience, “Photo showing the different trajectories of mortars and artillery,” [https://sjumilitaryscience.weebly.com/](http://sjumilitaryscience.weebly.com/).
- [14] “Cypress semiconductor CY8CKIT-059 development board,” <http://dk.farnell.com/cypress-semiconductor/cy8ckit-059/dev-board-psoc-5-prototyping/dp/2476010>, 2018.
- [15] Sparkfun. Sparkfun. [Online]. Available: <https://cdn.sparkfun.com/assets/part/1/1/3/0/6/13762-00a.jpg> [Accessed 15 Dec. 2018].
- [16] Adafruit. Adafruit. [Online]. Available: <https://cdn-shop.adafruit.com/1200x900/2651-00.jpg>

## Bibliography

- [17] *HC-05*. Aliexpress. [Online]. Available: <https://ae01.alicdn.com/kf/HTB16cZgXXXXXXXXLaXXXq6xXFXXX3/>  
HC-05-Wireless-Bluetooth-Host-Serial-Transceiver-Module-with-button-Slave-and-Master-RS232-For-Arduino-jpg\_640x640.jpg[Accessed15Dec.2018].
- [18] *Adafruit*. Adafruit. [Online]. Available: <https://cdn-shop.adafruit.com/1200x900/2201-03.jpg>
- [19] LED ENGIN, “LZ1-00R602 IR-LED datasheet,” <https://www.mouser.dk/datasheet/2/228/LZ1-00R602-368524.pdf>, 2018.
- [20] K. Giang, “PLA vs. ABS: What’s the difference?” <https://www.3dhubs.com/knowledge-base/pla-vs-abs-whats-difference>, 06-11-18.
- [21] NASA, “Rocket aerodynamics,” <https://spaceflightsystems.grc.nasa.gov/education/rocket/rktaero.html>, 06-11-18.
- [22] S. Munawar, “Analysis of grid fins as efficient control surface in comparison to conventional planar fins,” *27th Congress of the International Council of the Aeronautical Sciences 2010, ICAS 2010*, vol. 3, pp. 1732–1737, 01 2010.
- [23] [Online]. Available: [http://www.osiopoelectronics.com/application-notes/AN-Position-Sensing-Photodiodes\(PSDs\).pdf](http://www.osiopoelectronics.com/application-notes/AN-Position-Sensing-Photodiodes(PSDs).pdf)
- [24] W. Kester, “Understand sinad, enob, snr, thd, thd n, and sfdr so you don’t get lost in the noise floor,” Oct 2008.
- [25] G. Kopp and J. L. Lean, “A new, lower value of total solar irradiance: Evidence and climate significance,” *Geophysical Research Letters*, vol. 38, no. 1, 2011. [Online]. Available: <https://agupubs.onlinelibrary.wiley.com/doi/abs/10.1029/2010GL045777>
- [26] OSI Optoelectronics, “Photodiode characteristics and applications,” *OSI Optoelectronics Application Notes*, 2013, 16-12-2018.
- [27] J. G. Graeme, *Photodiode Amplifiers*. USA: McGraw-Hill, 1995.
- [28] Texas Instruments, “OPA2380 datasheet,” <http://www.ti.com/lit/ds/symlink/opa2380.pdf>, 2003.
- [29] TT Electronics, “OPR5925 datasheet,” [https://www.mouser.dk/datasheet/2/414/Datasheet\\_OPR5925-1131996.pdf](https://www.mouser.dk/datasheet/2/414/Datasheet_OPR5925-1131996.pdf), 2016.
- [30] K. Su, *Analog Filters*, 2nd ed. Kluwer Academic Publishers, 2002.
- [31] Texas Instruments, “TI084 datasheet,” <http://www.ti.com/lit/ds/symlink/tl084.pdf>, 2015.
- [32] Analog Devices, “Ad736 datasheet,” <https://www.analog.com/media/en/technical-documentation/data-sheets/ad736.pdf>, 2012.
- [33] Texas Instruments, “ADS1174 datasheet,” <http://www.ti.com/lit/ds/symlink/ads1174.pdf>, 2008.
- [34] Vishay, “ILQ1 datasheet,” <https://www.mouser.dk/datasheet/2/427/ild1-103056.pdf>, 2017.
- [35] btodoroff, “FreeRTOS CY8CKIT 059,” [https://github.com/btodoroff/FreeRTOS\\_CY8CKIT\\_059](https://github.com/btodoroff/FreeRTOS_CY8CKIT_059), 2017, 05-10-18.
- [36] S. Madgwick, *An efficient orientation filter for inertial and inertial/magnetic sensor arrays*, Apr 2010.
- [37] K. Winer, “MPU9250,” <https://github.com/kriswiner/MPU9250>, 2018, 15-10-18.

## Bibliography

- [38] The Institute of Electrical and Electronics Engineers, “IEEE standard for floating-point arithmetic,” *IEEE Std 754-2008*, pp. 1–70, 2008.
- [39] K. Nomoto, K. Taguchi, K. Honda, and S. Hirano, “On the steering qualities of ships,” *Journal of Zosen Kiokai*, vol. 1956, no. 99, pp. 75–82, 1956.
- [40] P. Mishra, S. K Panigrahi, S. Das, M. Engg Dept, and Milit, “Ships steering autopilot design by nomoto model,” *International Journal of Mechanical Engineering and Robotics (IJMER)*, vol. 3, pp. 2321–5747, 01 2015.
- [41] Z. Yu, X. BAO, and K. Nonami, “Course keeping control of an autonomous boat using low cost sensors,” *Journal of System Design and Dynamics*, vol. 2, pp. 389–400, 01 2008.
- [42] N. Y. University, “Experiment 3: Modelling, identification, and control of a dc-servomotor,” [http://engineering.nyu.edu/mechatronics/Mpcrl/Experiment\\_3\\_protected.pdf](http://engineering.nyu.edu/mechatronics/Mpcrl/Experiment_3_protected.pdf).
- [43] S. Skogestad and I. Postlethwaite, *Multivariable Feedback Control: Analysis and Design*. USA: John Wiley #38; Sons, Inc., 2005.
- [44] R. Mancini.

## Appendix A

# Determining the Size of the Pinhole

The design of the pinhole depends on three properties; shape, size and distance from the photodiodes. Each of these properties have some influence on the others, thus some choices have to be made before final values can be determined. A choice is made considering the size of the pinhole, based on measurement accuracies. Thus calculations of measurement accuracy and size of the pinhole is examined.

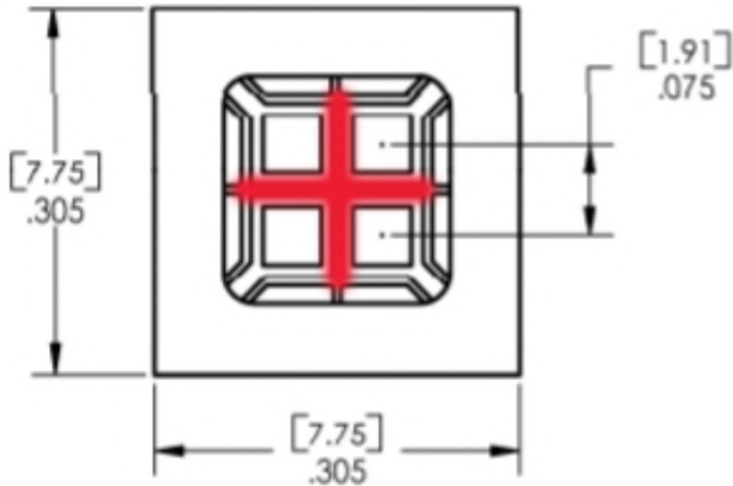


**Figure A.1:** Photodiodes seen from above. Deadzone marked with red [29].

On figure A.1 it is seen that there exists some space between each photodiode, where incoming light is not registered. This space is henceforth referred to as dead space. Additionally, there is some space from the outer edges of the photodiodes to the edges of the component as a whole. Henceforth, only the area comprised of the square that exactly covers all photodiodes is examined.

The size of the pinhole is chosen based on how much of each diode should be hit by the light beam, when the angle of incidence is 0 deg. This is the reference position, where the projectile is headed directly towards the target, and it is important to get reliable measurements for the controller in this position. Therefore the area should be several times larger than the smallest measurable area. To determine the smallest measurable area, the resolution of the photodiode measurements is examined. The resolution of the measurement is determined by the resolution of the ADC used in the projectile. The 16 bit ADC can measure a resolution of approximately 76  $\mu$ V with a full scale of 5 V. To convert

this voltage into an area, some intermediate calculations are needed. First, the voltage is used to calculate the expected current created by photodiode. From chapter 6.4 the gain from the photodiode to the ADC is given as 200 dB, thus the current from the photodiode can be found as

$$\begin{aligned} I_{min} &= \frac{V_{min}}{\text{Gain}} \\ &= \frac{76}{10^{10}} \\ &= 7.6 \text{ fA} \end{aligned} \quad (\text{A.1})$$

This current is a result of light hitting the photodiode and according to the datasheet of the photodiode the conversion rate between power and current is 0.45 A/W. Thus the minimum measurable power can be found as

$$\begin{aligned} P_{min} &= \frac{I_{min}}{0.45} \\ &= \frac{7.6 \cdot 10^{-15}}{0.45} \\ &\approx 17 \text{ fW} \end{aligned} \quad (\text{A.2})$$

How big an area this power corresponds to depends on the flux density of the light at the photodiode which itself depends on the distance between the light source and the photodiode. In section 6.4 it was stated that the projectile should be able to detect its target from a distance of 100 m and thus the flux density at that distance is used to calculate the smallest detectable area.

The IR-diode used as the target is assumed to emit light in a uniform half sphere. As stated in chapter ?? the diode emits 0.278 W, which is evenly distributed across the entire surface of the half sphere at any distance from the diode, as stated by Gauss's Law []. Thus the flux density at 100 m is  $E_e = 4.4 \frac{\mu\text{W}}{\text{m}^2}$ .

Now it is possible to calculate the minimal measurable area at a distance of 100 m

$$\begin{aligned} A_{min} &= \frac{E_e}{P_{min}} \\ &= \frac{17 \text{ fW}}{4.4 \frac{\mu\text{W}}{\text{m}^2}} \\ &= 3.0 \cdot 10^{-9} \\ &= 0.0039 \text{ mm}^2 \end{aligned} \quad (\text{A.3})$$

Now a fitting size of the pinhole can be chosen, based on the calculations above. For making further design and calculations easier it is therefore chosen that exactly one quarter of each photodiode needs to be covered by light at the reference position, as this gives a superfluous amount resolution. This makes it possible to determine the size of the pinhole, but as the size is different for different shapes, a short analysis of the shape of the pinhole is made.

The shape of the pinhole determines the shape of the light beam as it moves across the photodiodes when the angle of incident changes. To make calculations easier during flight it is desired to have a relation between change of area and angle of incident as linear as possible.

Two simple shapes, a square and a circle, are investigated and the linearity of their area-to-angle relations are compared. The reason that these two shapes are chosen, is due to how the photodiodes

are placed together. The photodiodes are placed symmetrically both vertically and horizontally around a center as can be seen on figure A.1. Therefore the shape of the pinhole should be symmetrical in this way too. For simplicity only regular polygons are considered and only regular polygons with an even number of sides has the desired symmetries. The square and the circle lies at each end of the spectrum of shapes with  $2n$  sides, and therefore the characteristics of all other shapes should lie somewhere between these two, thus these two shapes are examined.

### A.0.1 Deriving sizes for a square and a circular pinhole

For a square pinhole, the size needed to cover a quarter of each photodiode when in the reference position is exactly the square with corners at the center of each photodiode. Thus, this square has the dimensions seen in figure A.1, which is 1.91 mm on each side.

For a circular pinhole, deriving the size is done by finding an expression for the area that covers the photodiode, then solving for the radius when the area is equal to one quarter of one photodiodes area.

As the expression is for an area under a curve, it is found as a definite integral. The curve is a circle with radius,  $r$ , and center in the center of the component as seen in figure A.2

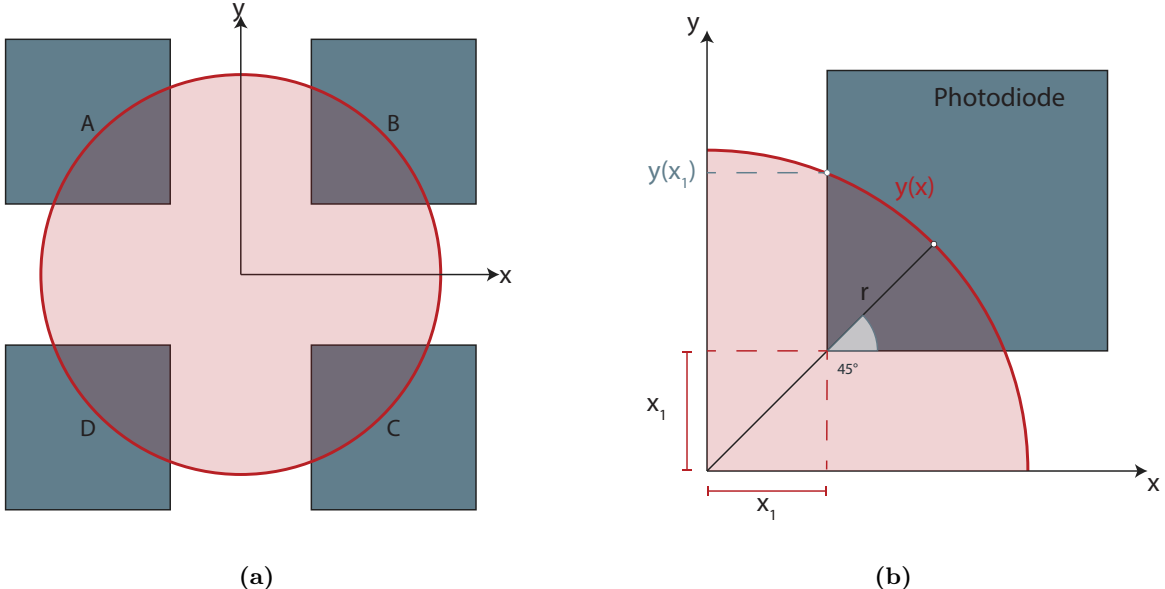


**Figure A.2:** Illustrations of photodiodes with circular pinhole overlay (a) and of a single photodiode together with a quarter circle of a pinhole (b).

Thus the circle can be expressed as:

$$x^2 + y^2 = r^2 \Rightarrow y(x) = \sqrt{r^2 - x^2} \quad (\text{A.4})$$

The area is then expressed by the integral in equation A.5

$$A = \int_{x_1}^{y(x_1)} y(x) dx - x_1 \cdot (y(x_1) - x_1) \quad (\text{A.5})$$

### A.1. Relationship between area and angle of incidence.

where  $x_1$  is half of the width of the dead space as illustrated on figure A.1. Using a CAD tool and solving for  $r$  when the area is equal to one quarter of the photodiode, gives a radius of 1.196 mm.

Now that the size of both a square and a circle is determined, the linearity of their relations between change in angle of incident and change in area can be examined.

## A.1 Relationship between area and angle of incidence.

To compare the relations, first an expression for each shape has to be found.

Starting with the circle, an expression for the width of the displaced area,  $d$ , can be derived via trigonometry corresponding to figure A.3.

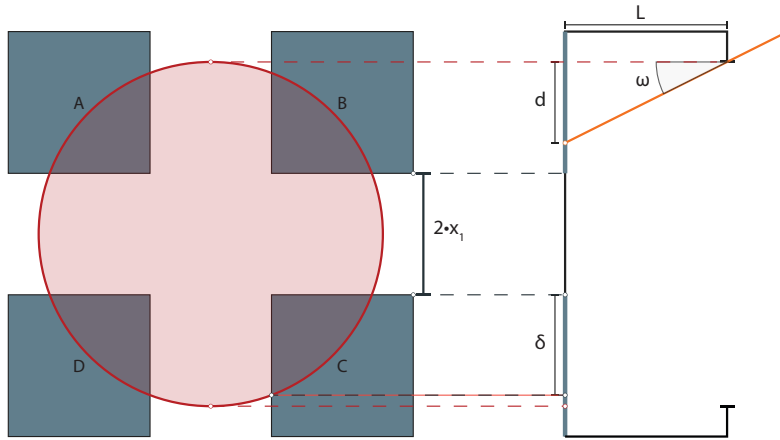


**Figure A.3:** Illustration of photodiodes seen from above and from the side, in the case of a circular pinhole

Thus the displacement is found as

$$d = L \cdot \tan \omega \quad (\text{A.6})$$

On figure A.3 some different dimensions are labelled:

- $l_d$  is the length of a photodiode.
- $x_1$  is half the length of the dead space.
- $\delta$  is the distance from the edge of the dead space to the projection of the edge of the pinhole onto the photodiode.
- $L$  is the distance from the pinhole to the photodiodes.
- $\omega$  is the angle of incident.
- $d$  is the displacement of the light beam due to a change in  $\omega$ .

For a square pinhole, a similar illustration can be made, as seen in figure A.4.

### A.1. Relationship between area and angle of incidence.

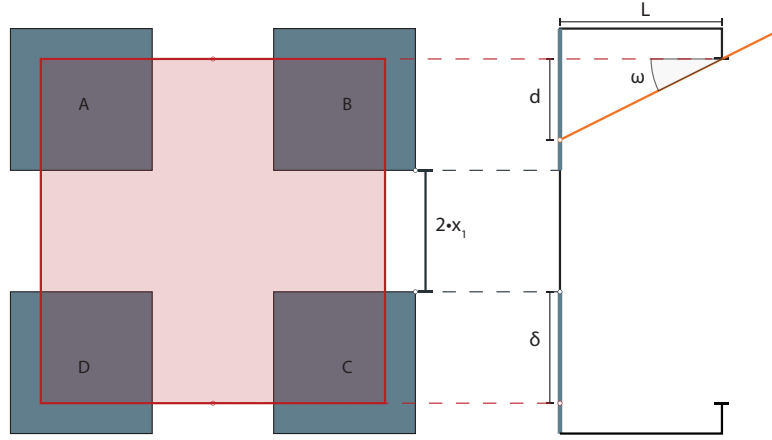


**Figure A.4:** Illustration of photodiodes seen from above and from the side, in the case of a square pinhole

Here  $\delta$  is exactly half the length of a photodiode, and the expression for the displacement is the same as before.

If the displacement is drawn onto the top-view of the photodiodes together with both a circular and a square pinhole, one gets the illustrations in figure A.5

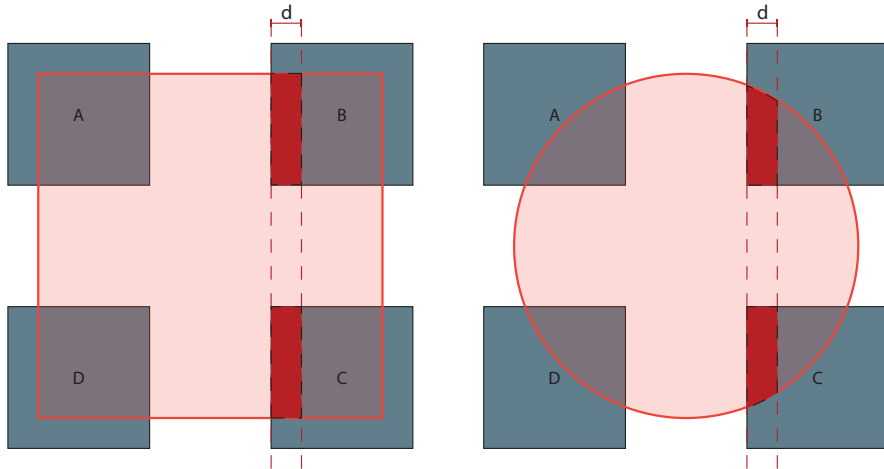


**Figure A.5**

Here the desired area is represented as the greyed-out parts. An expression for the area under each curve can be found as an integral as such.

$$A_{square} = 2 \cdot \int_0^d \delta \, dx \quad \wedge \quad A_{circle} = 2 \cdot \left( \int_{x_1}^d y(x) \, dx - x_1 \cdot (y(x_1) - x_1) \right) \quad (\text{A.7})$$

The expression for the square is simply the length of the area times the displacement  $d$ . The expression for the circle is derived as the area under part of the curve given by the circle  $y(x)$ .

However, both of these expressions depend on the displaced area  $d$ , which in turn depends on the

### A.1. Relationship between area and angle of incidence.

distance,  $L$ , between the photodiodes and the pinhole. Thus the influence of  $L$  on the areas is examined.

Plotting the area as function of angle of incident, for different values of  $L$ , a tendency is visible as seen on figure A.6.

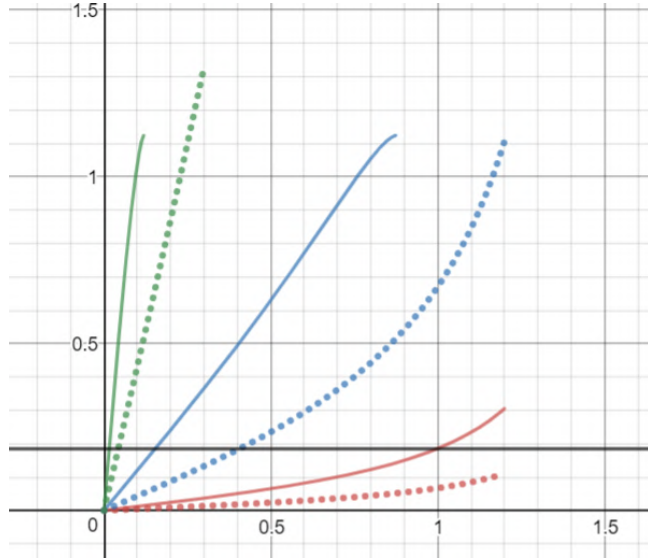


**Figure A.6:** The area displaced in  $mm^2$  as function of inclination angle in rad. (Add lidt omkring hvilke farver der er hvad)

Here three different distances are chosen, 0.1 mm, 1 mm and 10 mm. When the length exceeds 10 mm, the slope does not change significantly. As  $L$  increases the slope of the graph increases as well and the circle seems to be the most linear of the two. To determine more precisely which is most linear, a linear regression is made based on each curve, and the  $R^2$ -values are compared. The curves are bounded by zero and the angle that displaces an area the size of a quarter photodiode. These values can be seen in table A.1

**Table A.1:** Calculated R-squared values for different values of  $L$ .

$L$	R-squared for circle	R-squared for square
0.1 mm	0.9735	0.8494
1.0 mm	1.0000	0.9995
10 mm	1.0000	1.0000

From this it is concluded that the circle are either more linear than or just as linear as a square and therefore a circle is chosen as the shape of the pinhole. A note should also be made about the graphs for  $L = 10mm$ , that due to the steepness of the slope, the dynamic range of the angle of incident is very small. Thus, even though the relation is almost exactly linear, it is not feasible for use in practical use.

With the size and shape chosen, only the distance  $L$  is left to determine. To determine this distance, a choice is made based on the desired field of view (FOV) of the projectile. The FOV is the angle over which the projectile is able to discern the light from the target. Due to the symmetry of the pinhole and the photodiodes, the FOV angle can be divided into two equal parts on the x-axis or y-axis of a coordinate system imposed as on figure ???. These parts reflect an identical angle deflection from the reference position, in either direction, that results in identical displacements of the light

### A.1. Relationship between area and angle of incidence.

beam hitting the photodiodes. Thus only displacement in one direction is needed to acquire the full FOV. Two different FOVs are considered for the projectile, the first corresponds to the displacement of  $l_d - \delta$  as seen on figure (a). Beyond this, the total amount of light hitting the photodiodes starts decreasing, but position detection is still possible. The second FOV corresponds to the displacement of  $\delta$ , as seen on figure (b). Beyond this, only one half plane is hit by light and the position of the light beam can only be determined in one dimension.

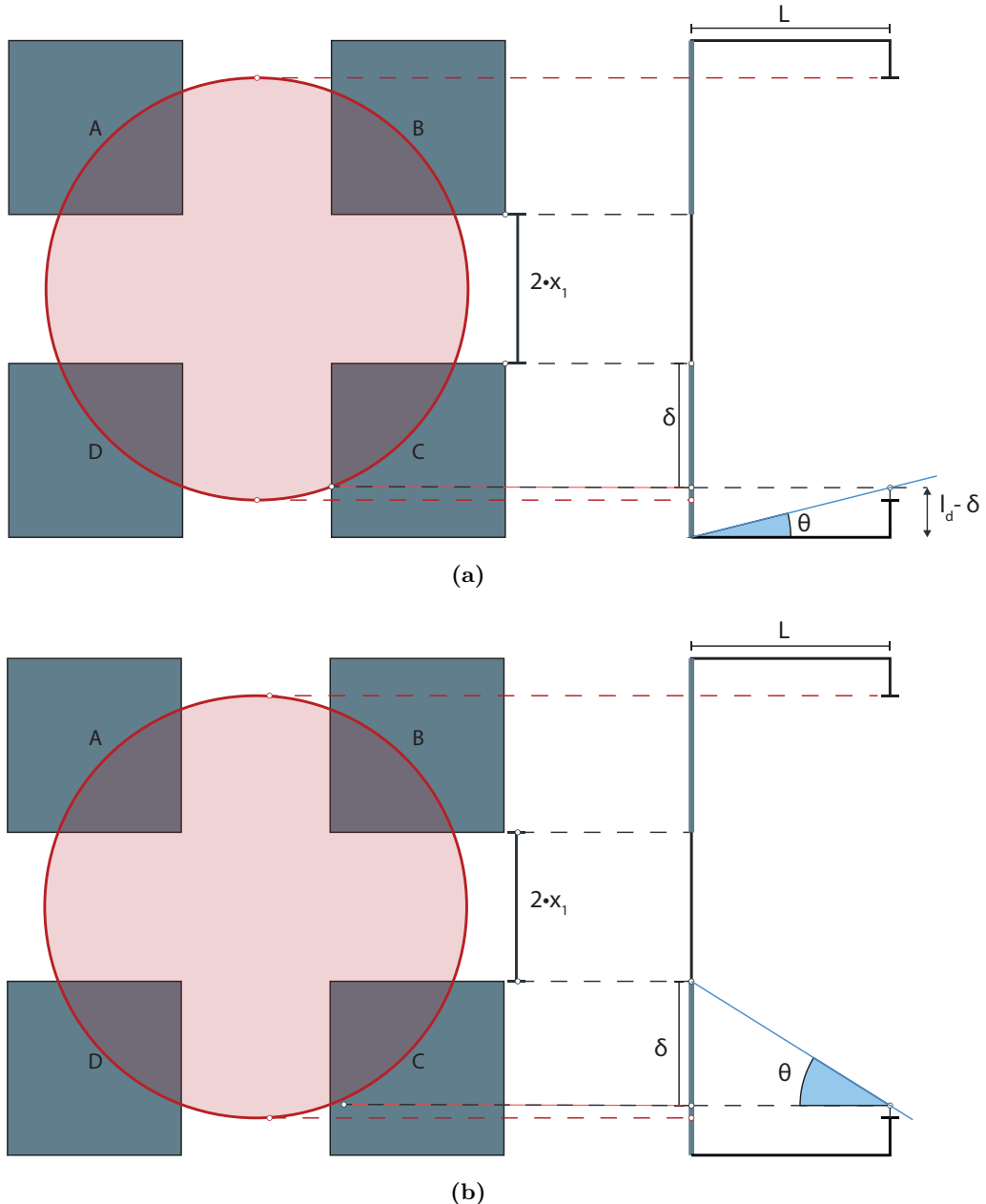


**Figure A.7**

The expressions for both FOVs are derived using trigonometry, using the illustrations from figure A.7.

### A.1. Relationship between area and angle of incidence.

For the first FOV:

$$\begin{aligned}
 FOV &= 2 \cdot \arctan\left(\frac{l_d - \delta}{L}\right) \\
 &= 2 \cdot \arctan\left(\frac{0.86 - (y(x_1) - x_1)}{L}\right) \\
 &= 2 \cdot \arctan\left(\frac{0.86 - 0.55}{L}\right)
 \end{aligned} \tag{A.8}$$

For the second FOV:

$$\begin{aligned}
 FOV &= 2 \cdot \arctan\left(\frac{\delta}{L}\right) \\
 &= 2 \cdot \arctan\left(\frac{(y(x_1) - x_1)}{L}\right) \\
 &= 2 \cdot \arctan\left(\frac{0.55}{L}\right)
 \end{aligned} \tag{A.9}$$

Solving for  $L$  when the first FOV is 90 degrees results in a distance of 0,31mm between the photodiodes and the pinhole.

With this, all the properties of the pinhole has been determined. The pinhole should be a circle with a radius of  $1.196mm$ , placed  $0.31mm$  above the photodiodes.

## Appendix B

# Photodiode Amplifier Bandwidth, Stability and Noise Analysis

The photodiode and current-to-voltage converter circuit consists of a combination of figure 6.7 and figure 6.8, it can be seen on figure B.1. To be able to design and implement this circuit so it fulfils its requirements, it is necessary to analyse the bandwidth, stability and noise components of the circuit.

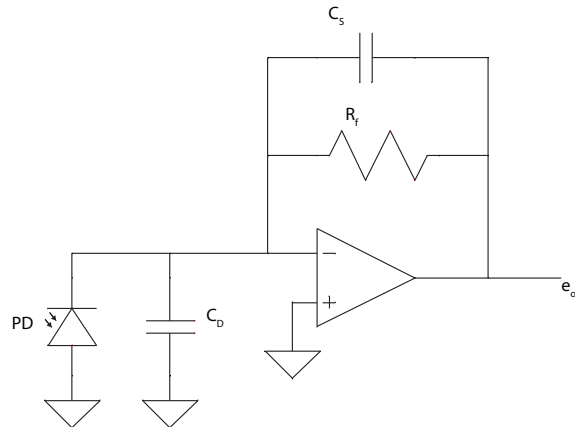


**Figure B.1:** Circuit of the photodiode amplifier [27, p. 23]

### B.1 Bandwidth of the TIA

The bandwidth of the circuit is limited by several factors. First there is the parasitic capacitance  $C_S$  of the feedback resistor, for a given resistance there is a corresponding stray capacitance value, the bandwidth limit caused by this capacitance is calculated by equation B.1 [27, p. 32].

$$f_{C_S} = \frac{1}{2 \cdot \pi \cdot R_f \cdot C_S} \quad (\text{B.1})$$

This frequency limit occurs due to the stray capacitance allowing  $i_p$  to bypass  $R_f$  because  $C_S$  shunts  $R_f$ . Thus,  $C_S$  creates a roll off effect with its pole at  $f_{C_S}$  and when this is the dominant frequency limit of the circuit, the -3-dB bandwidth is placed at this pole [27, p. 32].

## B.2. Stability of the TIA

The second limiting factor is the open-loop gain  $A_{OL}$  limit of the op-amp. As mentioned in section 6.5.2, the op-amp removes all voltage output produced by the photodiode at the amplifier input due to the virtual ground at its input. In practise, there is still a small voltage signal presented to the photodiode, this voltage is the op-amp gain error  $e_{gi}$  and it is determined by equation B.2 [27, p. 33].

$$e_{gi} = \frac{e_o}{A_{OL}} \quad (\text{B.2})$$

$e_{gi}$  in combination with the junction capacitance of the diode shunts the diode at high frequencies and create another roll off effect. Ideally, the op-amp has an infinite gain which results in virtually zero gain error at the input and then the feedback can produce a virtual ground at the amplifier input. For low frequencies, the op-amps  $A_{OL}$  is high enough that the ideal scenario can be assumed as a decent approximation. For high frequencies the  $A_{OL}$  magnitude decreases, therefore the op-amps bandwidth creates the roll off effect which is the second bandwidth limit of the circuit [27, p. 34].

## B.2 Stability of the TIA

At the input of the amplifier there is an impedance, which varies with frequency [27, p. 37]. To obtain a stable feedback loop it is important to employ phase compensation so that the loop never becomes an oscillator. By plotting the two curves of the amplifier's available gain  $A_{OL}$  and the required gain of the feedback  $1/\beta$  the graph shows a frequency intercept  $f_i$  of the two curves, this graph can be seen on both figures in figure B.2. The required gain of the feedback is calculated using equation B.3 [27, p. 39].

$$\frac{1}{\beta} = 1 + R_f \cdot C_i \cdot s \quad (\text{B.3})$$

Where  $C_i = C_D + C_{id} + C_{icm}$  is the combined input capacitance of the feedback loop. Here,  $C_D$  is the diode junction capacitance,  $C_{id}$  is the amplifiers differential input capacitance and  $C_{icm}$  is the amplifiers common-mode inverting input capacitance. When the gain curves of  $A_{OL}$  and  $1/\beta$  have a slope of 20 dB/decade (i.e. a phase shift of  $90^\circ$ ) at the intercept point in combination with the  $180^\circ$  phase shift of the feedback loop, oscillation will occur due to a total phase shift of  $360^\circ$ , this response can be seen on figure B.2(a).

## B.2. Stability of the TIA

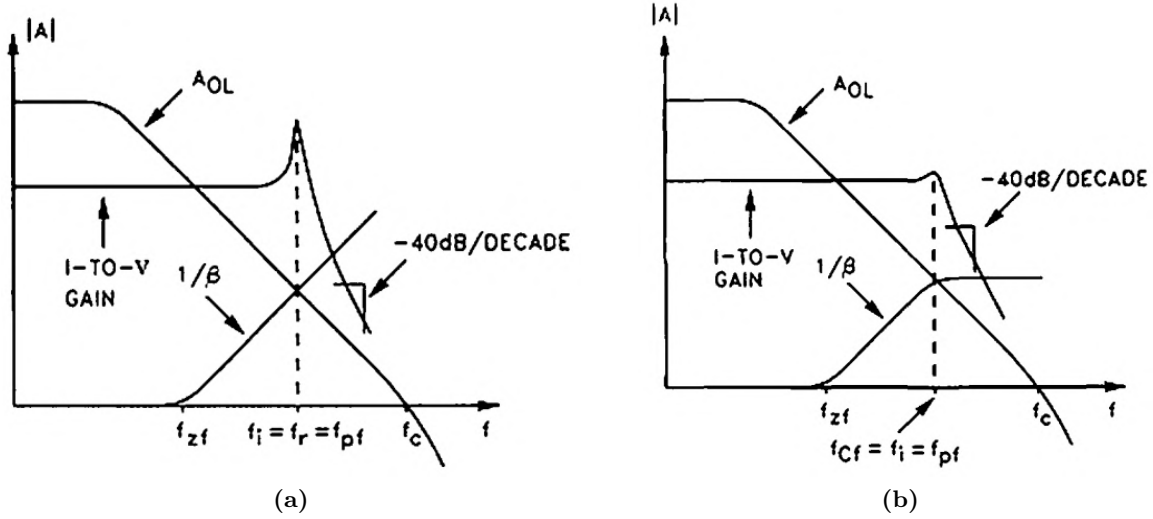


**Figure B.2:** Two gain graphs for the circuit containing a photodiode with a current-to-voltage converter and amplifier [27, p. 40 & 43]

The intercept frequency is determined by equation B.4 [27, p. 41].

$$f_i = \sqrt{f_{zf} \cdot f_c} \quad (\text{B.4})$$

The zero of the feedback demand  $f_{zf}$  is given by equation B.5 [27, p. 40].

$$f_{zf} = \frac{1}{2 \cdot \pi \cdot R_f \cdot C_i} \quad (\text{B.5})$$

The unity-gain bandwidth  $f_c$  is the frequency where  $A_{OL}$  is 0 dB, this frequency is available in the given op-amp datasheet.

There are several methods to stabilise the feedback via phase compensation, the best performance is obtained by employing a feedback capacitor  $C_f$  in parallel with  $R_f$ .  $C_f$  adds a zero response to the circuit's feedback factor to cancel out the pole, which is produced by the input capacitance of the feedback loop. This response can be seen on figure B.2(b), the  $1/\beta$  graph is rolled off by the  $-45^\circ$  phase shift of  $C_f$  and therefore no longer has a  $90^\circ$  phase shift at  $f_i$ . The value of  $C_f$  can be approximated for the case of  $C_i \gg C_f$  by equation B.6 [27, p. 49].

$$C_f = \sqrt{C_i \cdot C_c} \quad \text{for } C_i \gg C_f \quad (\text{B.6})$$

This makes  $C_f$  a geometric average of the feedback input capacitance and an artificial capacitance  $C_c$ . However, the result of equation B.6 is only valid for  $C_i \gg C_f$  where  $C_f$  is unknown at first, but this is easily solved by calculating  $C_f$  and then evaluating the inequality. As it can be noted in equation B.5  $C_i$  is linked to  $R_f$  as seen here:

$$C_i = \frac{1}{2 \cdot \pi \cdot R_f \cdot f_{zf}}$$

A similar relationship is also desired for the artificial capacitance, thus  $C_c$  is defined by equation B.7 [27].

$$C_c = \frac{1}{2 \cdot \pi \cdot R_f \cdot f_c} \quad (\text{B.7})$$

For practical implementations, the stray capacitance  $C_S$  of  $R_f$  is often in the range of 0.2 pF to 0.5 pF for Surface Mount Device (SMD) resistors, this stray capacitance may be enough to compensate the phase [28, p. 11]. However, parasitic capacitance which arise from PCB routing will contribute to a higher value of  $C_i$ , therefore it is required to tune the value of  $C_f$  empirically [27, p. 50].

### B.3 RMS Noise Analysis of the TIA

For the photodiode application, the TIA has a very complex noise performance. The complete noise analysis consist of multiple noise components and displays a frequency varying noise figure. The three major noise components is the feedback resistor, input noise current and noise voltage of the op-amp, the sum of these components is the total output noise  $e_{no}$  [27, p. 88]. The output noise component of the feedback resistor  $e_{noR}$  and the amplifier's input current noise  $e_{noi}$  remain constant with frequency until they are eventually rolled off by the bandwidth limit of the circuit. Furthermore, the output noise component of the amplifier's input voltage noise  $e_{noe}$  varies with frequency which makes simple calculations inadequate. However, to simplify the calculation of this noise component it is split into multiple sub-components for each of their own frequency region [27, p. 88]. A circuit model based on the photodiode and TIA with the three noise components is shown on figure B.3 Here, the input capacitance of the amplifier is  $C_{ia} = C_{id} + C_{icm}$ .

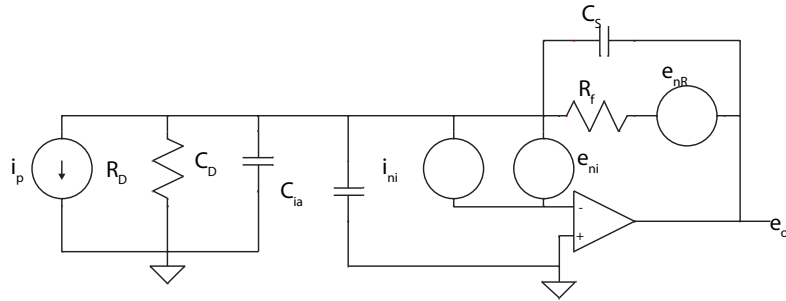


**Figure B.3:** Circuit of the photodiode model and TIA with the three noise components and input capacitance[27, p. 89]

Starting off, the resistor's noise voltage has a spectral density calculated by equation B.8 [27, p. 89]

$$e_{nR} = \sqrt{4 \cdot K \cdot T \cdot R_f} \quad (\text{B.8})$$

Where  $K$  is the Boltzmann's constant at  $1.381 \times 10^{-23} \text{ J}/\text{K}$  and  $T$  is the temperature in  $^{\circ}\text{K}$  [27, p. 89]. If the TIA is set to unity gain, i.e.  $R_f = 1\Omega$ , then the output noise component  $e_{noR}$  is equal to  $e_{nR}$ . When  $R_f$  is increased the output signal  $e_o$  rises due to  $e_o = i_p \cdot R_f$ , in turn the signal to noise ratio is improved by the square root of  $R_f$  as seen in equation B.9 [27, p. 89].

$$\frac{i_p \cdot R_f}{e_{noR}} = i_p \cdot \sqrt{\frac{R_f}{4 \cdot K \cdot T}} \quad (\text{B.9})$$

This property of  $e_{nR}$  is exceptional because the signal to noise ratio is improved with an increased value of  $R_f$ , where the only downside to increasing  $R_f$  is its effect on the bandwidth. However, this calculation does not account for the other noise components which also affect the noise performance of the circuit. Thereby, it is not a prerequisite that  $R_f$  should be as large as possible [27, p. 90]. The next noise component is the input noise current  $i_{ni}$ , this is the effect of the input bias current  $I_{B-}$  of the op amp,  $i_{ni}$  is calculated by equation B.10.

$$i_{ni} = \sqrt{2 \cdot q \cdot I_{B-}} \quad (\text{B.10})$$

Where  $q$  is the charge of an electron ( $1.6 \times 10^{-19} \text{ C}$ ) and  $I_{B-}$  is found in the op amp datasheet. During the operation of the feedback loop  $i_{ni}$  flows through  $R_f$  and to the output of the op amp producing a noise voltage  $e_{nRi}$ , this voltage can be calculated with equation B.11 [27, p. 90].

$$e_{nRi} = i_{ni} \cdot R_f \quad (\text{B.11})$$

### B.3. RMS Noise Analysis of the TIA

Similar to how  $e_{nR}$  directly appears at the output at unity gain, the output noise of the amplifier's input current noise  $e_{noi}$  is equal to  $e_{nRi}$  at unity gain [27, p. 90].

At last, there is the input voltage noise of the op amp. This is the noise component which varies with frequency as a function of the feedback resistance, stray capacitance of  $R_f$  and the input capacitance before it is finally rolled off by the open loop gain of the op amp. Contrary to the two previous noise components,  $e_{ni}$  does not transfer to the output with a low noise gain  $A_{ne}$ . Instead  $A_{ne}$  is close to unity at lower frequencies due equation B.12 [27, p. 90].

$$A_{ne} = 1 + \frac{R_f}{R_D} \quad (\text{B.12})$$

There,  $R_D$  is extremely large which results in a near unity  $A_{ne}$ . Now, as frequency increase, the junction capacitance  $C_D$  of the photodiode shunts the  $R_D$  which in turn increases  $A_{ne}$ . The complete function of  $A_{ne}$  can be seen on figure B.4, which is gain graph with a logarithmic frequency scale.

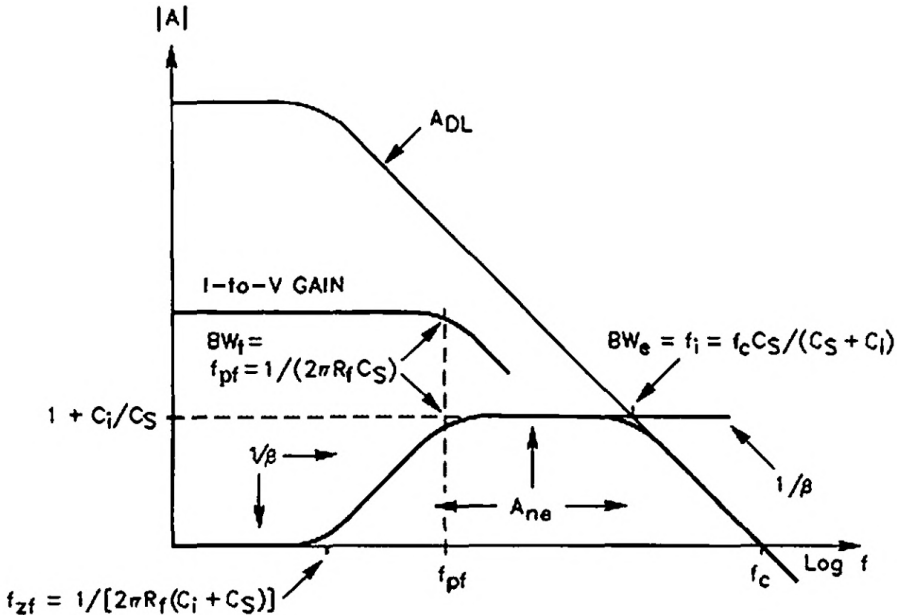


**Figure B.4:** Gain graph of the TIA circuit which shows the variation in noise gain for the op-amps input voltage noise [27, p. 91].

To make matters worse, the input capacitance of the op amp,  $C_{id}$  and  $C_{icm}$ , are in parallel with  $C_D$  and the sum of these three capacitors is  $C_i$ . thereforee, this total input capacitance gives rise to  $A_{ne}$  at even lower frequencies than before. The rise of  $A_{ne}$  is like a zero response and the frequency of this zero is determined by equation B.13 [27, p. 91].

$$f_{zf} = \frac{1}{2 \cdot \pi \cdot R_f \cdot (C_i + C_S)} \quad (\text{B.13})$$

The noise gain along this zero response is determined by equation B.14 [27, p. 90].

$$A_{ne} \approx 1 + R_f \cdot C_i \cdot s \quad (\text{B.14})$$

Now, as mentioned earlier the stray capacitance of  $R_f$  is a significant part of this noise function.  $C_S$  cancels the zero response and thus the rising  $A_{ne}$  with a pole response at the pole frequency  $f_{pf}$  which is determined by equation B.15 [27, p. 91].

$$f_{pf} = \frac{1}{2 \cdot \pi \cdot R_f \cdot C_S} \quad (\text{B.15})$$

### B.3. RMS Noise Analysis of the TIA

This is due to  $C_S$  shunting  $R_f$  and effectively bypassing the resistor which levels off the rise of  $A_{ne}$ . Since  $C_S$  bypasses  $R_f$  the noise gain is found via equation B.16 [27, p. 91].

$$A_{ne} = 1 + \frac{C_i}{C_S} \quad (\text{B.16})$$

As the level response of  $A_{ne}$  approaches the  $A_{OL}$  roll off it runs into a second pole response. This second pole is located at  $BW_e$  which is found by equation B.17 [27, p. 91].

$$BW_e = \frac{f_c \cdot C_S}{C_S + C_i} \quad (\text{B.17})$$

Now that the complete response of  $A_{ne}$  has been established for the varying frequency, a function for the complete output noise  $e_{noe}$  of the amplifier's input voltage noise  $e_{ni}$  can be established in equation B.18 [27, p. 91].

$$e_{noe} = \frac{1 + R_f \cdot (C_i + C_S) \cdot s}{1 + R_f \cdot C_S \cdot s} \cdot e_{ni} \quad (\text{B.18})$$

Thereby, with the three noise densities,  $e_{noR}$ ,  $e_{noi}$  and  $e_{noe}$ , established the complete output noise density of the amplifier  $e_{no}$  can be calculated as an RMS summation. However, this summation would still remain a function of frequency due to  $e_{noe}$  and therefore requires RMS integration [27, p. 92]. To solve this problem, each noise density should receive its own RMS integration before the final summation is calculated.

The two first RMS summations are carried out for  $e_{noR}$  and  $e_{noi}$  which become  $E_{noR}$  and  $E_{noi}$  respectively. As mentioned before these two noise components are linear for the whole bandwidth  $BW_t$  of the TIA with a corresponding approximation of unity noise gain.  $BW_t$  is the pole frequency where the current-to-voltage gain starts to roll off, this response can also be seen on B.4 where  $BW_t$  is equal to  $f_{pf}$ . This response occurs due to  $C_S$  shunting  $R_f$ , which is also why  $BW_t$  is referred to as the transresistance bandwidth. Similar to  $f_{pf}$  in equation B.15,  $BW_t$  is calculated by equation B.19 [27, p. 93].

$$BW_t = \frac{1}{2 \cdot \pi \cdot R_f \cdot C_S} \quad (\text{B.19})$$

Now, with  $BW_t$  determined  $E_{noR}$  and  $E_{noi}$  can be calculated with equation B.20 and B.21 respectively [27, p. 93].

$$E_{noR} = \sqrt{2 \cdot K \cdot T \cdot R_f \cdot \pi \cdot BW_t} \quad (\text{B.20})$$

$$E_{noi} = R_f \sqrt{q \cdot \pi \cdot BW_t \cdot I_{B-}} \quad (\text{B.21})$$

Determining  $E_{noe}$  is a longer process than the two other RMS noise components, due to the varying noise gain  $A_{ne}$ . The conversion to RMS cannot simply be carried out in one single equation, instead it must be divided into separate frequency regions and then summed up. therefore it is required to define these frequency regions and the corresponding noise characteristics of  $e_{ni}$  for the given region and noise gain. Along these lines,  $E_{noe}$  is split into five sub-components for five bandwidth regions, a graph of this can be seen on figure B.5.

### B.3. RMS Noise Analysis of the TIA

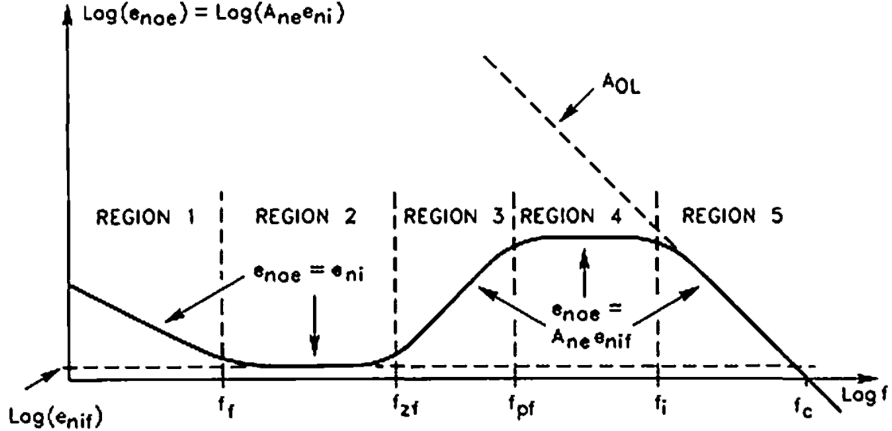


Figure B.5: [27, p. 96].

The first region is at low frequencies and is dominated by the  $1/f$  noise slope of  $\sqrt{1/f}$ , this is also known as pink noise. As is the definition of  $1/f$  noise, the magnitude of the noise decreases until it reaches a noise floor at  $f_f$  where the second region begins. As a result of  $1/f$  continuing until 0 Hz the entire RMS value of the noise component cannot be calculated due to a 0 Hz limit. therefore, a lower limit of the RMS equation is chosen as  $f_1 = 0.01$  [27, p. 97]. Now, the equation for  $E_{noe1}$  can be presented in equation B.22 [27, p. 97].

$$E_{noe1}^2 = \int_{f_1}^{f_f} \left| e_{nif} \cdot \frac{f}{f} \right|^2 df = e_{nif}^2 \cdot f_f \cdot \ln \left( \frac{f_f}{f_1} \right) \quad (\text{B.22})$$

Where the input noise floor  $e_{nif} = e_{ni}$  and  $1/f$  corner frequency  $f_f$  is given by B.23 [44].

$$f_f = \frac{e_{n_{pn}}^2}{e_{n_{wn}}^2} \quad (\text{B.23})$$

$e_{n_{pn}}$  is the pink noise density, which is found in the op-amp datasheet usually for 0.1 Hz to 10 Hz.  $e_{n_{wn}}$  is the white noise density, which is found in the input voltage noise spectral density graph of the op-amp datasheet.

The second region consists of the constant noise floor  $e_{nif} = e_{ni}$  with a unity noise gain  $A_{ne}$ . The limits of this region is  $f_f$  and  $f_{zf}$  is determined by equation B.24 [27, p. 98].

$$f_{zf} = \frac{1}{2 \cdot \pi \cdot R_f \cdot (C_i + C_s)} \quad (\text{B.24})$$

Consequently the RMS value of the noise component  $E_{noe2}$  is obtained via equation B.25 [27, p. 98].

$$E_{noe2}^2 = \int_{f_f}^{f_{zf}} |e_{nif}|^2 df = e_{nif}^2 \cdot (f_{zf} - f_f) \quad (\text{B.25})$$

The third region is where the  $e_{ni}$  is amplified by a rising  $A_{ne}$ , which has a zero response as explained earlier. The limits of this region is  $f_{zf}$  from equation B.24 and  $f_{pf}$  from equation B.15. The resulting RMS value of the noise component  $E_{noe3}$  is obtained from equation B.26 [27, p. 98]

$$E_{noe3}^2 = \int_{f_{zf}}^{f_{pf}} \left| \frac{e_{nif} \cdot f}{f_{zf}} \right|^2 df = \left( \frac{e_{nif}}{f_{zf}} \right)^2 \cdot \frac{(f_{pf}^3 - f_{zf}^3)}{3} \quad (\text{B.26})$$

The fourth region is where  $A_{ne}$  becomes level by the pole response which appears at the pole frequency  $f_{pf}$ . Similar to the second region  $e_{ni} = e_{nif}$  however the noise gain calculated in equation B.16 is

### B.3. RMS Noise Analysis of the TIA

present. This region ends as the amplifier is rolled off at the intercept frequency  $f_i$  which is calculated in equation B.27

$$f_i = \frac{f_c \cdot C_S}{C_i + C_s} \quad (\text{B.27})$$

Then, the RMS value can be calculated by equation B.28

$$E_{noe4}^2 = \int_{f_{pf}}^{f_i} \left| \left( \frac{1 + C_i}{C_s} \right) \cdot e_{nif} \right|^2 df = \left( \left( \frac{1 + C_i}{C_S} \right) \cdot e_{nif} \right)^2 \cdot (f_i - f_{pf}) \quad (\text{B.28})$$

The fifth region is where  $A_{ne}$  is rolled off by the  $A_{OL}$  decrease. This roll off begins at  $f_i$  where  $A_{ne}$  sees a pole response and then it declines until it hits  $f_c$ , which is the unity-gain crossover frequency of the op-amp. Because the noise gain follows the  $A_{OL}$  roll off its gain is defined by:  $A_{ne} = f_c/f$  where  $f$  is the varying frequency. Again, the regions input voltage noise is given by the voltage noise floor which is amplified by  $A_{ne}$ . Thus the RMS value of the fifth region is given by equation B.29 [27, p. 99].

$$E_{noe5}^2 = \int_{f_i}^{\infty} \left| \left( \frac{e_{nif} \cdot f_c}{f} \right) \right|^2 df = \frac{(e_{nif} \cdot f_c)^2}{f_i} \quad (\text{B.29})$$

Finally, calculating  $E_{noe}$  becomes the simple task of summing the five RMS values of the op-amp input voltage noise for each separate frequency region [27, p. 100].

$$E_{noe} = \sqrt{E_{noe1}^2 + E_{noe2}^2 + E_{noe3}^2 + E_{noe4}^2 + E_{noe5}^2} \quad (\text{B.30})$$

Then, the net output noise  $E_{no}$  of the TIA can be calculated as an RMS summation, this is done in equation B.31 [27, p. 102].

$$E_{no} = \sqrt{E_{noR}^2 + E_{noi}^2 + E_{noe}^2} \quad (\text{B.31})$$

## Appendix C

# Input Impedance of MFB Bandpass Filter

This appendix describes the process of finding the input impedance of an active MFB bandpass filter.

### C.1 Defining Input Impedance

The input impedance of any circuit is defined as the input voltage divided by the input current, as seen in equation C.1.

$$Z_i = \frac{V_i}{I_i} \quad (\text{C.1})$$

Examining the circuit topology of the MFB bandpass filter in figure C.1 the input voltage  $V_i$  is known already. In order to find an expression for  $I_i$ , an analysis is required. It is seen that  $I_i = I_{R_1}$ , which can be expressed as  $\frac{V_i - V_x}{R_1}$ . The voltage drop across  $R_1$  can be expressed as  $V_i - V_x$ .

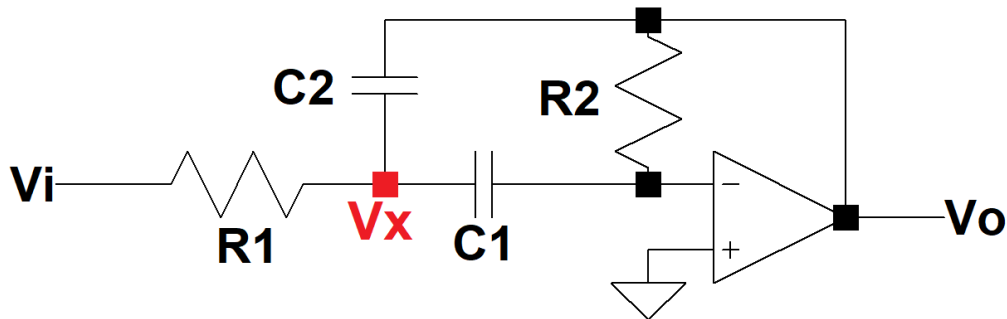


**Figure C.1:** Circuit diagram of an MFB filter.

The input impedance can now be described by equation C.2. In order to find an expression for  $V_x$ ,

## C.2. Circuit Analysis of MFB filter

the MFB bandpass circuit is analysed in section C.2.

$$Z_i = \frac{\frac{V_i}{V_i - V_x}}{R_1} \quad (C.2)$$

## C.2 Circuit Analysis of MFB filter

Examining the circuit in figure C.1, it is apparent that the circuit contains two voltage sources, namely  $V_i$  and  $V_o$ . The second voltage source comes as a consequence of the filter being active and containing an opamp. In order to find a way to express  $V_x$ , the superposition method is used. In the following circuits  $R_2$  is shorted to ground. This comes as a result of the input terminal of an ideal opamp functioning as a virtual zero or ground, when the other terminal is connected to ground.

First  $V_o$  is set to zero, thus shorting the supply to ground. This allows for finding  $V_x$  with  $V_i$  as the only voltage source. Doing so results in the circuit seen on figure C.2.

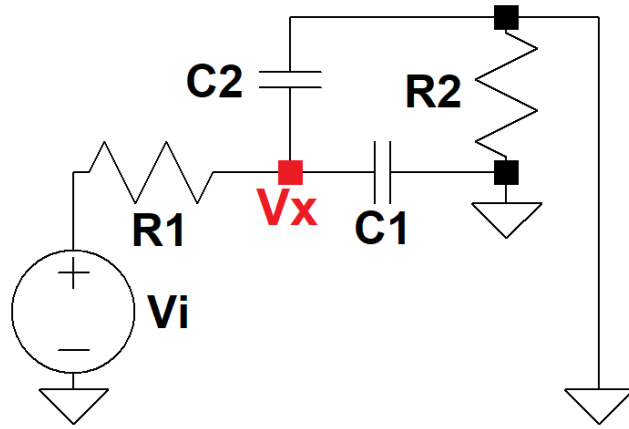


**Figure C.2:** Circuit diagram of MFB filter with  $V_o$  set to zero.

Analysing the circuit gives the expression in equation C.3 for  $V_x$ , which will be denoted as  $V_{x1}$ .

$$V_{x1} = \frac{\frac{1}{s(C_1 + C_2)}}{R_1 + \frac{1}{s + (C_1 + C_2)}} \cdot V_i \quad (C.3)$$

Next,  $V_i$  is set to zero and shorted to ground, thus allowing for  $V_x$  to be found for  $V_o$ . The circuit can be seen in figure C.3 and the expression is denoted as  $V_{x2}$  in equation C.4.

$$V_{x2} = \frac{\frac{R_1}{sC_1R_1 + 1}}{\frac{1}{sC_2} + \frac{R_1}{sC_1R_1 + 1}} \cdot V_o \quad (C.4)$$

## C.2. Circuit Analysis of MFB filter

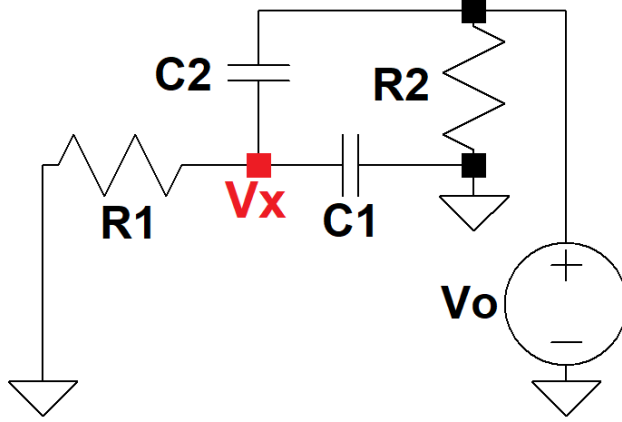


**Figure C.3:** Circuit diagram of MFB filter with  $V_i$  set to zero.

The final expression for  $V_x$  is found by adding  $V_{x1}$  and  $V_{x2}$ , which results in equation C.5.

$$V_x = \frac{V_i + sC_2R_1 \cdot V_o}{sC_1R_1 + sC_2R_1 + 1} \quad (\text{C.5})$$

Equation C.5 can now be substituted into equation C.2, which results in expression C.6. It should be noted that  $V_x$  includes both  $V_i$  and  $V_o$ . In order to remove  $V_o$ , it is replaced by  $V_i \cdot H(s)$ , where  $H(s)$  is the transfer function of the filter.

$$Z_i = \frac{\frac{V_i}{V_i + sC_2R_1V_i \cdot H(s)}}{\frac{sC_1R_1 + sC_2R_1 + 1}{R_1}} \quad (\text{C.6})$$

Reducing equation C.6 gives equation C.7.

$$Z_i = \frac{sC_1R_1 + sC_2R_1 + 1}{s \cdot (C_1 + C_2 - C_2 \cdot H(S))} \quad (\text{C.7})$$

Substituting  $H(s)$  in equation C.7 with the transfer function for the filter, see equation C.9 [30], gives equation C.8, which is the final expression for the input impedance of the filter. This equation is used for the filter design in section 6.6.3.

$$Z_{in} = \frac{C_1R_1s + C_2R_1s + 1}{s(C_1 + C_2 + \frac{1}{R_1(s^2 + (\frac{1}{C_1R_2} + \frac{1}{C_2R_2})s + \frac{1}{C_1C_2R_1R_2})})} \quad (\text{C.8})$$

$$H(s) = -\frac{\frac{1}{R_1C_1} \cdot s}{s^2 + (\frac{1}{R_2C_1} + \frac{1}{R_2C_2}) \cdot s + \frac{1}{R_1R_2C_1C_2}} \quad (\text{C.9})$$

## Appendix D

# Test journal: Trans-Impedance Amplifier

In the following appendix a test journal describing the test of the trans-impedance amplifier(TIA) can be read.

### D.1 Test purpose

The purpose of this test is to measure the frequency response of the TIA on each channel.

### D.2 Test frame

#### Theoretical background

The theoretical background can be found in section 6.5.2

#### Test setup, equipment and test procedure

The test was conducted in the group room and the test setup can be seen on figure D.1.

## D.2. Test frame

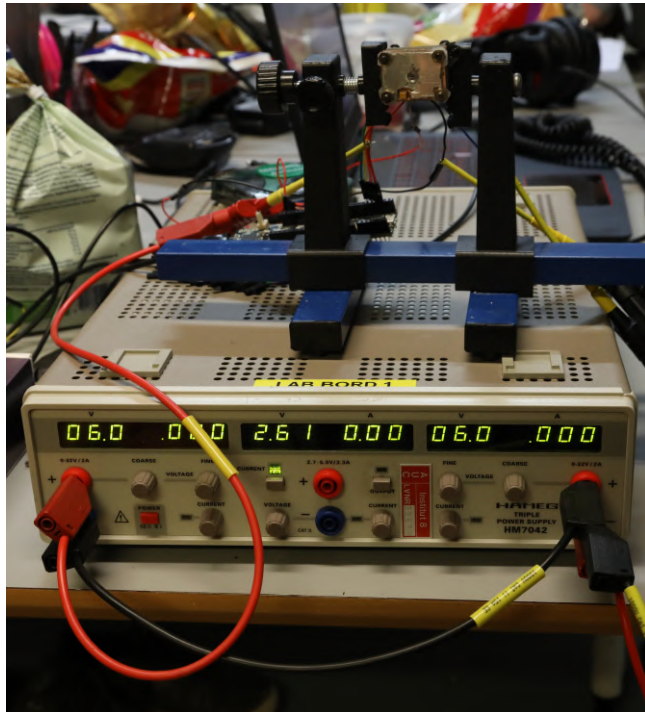


**Figure D.1:** Picture of the setup of the trans-impedance amplifier.

To test the Trans-impedance amplifier, a power supply of 5 V is connected to the TIA. To test the frequency response an Analog Discovery is connected to the target box, the Analog Discovery outputs a frequency sweep ranging from 300 hz to 30 kHz. The target box is placed 50 cm from the quad photodiode which gives it a "clear" input to the photodiode. The same Analog Discovery is connected to one of the four output channels of the TIA. This Analog Discovery is also connected to a computer which logs the data. The test is repeated until all four channels have been tested.

**Table D.1:** Table of equipment used in the test.

List of equipment		
Name / Description	Type	AAU-ID
Quad Photodiode	OPR5925	-
Trans-Impedance Amplifier	OPA2380	-
Target Box	LED LZ1-00R602	-
1 x Analog Discovery 2	-	-

### D.3. Test results and data processing

## D.3 Test results and data processing

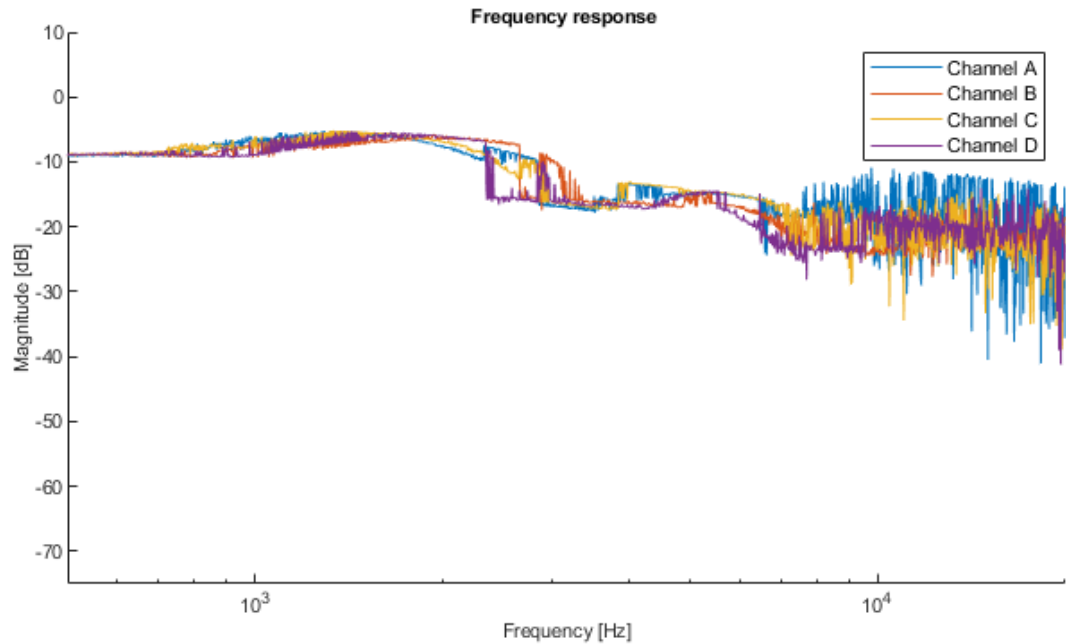


**Figure D.2:** Graph showing the frequency response of each channel.

# Appendix E

## Test journal: High Pass Filter

In the following appendix a testjournal of the high pass filter (HPF) can be read.

### E.1 Test purpose

The purpose of the test is to test the properties of the HPF.

### E.2 Test frame

#### Theoretical background

The theoretical background of the HPF can be read in section 6.6.3

#### Test setup, equipment and test procedure

The test was conducted in the group room and the test setup can be seen on figure E.1.

## E.2. Test frame

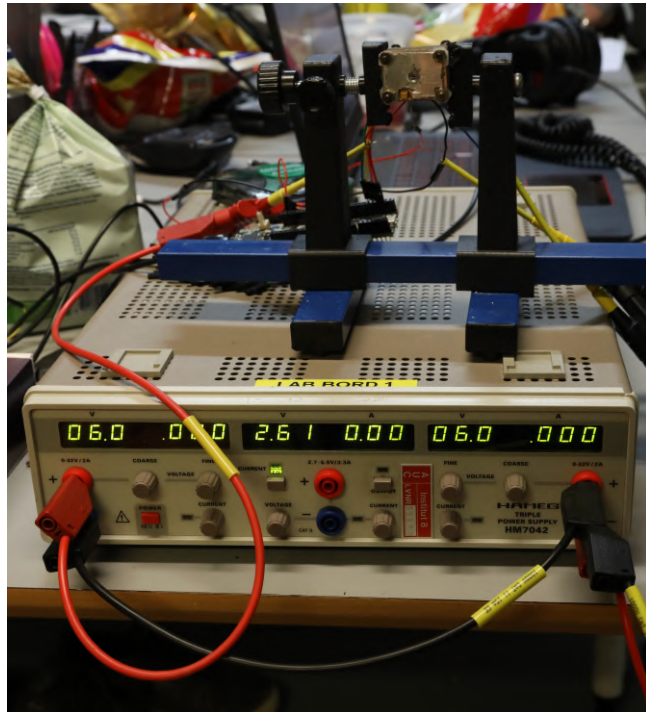


**Figure E.1:** Picture of the setup of the high pass filter.

To test the HPF firstly the Analog Discovery is connected to the input of the HPF. This Analog Discovery runs a frequency sweep ranging from 300 Hz to 30 kHz. Another Analog Discovery is connected to the output of one of the four channels of the HPF. This analog discovery is also connected to a computer which logs the data. The test is repeated until all four channels have been tested.

**Table E.1:** Table of equipment used in the test.

List of equipment		
Name / Description	Type	AAU-ID
High Pass Filter	-	-
1 x Analog Discovery 2	-	-

E.3. Test results and data processing

### E.3 Test results and data processing

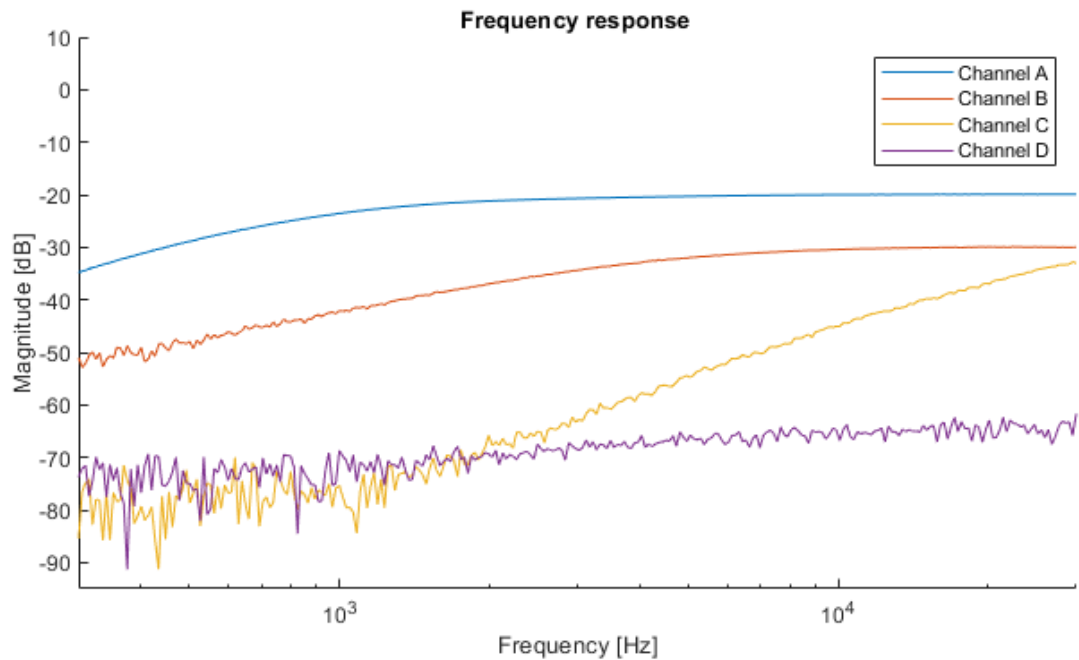


**Figure E.2:** Graph of the frequency response for each channel.

# Appendix F

## Test journal: Band Pass Filter

In this appendix a test journal of the band pass filter (BPF) can be read.

### F.1 Test purpose

The purpose of the the test is to do a spectrum analysis of the BPF on each channel.

### F.2 Test frame

#### Theoretical background

The theoretical background of the band pass filter can be found in section 6.6.3.

#### Test setup, equipment and test procedure

The test was conducted in the group room, and the setup can be seen on figure F.1

## F.2. Test frame

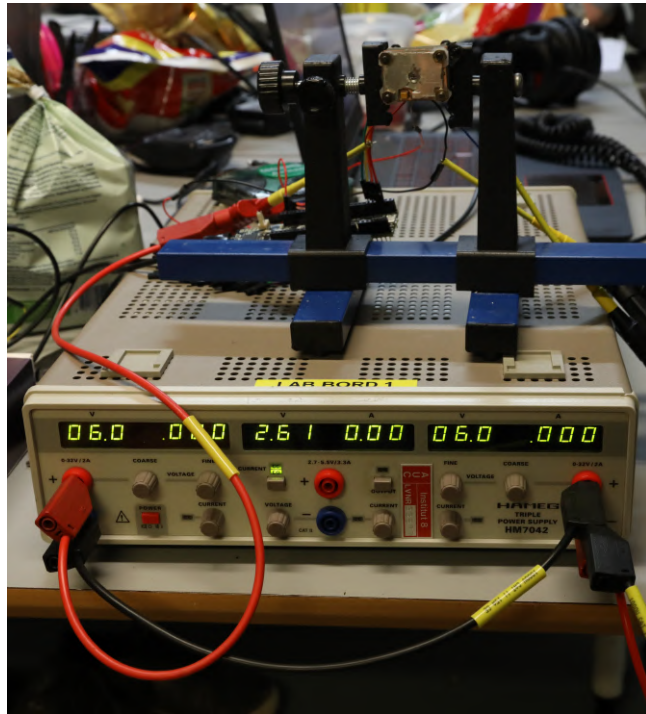


**Figure F.1:** Picture of the setup of the band pass filter.

To make the spectral analysis test an Analog Discovery is connected to the BPF. To power the BPF a power supply of  $\pm 6$  V is connected. The spectrum analysis is done with a frequency sweep ranging between 2.5 kHz and 50.5 kHz.

**Table F.1:** Table of equipment used in the test

List of Equipment		
Name / Description	Type	AAU-ID
Band Pass Filter	-	-
Hameg Power Supply	HM7042-2	33877
Analog Discovery 2	-	-

F.3. Test results and data processing

### F.3 Test results and data processing

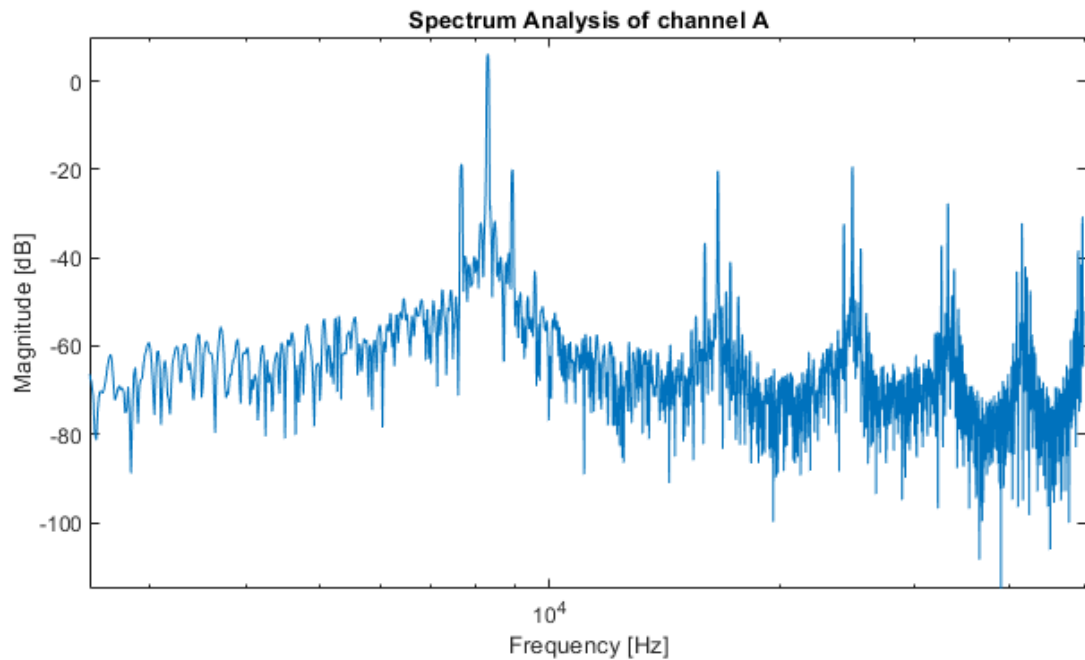


**Figure F.2:** Graph showing a sequence analysis of channel A.

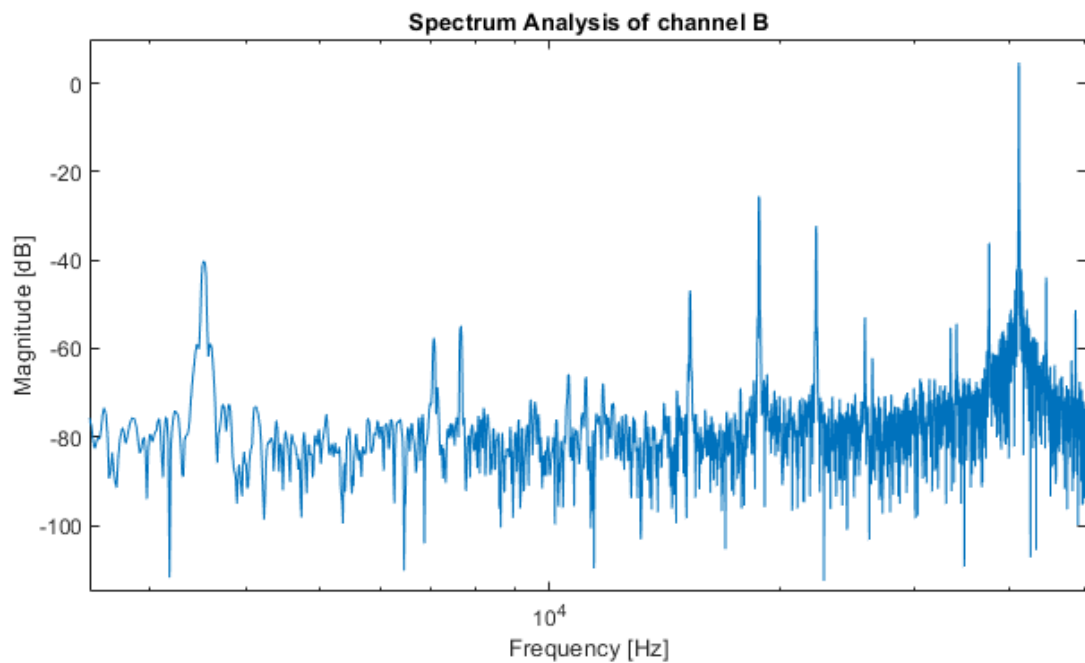


**Figure F.3:** Graph showing a sequence analysis of channel B.

### F.3. Test results and data processing

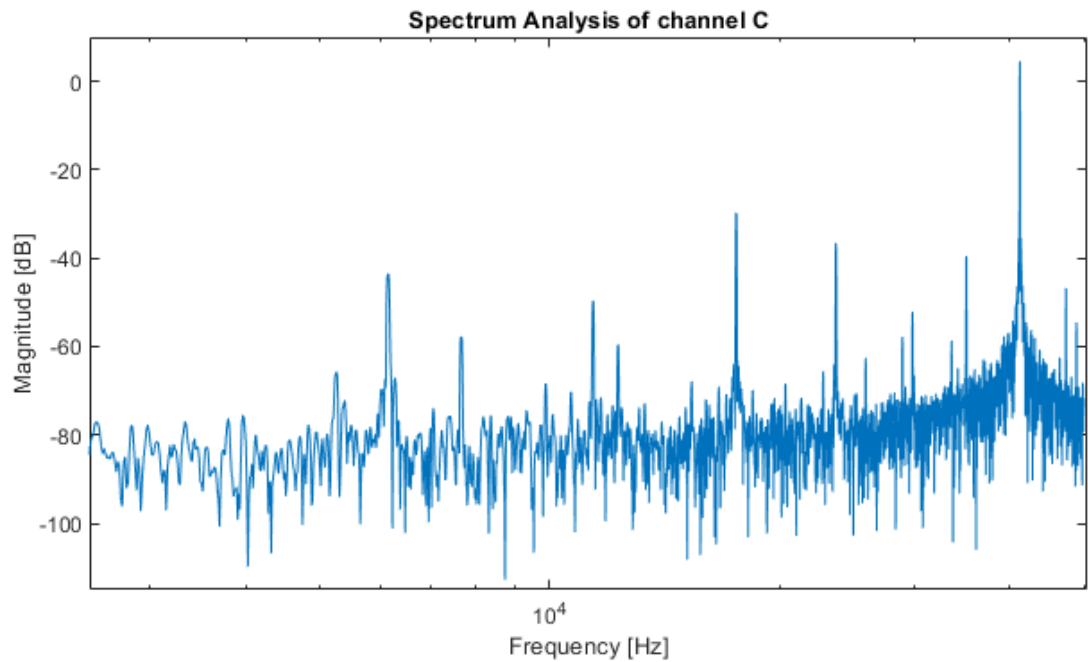


**Figure F.4:** Graph showing a sequence analysis of channel C.

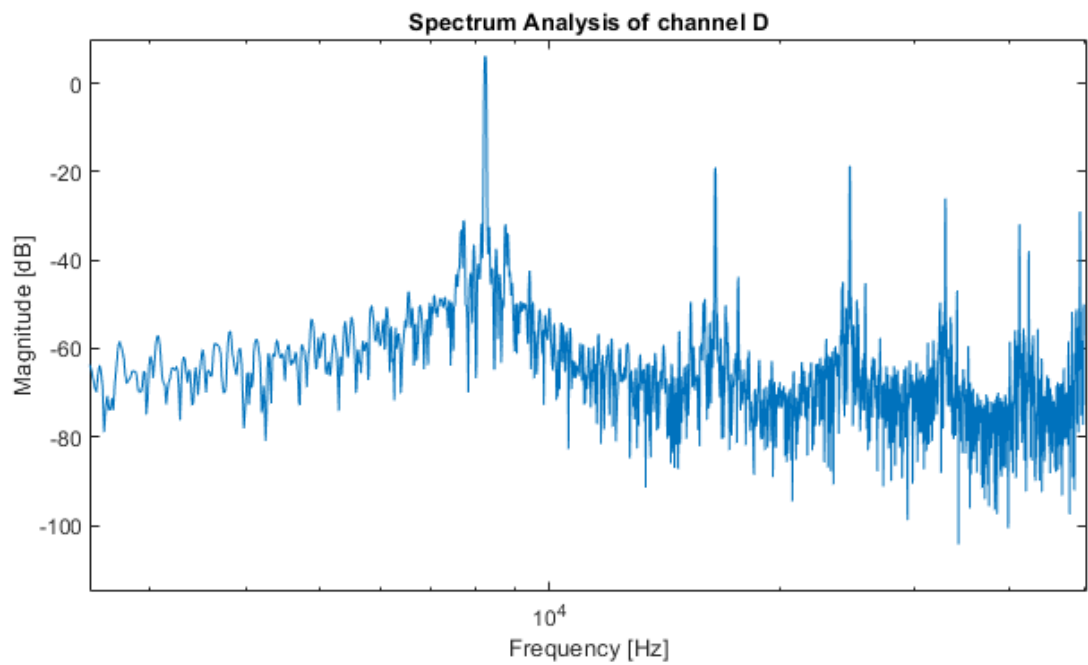


**Figure F.5:** Graph showing a sequence analysis of channel D.

## Appendix G

# Test journal: Photodiode Circuit

In this appendix is the test journal of the tests of photodiode circuit.

### G.1 Test purpose

The purpose of the test is to measure the frequency response on the photodiode circuit.

### G.2 Test frame

#### Test setup, equipment and test procedure

The test was conducted in the group room, and the setup can be seen on figure G.1.

## G.2. Test frame

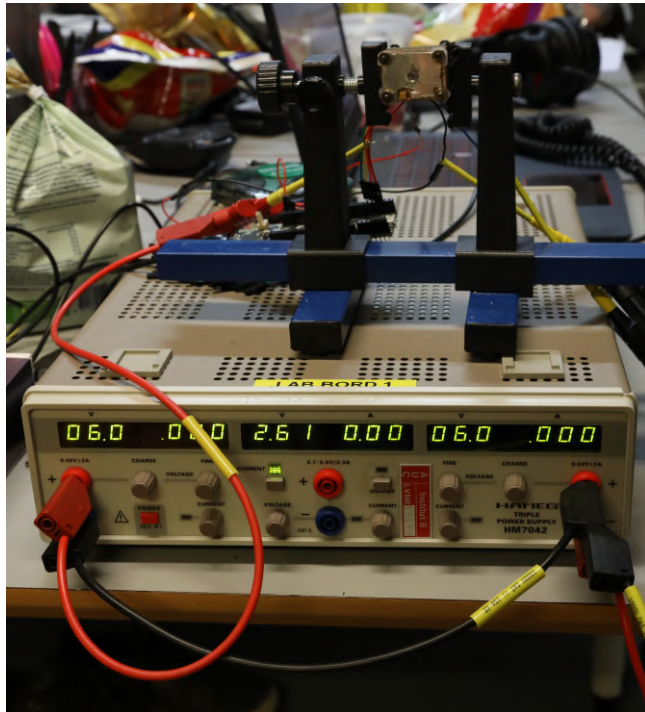


**Figure G.1:** Picture of the setup of the photodiode circuit.

To test the three stages in the photodiode circuit, an Analog Discovery is connected to the target box, the Analog Discovery inputs a frequency sweep ranging from 300 hz to 30 kHz. The target box is placed 50 cm from the quad photodiode, which gives it a "clear" input to the photodiode. Another Analog Discovery is connected to one of the four output channels of the Band pass filter. This analog discovery is also connected to a computer which logs the data. The test is repeated until all four channels have been tested.

**Table G.1:** Table of equipment used in the test

List of equipment		
Name / Description	Type	AAU-ID
Quad photodiode	OPR5925	-
High Pass Filter	-	-
Band Pass Filter	-	-
Hameg Power Supply	HM7042-2	33877
Target Box	LED LZ1-00R602	-
2 x Analog Discovery 2	-	-

### G.3 Test results and data processing

## G.3 Test results and data processing

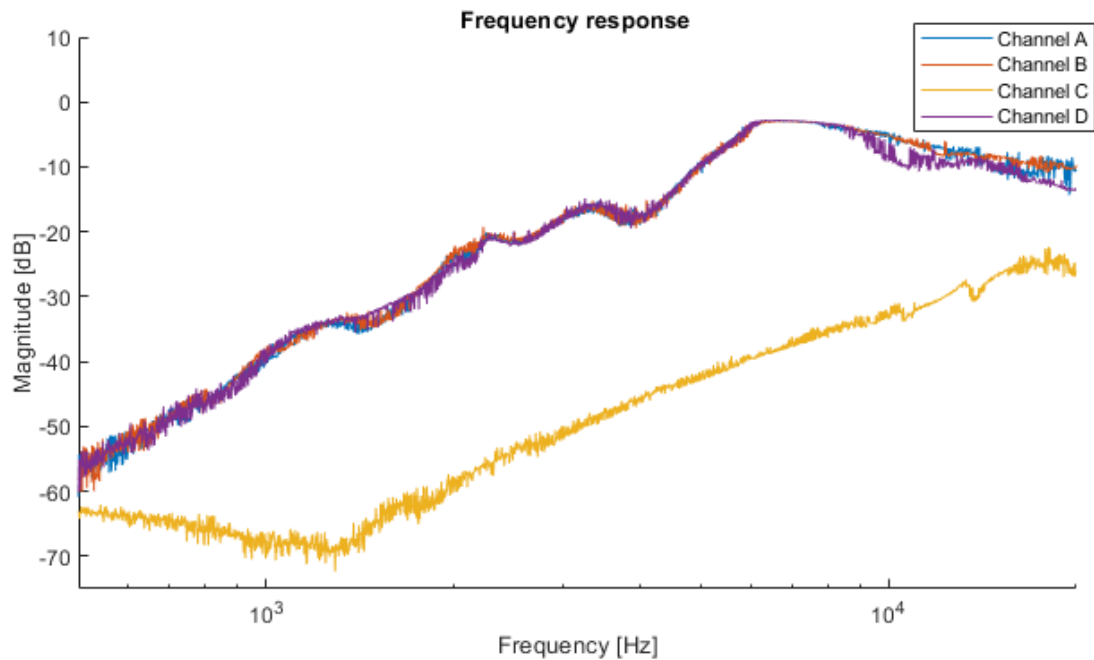


**Figure G.2:** Graph showing the frequency response of each channel.

## G.4 Sources of error and other uncertainties

Saturation occurs in the pass band of the BPF, this could have been alleviated by placing the target box further away, however time did not permit for this.

# **Test journal: Range of Position sensor**

## **G.5 Test purpose**

The purpose of this test is to test the effective range of the implemented position sensor.

## **G.6 Test frame**

### **Theoretical background**

The theory of the the position sensor was discussed in section 6.4.

### **Test setup, equipment and test procedure**

The test was conducted in a hallway and the setup was as seen on figure G.3.

## G.6. Test frame

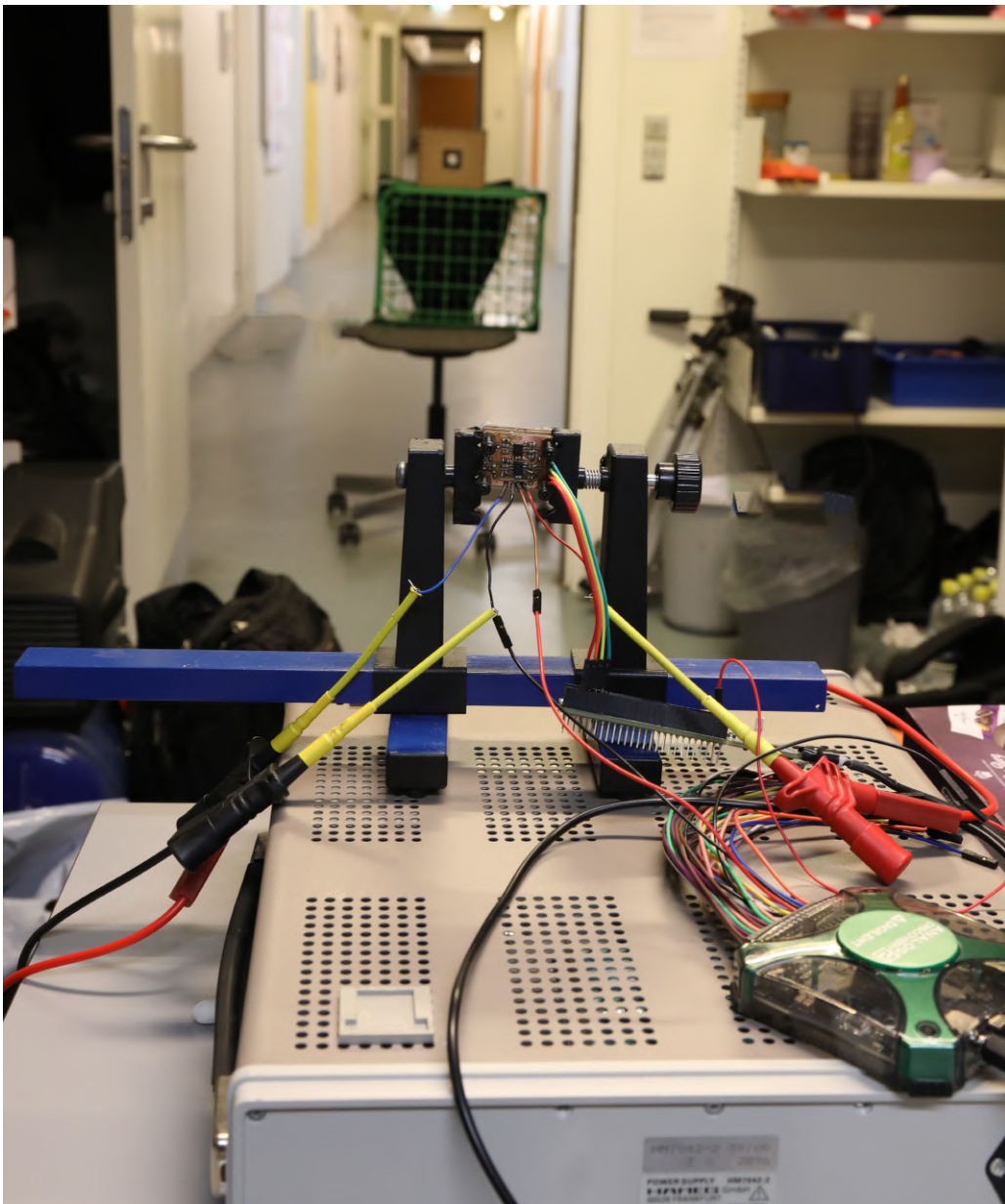


**Figure G.3:** Picture of setup of range test

The tests were performed at distances 5 m, 10 m, 20 m, 30 m, 45 m and a reference when the target was turned off. The target were pointed directly at the sensor. The target and sensor was leveled and set to the same height at all measurements. The range tests was both done with the sensor directly at diode and tilted at 45 ° on one axis.

## G.7. Test results and data processing

Title		
Name / Description	Type	AAU-ID
Analog Discovery 2	-	2179-06
Hameg Power Supply	HM7042	33905
Position sensor PCBs	-	-
Target	-	-
PSoC 5LP	programmable system on chip	-
Python data logging software	-	-

**Table G.2:** Test equipment

## G.7 Test results and data processing

The data logged is a scatter plot of the measurements of the sensor. Using the positioning system implemented in section 6.1.

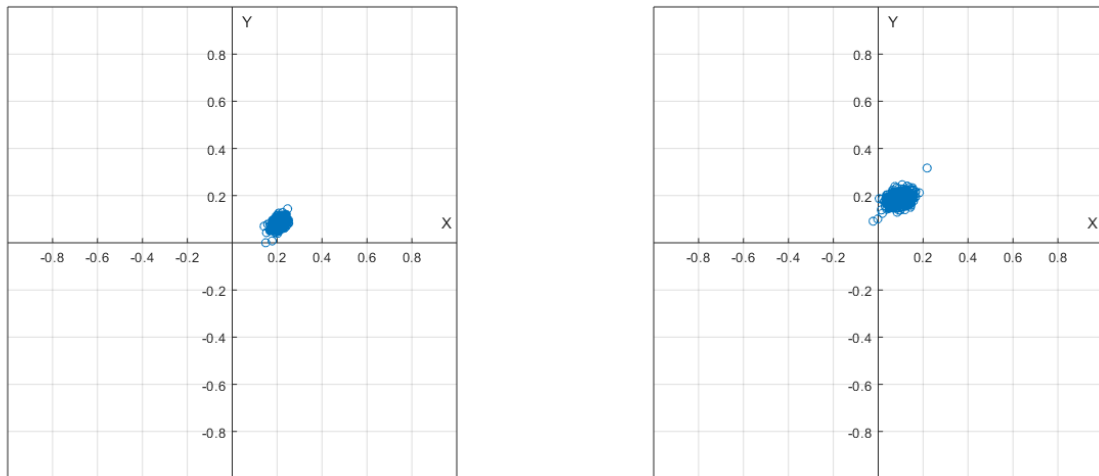
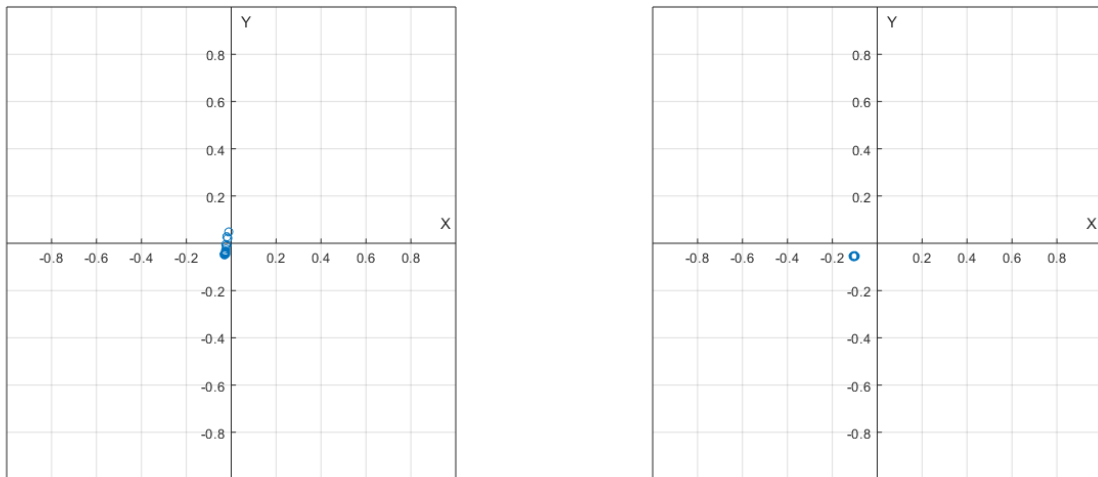


**Figure G.4:** Scatter plot of reference measurements

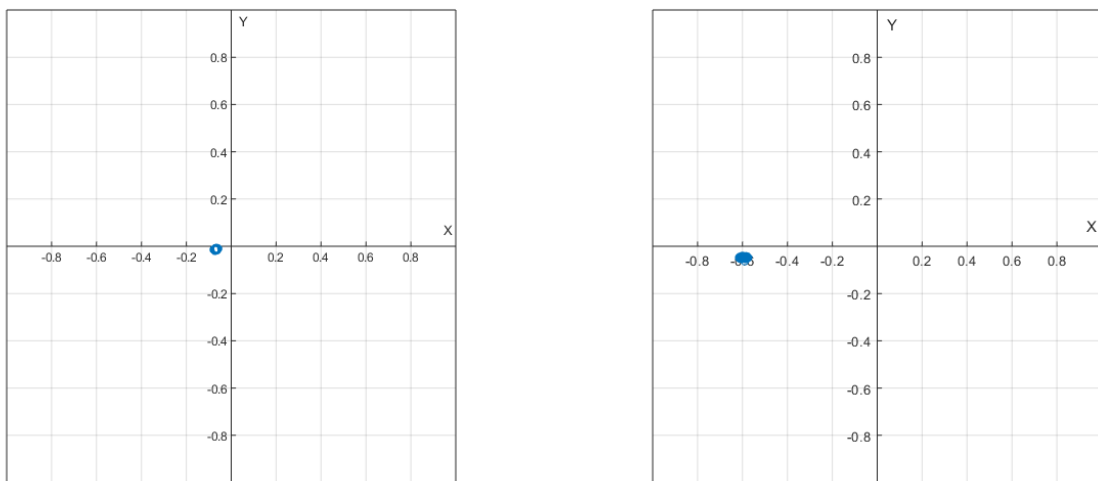
## G.7. Test results and data processing



(a) Direct measurement at 5 meters distance.

(b) 45°measurement at 5 meters distance.

**Figure G.5:** Scatter plots of measurements at 5 meters distance.

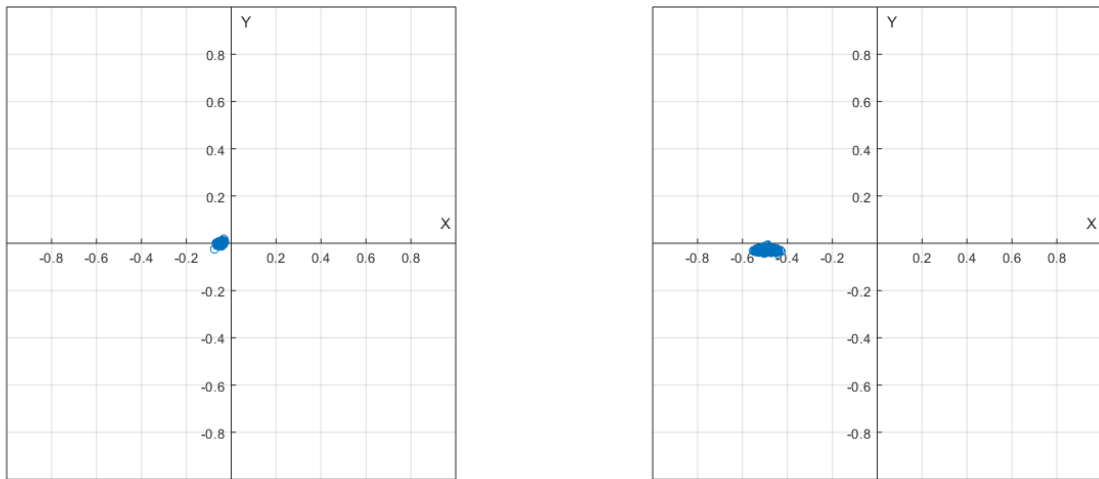


(a) Direct measurement at 10 meters distance.

(b) 45°measurement at 10 meters distance.

**Figure G.6:** Scatter plots of measurements at 10 meters distance.

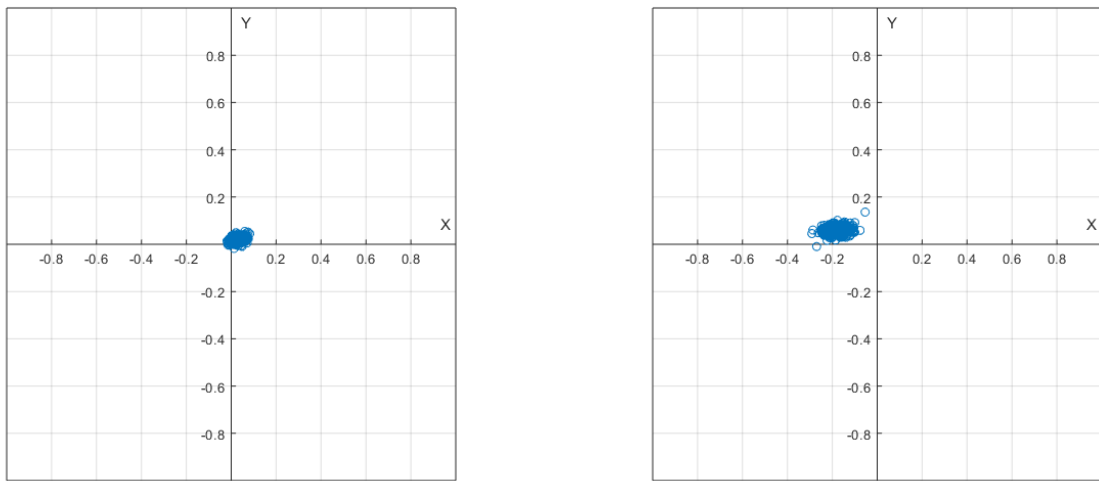
## G.7. Test results and data processing



(a) Direct measurement at 20 meters distance.

(b) 45°measurement at 20 meters distance.

**Figure G.7:** Scatter plots of measurements at 20 meters distance.

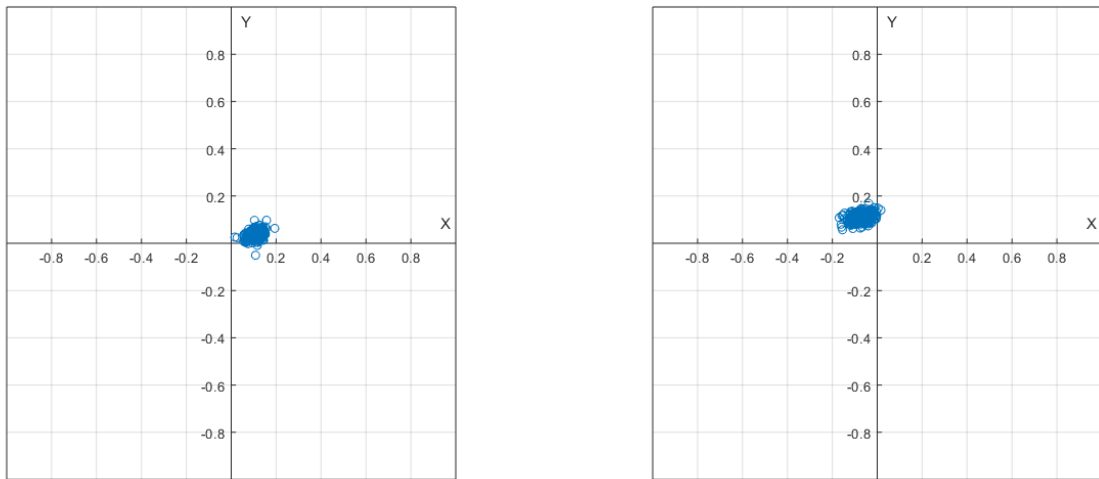


(a) Direct measurement at 30 meters distance.

(b) 45°measurement at 30 meters distance.

**Figure G.8:** Scatter plots of measurements at 30 meters distance.

## G.8. Sources of error and other uncertainties



(a) Direct measurement at 45 meters distance.

(b) 45°measurement at 45 meters distance.

**Figure G.9:** Scatter plots of measurements at 45 meters distance.

## G.8 Sources of error and other uncertainties

There are many uncertainties due to other light sources and reflection that has not been taken into consideration for the test. Additionally, there is the one diode channel which does not work at all.